

AEROTHERM CORPORATION



FINAL REPORT NO. 68-38, PART II

AN EVALUATION OF ABLATION
MECHANISMS FOR THE APOLLO
HEAT SHIELD MATERIAL

by

Eugene P. Bartlett
Larry W. Anderson

(NASA-CR-92472) FURTHER STUDIES OF
THE COUPLED CHEMICALLY REACTING
BOUNDARY LAYER AND CHARRING
ABLATOR. PART 2: AN EVALUATION OF
ABLATION MECHANISMS FOR THE APOLLO
HEAT SHIELD MATERIAL Final Report
(Aerotherm Corp.) 107 p

N94-71675

Unclass

29/34 0000303

NASH CR 92472

Aerotherm Report No. 68-38, Part II

Copy No. _____

FINAL REPORT

FURTHER STUDIES OF THE COUPLED CHEMICALLY
REACTING BOUNDARY LAYER AND CHARRING ABLATOR

PART II

AN EVALUATION OF ABLATION MECHANISMS FOR
THE APOLLO HEAT SHIELD MATERIAL

by

Eugene P. Bartlett and Larry W. Anderson

prepared for

NATIONAL AERONAUTICS AND SPACE ADMINISTRATION

October 15, 1968

CONTRACT NAS9-6719

Technical Management
NASA Manned Spacecraft Center
Houston, Texas
Structures and Mechanics Division
D. M. Curry
G. Strouhal

ABSTRACT

A number of thermochemical ablation models are postulated for the Apollo heat shield material and are compared to available ground and flight test data. The predictions are made with the Aerotherm Chemical Equilibrium (ACE) and the Charring Material Ablation (CMA) computer codes. The ACE solutions are then validated by Boundary Layer Integral Matrix Procedure (BLIMP) calculations. The ACE program generates normalized ablation rates representing the boundary layer approximately by the use of transfer coefficients. The CMA program utilizes this information as a boundary condition to generate one-dimensional transient ablation solutions. The BLIMP program solves the laminar, nonsimilar, chemically-reacting boundary layer.

Some of the more important parameters considered in the ablation analysis include various degrees of pyrolysis-gas reactivity, in-depth coking, mechanical removal of silica and/or silicon carbide, loss of pyrolysis gas through fissures which develop in the chars, and rate-controlled as well as diffusion-controlled surface chemical reactions. The model which appears to correlate the flight data best also provides the best correlation for the ground test data. This model has the following major features. First, it is assumed that the pyrolysis gases escape for the most part out of the boundary layer without contributing to a blowing reduction to the convective heat transfer. At low surface temperatures, an empirical Arrhenius-type law is employed. This is not a chemical kinetic law, but is, rather, a law for the mechanical removal of silica. At higher surface temperatures, the surface recession is limited by the availability of oxygen (diffusion-controlled carbon ablation regime). The oxygen supplied by the boundary-layer edge gas is supplemented by oxygen in the silica. Finally, at very high temperatures, carbon reactions with nitrogen and carbon sublimation become important.

FOREWORD

The present report is one of a series of four reports, published simultaneously, which describe extension and application of analyses and computational procedures for predicting the in-depth response of charring ablation materials and non-similar chemically reacting boundary layers which were generated under a previous contract (NAS9-4599). In particular, the present reports describe the extension of a laminar multicomponent chemically-reacting (equilibrium) boundary-layer program to include nongrey radiation coupling, the extension of this computational procedure to turbulent flow (at this point for incompressible flows only), the further checkout of a code which couples the laminar boundary layer procedure to a transient charring ablation code, and the application of these and other computational procedures to the Apollo heat shield material and typical Apollo missions. Part I serves as a summary report and describes the present status of and solutions obtained with the various computational procedures. In Part II a thermochemical ablation program based on a transfer-coefficient approach is utilized to investigate ablation mechanisms for the Apollo heat shield material. The radiation transport model which is utilized is described in Part III, whereas the turbulent boundary layer code is discussed in Part IV.

The titles in the series are:

- Part I: Summary Report: Further Studies of the Coupled Chemically Reacting Boundary Layer and Charring Ablator, by E.P. Bartlett, W.E. Nicolet, L.W. Anderson, and R.M. Kendall.
- Part II: An Evaluation of Surface Recession Models for the Apollo Heat Shield Material, by E.P. Bartlett, and L. W. Anderson.
- Part III: A Nongrey Radiation Transport Model Suitable for Use in Ablation-Product Contaminated Boundary Layers, by W. E. Nicolet
- Part IV: Nonsimilar Solution of an Incompressible Turbulent Boundary Layer by an Integral Matrix Method, by L. W. Anderson and R. M. Kendall.

This effort was conducted for the Structures and Mechanics Division of the Manned Spacecraft Center, National Aeronautics and Space Administration under Contract NAS9-6719 with Mr. Donald M. Curry as the NASA Technical Monitor. Development of the turbulent boundary layer code was sponsored jointly by NASA/MSC and by the Air Force Weapons Laboratory, Kirtland Air Force Base, with Lt. Ronald H. Aungier as Project Engineer. Extension of the turbulent boundary layer analysis to compressible flows is continuing under AFWL sponsorship. Mr. Eugene P. Bartlett of Aerotherm Corporation was Program Manager and Principal Investigator for the efforts reported here.

TABLE OF CONTENTS

<u>Section</u>	<u>Title</u>	<u>Page</u>
	ABSTRACT	ii
	FOREWORD	iii
	LIST OF TABLES	v
	LIST OF FIGURES	v
	LIST OF SYMBOLS	ix
1	INTRODUCTION	1
2	CORRELATION OF SURFACE THERMOCHEMISTRY SOLUTIONS WITH AND WITHOUT LOW SILICA FAIL TEMPERATURE	3
	2.1 Surface Thermochemistry Models with Dominant B ₁ Effects	3
	2.2 Surface Thermochemistry Models Without Dominant B ₁ Effects	10
	2.2.1 Reactive Pyrolysis Gases Considering Coking	11
	2.2.2 Frozen Pyrolysis Gases	13
	2.2.3 Fissure Model	18
	2.3 Discussion of Results	19
3	DEVELOPMENT OF RATE LAW FOR REMOVAL OF SILICA AT LOW SURFACE TEMPERATURES	22
	3.1 Introductory Remarks	22
	3.2 Development of Rate Law for Ground Test Data	24
	3.3 Application of Rate Law to Flight Test Conditions	28
4	CORRELATION OF SURFACE THERMOCHEMISTRY MODELS WITH FLIGHT DATA	30
	4.1 Introductory Remarks	30
	4.2 Preliminary Flight Calculations	30
	4.3 Flight Predictions Using Official Trajectory and Current Material Properties Model	32
	4.4 Interim Summary	40
5	BOUNDARY LAYER (BLIMP) SOLUTIONS FOR THE APOLLO HEAT SHIELD MATERIAL	41
	5.1 Demonstration of Correspondence Between BLIMP and ACE Programs	41
	5.2 Flight Predictions Performed with the BLIMP Program	44
6	CONCLUSIONS AND RECOMMENDATIONS	50
	REFERENCES	52
	APPENDIX A - APOLLO HEAT SHIELD MATERIAL PROPERTIES USED IN THE PRESENT STUDY	
	APPENDIX B - SUMMARY OF RECOMMENDED SURFACE THERMOCHEMICAL ABLATION MODEL	
	APPENDIX C - SUMMARY OF GROUND TEST DATA UTILIZED IN THIS STUDY	
	APPENDIX D - AN EVALUATION OF THE EFFECTS OF POROUS FLOW THROUGH THE SCHAEFER TEST MODELS	
	APPENDIX E - AN ATTEMPT TO PREDICT SURFACE RECESSION FOR THE APOLLO HEAT SHIELD MATERIAL ON THE BASIS OF SILICA-CARBON REACTION KINETICS ALONE	

LIST OF TABLES

<u>Number</u>	<u>Title</u>	<u>Page</u>
I	Char and Pyrolysis Gas Elemental Mass Fractions Considering Minor Constituents in Char	4
II	Char and Pyrolysis Gas Elemental Mass Fractions Neglecting Minor Constituents in Char	4
III	Char and Pyrolysis Gas Elemental Mass Fractions Considering Coking	11
IV	Surface Thermochemistry Solutions With and Without SiC* Fail Temperature of 500°K (Frozen Pyrolysis Gases, SiO ₂ * Fail Temperature of 500°K, B' _g = 0.6, P = 0.028 Atmospheres)	16
V	Comparison of BLIMP and CMA/ACE Solutions for a Typical Superorbital Trajectory at Peak Heating	49

LIST OF FIGURES

<u>Number</u>	<u>Title</u>	<u>Page</u>
1	Surface Thermochemistry Model for Reactive Pyrolysis Gases (P = 0.028 atm)	5
2	Surface Thermochemistry Model for Reactive Pyrolysis Gases with Low Silica Fail Temperature (P = 0.028 atm)	6
3	Correlation of Reactive Pyrolysis Gas Surface Thermo- chemistry Model with Ground Test Data a. Model 91/BH/2.0 (H _T = 10,970 Btu/lb, P _{T2} = 0.0079 atm, θ = 60 sec)	9
	b. Model 27/BH/2.0 (H _T = 10,270 Btu/lb, P _{T2} = 0.0292 atm, θ = 90 sec)	9
4	Surface Thermochemistry Model for Reactive Pyrolysis Gases Considering Coking (P = 0.028 atm)	11
5	Correlation of Coking Surface Thermochemistry Model with Ground Test Data	13
6	Surface Thermochemistry Model for Frozen Pyrolysis Gases (P = 0.028 atm)	14
7	Correlation of Frozen Pyrolysis Gas Surface Thermochemistry Model with Ground Test Data	14
8	Correlation of Fissure Surface Thermochemistry Model with Ground Test Data	19
9	Correlation of Schaefer Ground Test Data in Terms of B' _c √P	25
10	Comparison with Ground Test Data of Fissure Surface Thermo- chemistry Model Including B' _c √P Correlation for Mechanical Removal of Silica	25

LIST OF FIGURES (continued)

<u>Number</u>	<u>Title</u>	<u>Page</u>
11	Comparison of Fissure Model Predictions for Surface Temperature with Measured Data for Two Schaefer Ground Tests	
	a. Model 114/BH/4.0 ($H_T = 4,910$ Btu/lb, $P_{T_2} = 0.0112$ atm, $\theta = 210$ sec)	26
	b. Model 124/BH/4.0 ($H_T = 19,040$ Btu/lb, $P_{T_2} = 0.0279$ atm, $\theta = 20$ sec)	26
12	Fissure Model Predictions for Surface Recession Rate for Two Schaefer Ground Tests	
	a. Model 114/BH/4.0 ($H_T = 4,910$ Btu/lb, $P_{T_2} = 0.0112$ atm, $\theta = 210$ sec)	27
	b. Model 124/BH/4.0 ($H_T = 19,040$ Btu/lb, $P_{T_2} = 0.0279$ atm, $\theta = 20$ sec)	27
13	Correlation of Schaefer Ground Test Data in Terms of \dot{S}	28
14	Surface Thermochemistry Map for Apollo Vehicle Based on \dot{S} Correlation of Ground Test Data	28
15	Predictions for Typical Superorbital Trajectory for Various Nonfissure Models and Low SiO_2^* Fail Temperature (900°K)	
	a. Surface Temperature	31
	b. Surface Recession Rate	31
16	Surface Recession Rate Histories for Typical Superorbital Trajectory with Low SiO_2^* Fail Temperature (900°K) for Fissure and Nonfissure Models	33
17	Temperature Histories for Typical Superorbital Trajectory with Low Fail Temperature (900°K) for Fissure and Nonfissure Models	
	a. Surface Temperature	33
	b. 0.1 Inch from Initial Surface	34
	c. 0.3 Inch from Initial Surface	34
	d. 0.6 Inch from Initial Surface	34
	e. 0.9 Inch from Initial Surface	34
18	Temperature Histories for Typical Superorbital Trajectory with Fissure Model and Silica Mechanical Removal Rate Laws	
	a. Surface Temperature	35
	b. 0.1 Inch from Initial Surface	35
	c. 0.3 Inch from Initial Surface	35

LIST OF FIGURES (continued)

<u>Number</u>	<u>Title</u>	<u>Page</u>
	d. 0.6 Inch from Initial Surface	35
	e. 0.9 Inch from Initial Surface	36
19	Surface Recession Rate Histories for Typical Superorbital Trajectory with Fissure Model and Silica Mechanical Removal Rate Laws	36
20	Temperature Histories for Typical Superorbital Trajectory with Fissure and Post-Peak Fissure Models	
	a. Surface Temperature	39
	b. 0.1 Inch from Initial Surface	39
	c. 0.3 Inch from Initial Surface	39
	d. 0.6 Inch from Initial Surface	39
	e. 0.9 Inch from Initial Surface	40
21	Surface Recession Rate Histories for Typical Superorbital Trajectory with Fissure and Post-Peak Fissure Models	40
22	Comparison of Surface Thermochemistry Maps for Fissure and Nonfissure Models without Low Silica Fail Temperature as Generated by BLIMP and ACE Programs	42
23	Velocity Profiles in Boundary Layer over Ablating Apollo Heat Shield ($H_T = 25,000$ Btu/lb, $P_{T_2} = 0.028$ atm, Non-fissure Model)	43
24	Temperature Profiles in Boundary Layer over Ablating Apollo Heat Shield ($H_T = 25,000$ Btu/lb, $P_{T_2} = 0.028$ atm, Nonfissure Model)	43
25	Elemental Mass Fraction Profiles in Boundary Layer over Ablating Apollo Heat Shield ($H_T = 25,000$ Btu/lb, $P_{T_2} = 0.028$ atm, Nonfissure Model)	43
26	Pressure Ratio and Pressure Gradient Parameter Along Apollo Windward Ray for Typical Superorbital Trajectory	44
27	Comparison of Nonablating Heat-Transfer Coefficients along Apollo Windward Ray as Supplied by NASA-MSC and Computed by BLIMP for Typical Superorbital Trajectory	45
28	Distributions of Nonablating Mass-Transfer Coefficients along Apollo Windward Ray for Typical Superorbital Trajectory	45
29	Boundary Layer Solutions along Apollo Windward Ray for Fissure and Nonfissure Models Considering Steady-State Surface Energy Balances for Typical Superorbital Trajectory (Time = 30,030 sec)	
	a. Mass-Transfer Coefficient	46

LIST OF FIGURES (concluded)

<u>Number</u>	<u>Title</u>	<u>Page</u>
	b. Surface Recession Rate	46
	c. Surface Temperature	46
30	Boundary Layer Solutions along Apollo Windward Ray for Fissure and Nonfissure Models for Injection Rates Predicted by CMA/ACE for Typical Superorbital Trajectory (Time = 30,030 sec)	
	a. Surface Recession Rate	47
	b. Mass-Transfer Coefficient	47
	c. Surface Temperature	48
31	Variation of C_M/C_{M0} for Fissure and Nonfissure Models ($H_T = 25,000$ Btu/lb, $P_{T2} = 0.028$ atm)	48

LIST OF SYMBOLS

A	area
B	pre-exponential factor
B'	blowing parameter
C _p	specific heat
E _a	activation energy
h	enthalpy
H _T	total enthalpy
k	conductivity
K	permeability
L	thickness
m	mass
\dot{m}	mass flux per unit area
\dot{m}_C^*	kinetically controlled consumption rate of carbon per unit area
P	pressure
P _{T2}	total pressure behind normal shock
q	heat flux per unit area
R	universal gas constant
R _{eff}	effective nose radius
\dot{S}	surface recession rate
T	temperature
U	velocity
V	gas velocity
x _i	mole fraction of species i
α	viscous resistance coefficient
β	pressure gradient parameter; also inertial resistance coefficient
δ	particle diameter
ϵ	emissivity; also porosity
θ	time
μ	viscosity

LIST OF SYMBOLS (concluded)

ρ	density
$\rho_e^{u C_H}$	heat-transfer coefficient
$\rho_e^{u C_M}$	mass-transfer coefficient

SUBSCRIPTS

c	char
g	pyrolysis gas
o	nonablating or initial
s	solid
ss	steady-state
t	total gas (char + pyrolysis gas)
w	wall
∞	upstream of the shock

SUPERSCRIPTS

*	condensed species
---	-------------------

AN EVALUATION OF ABLATION MECHANISMS FOR THE APOLLO HEAT SHIELD MATERIAL

SECTION 1

INTRODUCTION

The primary intent of this report is to develop an understanding of mechanisms which control ablation of the Apollo heat shield material utilizing a generalized surface thermochemistry computer program. Physicochemical models are postulated, theoretical predictions are made, and these predictions are compared to ground and flight test data.

The material under consideration is a low-density ablation material, AVCOAT 5026-39/HC-GP, bonded to a primary structure. The ablation material is basically an epoxy-novalac resin with phenolic microballoons and silica-fiber reinforcement in a fiberglass-reinforced-phenolic honeycomb matrix. Although this composite maintains its cellular appearance after fabrication, the virgin material is treated theoretically as a continuum. Upon being subjected to sufficiently high heating rates, the ablation material decomposes chemically, forming a pyrolysis gas and a char residue. The material properties utilized in the present study are taken directly from post-test chars and are presented in Appendix A. In-depth thermal analyses are compared therein to ground and flight test data in order to validate the in-depth thermal properties model. The recommended surface thermochemical ablation model resulting from this study is summarized in Appendix B.

The computer codes utilized in the present study are the Aerotherm Chemical Equilibrium (ACE) program, the Charring Material Ablation (CMA) program, and the Boundary Layer Integral Matrix Procedure (BLIMP). The ACE program solves for surface chemistry and satisfies surface elemental mass balances, producing solutions for normalized ablation rates (B'_c) for ranges of pressure (P), surface temperature (T_w), and normalized pyrolysis gas rate (B'_g). A variety of physicochemical models can be assumed including consideration of equilibrium or rate-controlled reactions at the surface and mechanical removal of candidate surface species. These results are of interest in themselves, but also serve as input to the CMA program. The CMA program is an implicit finite-difference computational procedure which solves for the surface energy balance while computing the one-dimensional transient transport of energy in a three-dimensional isotropic material which can ablate from the front surface and decompose in depth. The BLIMP program computes the non-similar, laminar, chemically-reacting boundary layer. The characteristics

of these programs are summarized in Part I of this series of reports. A more complete description of these programs and their capabilities and restrictions are contained in References 1 through 3, respectively.

The ground test data utilized in the present study is that of Schaefer et al (Ref. 4). These data, obtained in an arc tunnel facility, cover a range of enthalpies from 3,000 to 30,000 Btu/lb and local stagnation pressures of 0.008 to 1.0 atmospheres. A summary of these test results is presented in Appendix C.

The approach which is taken in this report is to consider, first, "limiting" theories where the silica in the char is either permitted to be the surface species or required to fail mechanically if it wants to form the surface species. A number of such ACE solutions are presented in Section 2 and compared therein to the ground test data of Schaefer. These correlations show that some mechanical removal of silica does take place. An empirically-derived rate law for mechanical removal of silica is then proposed in Section 3. Correlations with flight test data are reported in Section 4. Nonsimilar laminar boundary layer solutions, obtained as a check on the transfer-coefficient calculations, are described in Section 5. Conclusions and recommendations are presented in Section 6.

SECTION 2

CORRELATION OF SURFACE THERMOCHEMISTRY SOLUTIONS WITH AND WITHOUT LOW SILICA FAIL TEMPERATURE

A number of decisions have to be made regarding mechanical removal and nonequilibrium considerations in order to generate a set of ACE solutions. This is especially true for a material as complex as the Apollo heat shield. The resulting ACE maps of B'_c versus surface temperature with B'_g and pressure as parameters can be strongly dependent upon the choices which are made. In this section, ACE maps are presented and correlated with the data of Schaefer for a number of assumed models which are limiting in the sense that silica is either required to fail mechanically or permitted to serve as the material surface. A model which appears to correlate these data well is then considered further in Section 3 where a rate law for the mechanical removal of silica is developed.

As will be shown, strikingly different ACE maps are obtained depending upon whether (1) the pyrolysis gases, based on the elemental composition resulting from primary pyrolysis, are allowed to react at the surface with the char and boundary-layer edge gases or (2) the pyrolysis gases are either allowed to equilibrate with the subsurface char or are not allowed to react with the char and boundary-layer edge gases. The B'_g is a dominant parameter in the former, but takes on only a secondary role in the latter. Several models within these two categories are considered in the following subsections.

2.1 SURFACE THERMOCHEMISTRY MODELS WITH DOMINANT B'_g EFFECTS

The most straightforward application of the ACE program is to consider the pyrolysis gas and char resulting from the primary pyrolysis to equilibrate at the surface with each other and with the boundary-layer-edge gases, and to consider all possible candidate surface materials while imposing no fail temperatures. Based upon chemical analysis and TGA data, the pyrolysis gas and char were assigned densities of 18 and 16 lb/ft³, the char being composed of C*, SiO₂*, Al₂O₃*, CaO*, and B₂O₃*. (An asterisk (*) is used to indicate condensed species.) The elemental compositions of the char and pyrolysis gas are presented in Table 1.

ACE calculations performed using this model indicated that the minor constituent aluminum plays an important role in the ablation process. No surface recession was predicted to occur until very high surface temperatures, a

TABLE I

CHAR AND PYROLYSIS GAS ELEMENTAL MASS FRACTIONS
CONSIDERING MINOR CONSTITUENTS IN CHAR

<u>Element</u>	<u>Pyrolysis Gas</u>	<u>Char</u>
H	0.0930	--
B	--	0.0079
C	0.5470	0.4880
N	0.0190	--
O	0.3410	0.2605
Al	--	0.0212
Si	--	0.1852
Ca	--	0.0366

surface of $Al_2O_3^*$ being predicted. These results suggest that there is no chemical means for removing aluminum from the char until the surface becomes hot enough for $Al_2O_3^*$ to decompose into gaseous products. At higher B'_C , BN^* , SiC^* and finally C^* were predicted to be the surface species. Another significant feature of these results was that B'_g is a very important parameter, B'_C being reduced as B'_g is increased.

It seems unlikely that minor constituents such as Al and B should control the surface recession. Rather, one might suspect that they would be carried off in condensed form if there were no means for gasification. Therefore, $Al_2O_3^*$, $B_2O_3^*$ and CaO^* were removed from consideration. The approach taken was to replace these species by an equal mass of SiO_2^* to yield the char and pyrolysis gas compositions of Table II while retaining the same char and pyrolysis gas densities.

TABLE II

CHAR AND PYROLYSIS GAS ELEMENTAL MASS FRACTIONS
NEGLECTING MINOR CONSTITUENTS IN CHAR

<u>Element</u>	<u>Pyrolysis Gas</u>	<u>Char</u>
H	0.0930	--
C	0.5470	0.488
N	0.0190	--
O	0.3410	0.273
Si	--	0.239

The results of ACE calculations for this model are presented in Figure 1 for a pressure of 0.028 atm and several B'_g . Results are also shown for the steady-state ratio of B'_g/B'_c which is numerically equal to ρ_g/ρ_c , or 1.125. The constant B'_g curves are of interest in transient problems. As steady-state ablation is approached such that the pyrolysis zone moves at the same speed as the receding surface, the steady-state ratio of B'_g/B'_c is attained.

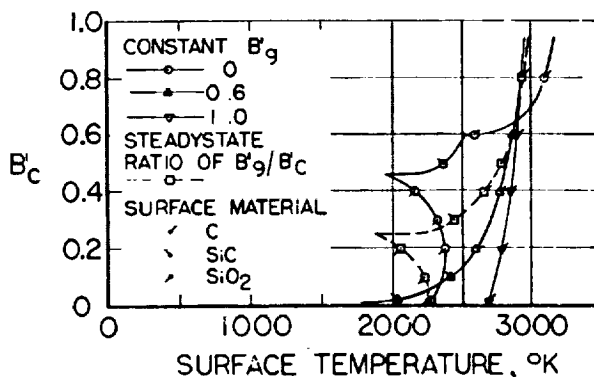


Figure 1. Surface Thermochemistry Model for Reactive Pyrolysis Gases ($P = 0.028$ atm)

With the minor char constituents removed from consideration, SiO_2^* is predicted to be the surface species under the conditions of low B'_g and B'_c . As B'_c is increased the surface changes to SiC^* and then C^* . At higher B'_g , the SiO_2^* and SiC^* zones disappear and the surface is C^* over the entire range of B'_c . Whether or not SiO_2^* and SiC^* play such significant roles remains to be seen, but at least silicon is a major component of the char.

The behavior of SiO_2^* parallels the role played by Al_2O_3^* in the calculations mentioned previously. That is, there is no chemical means for removing SiO_2^* from the surface until the surface temperature is sufficiently high that decomposition into SiO and/or Si gas takes place. Reaction with C^* is permitted resulting, for example, in SiO and CO , but SiO then subsequently reacts with oxygen from the boundary-layer edge to reform SiO_2^* so there is no net chemical removal of silica from the surface by this process.*

* In a nitrogen environment, this reaction could result in the removal of silica and some carbon; however, there is then no means for chemical removal of the excess carbon so again thermochemical ablation theory predicts no surface recession until sufficiently high surface temperatures that cyanogen forms and carbon sublimates. More will be said of this later.

There are a number of reasons that one might expect at least some mechanical removal of silica at surface temperatures below the 2,200°K shown above for the onset of thermochemical ablation. First, the silica "melts" at lower temperatures and there will be some removal by liquid-layer flow. The loss of material by this manner was observed in movies of some of the Schaefer tests (principally in the vicinity of 1,800-2,000°K) and liquid globules were found on the surfaces after cooldown. In addition, there is considerable experimental data which confirm that SiO_2^* and C^* react at surface temperatures in this same temperature range, and one might expect that the SiO_2^* which reforms at the surface would be mechanically weak.

In order to obtain an understanding of the effect of silica mechanical removal on surface recession rate, calculations were performed with a low silica fail temperature.* An unrealistically low fail temperature of 1,200°K was chosen in order to demonstrate the effect of mechanical removal, if it were to occur, over a wide surface temperature range. Solutions for a pressure of 0.028 atm and several B'_g are presented in Figure 2.

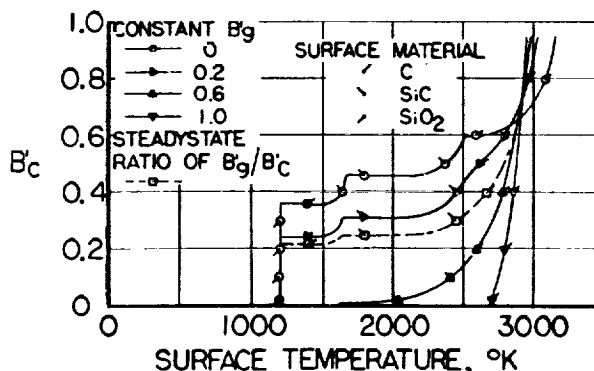


Figure 2. Surface Thermochemistry Model for Reactive Pyrolysis Gases with Low Silica Fail Temperature ($P = 0.028$ atm)

With silica permitted to fail, the B'_c curves for the lower B'_g are extended down to the fail temperature. The steady-state B'_c rises at the fail temperature to a value of about 0.22 and then continues to rise slowly with increase in surface temperature until a T_w of the order of 2,400°K at which point it begins to rise very rapidly. The B'_c is higher for values of B'_g

* See Reference 1 for a discussion of the fail temperature concept.

below the steady-state values and lower for higher B'_g . For example, the B'_c is zero (i.e., no surface recession) for T_w below 2,680°K for B'_g of 1.0. The B'_g is considerably greater than 1.0 during a substantial portion of a typical Apollo superorbital reentry trajectory, approaching values as high as 10 to 20 during the major heating pulse. Thus, it can be seen that the B'_g is a very important parameter in the present model.

The results of Figure 2 are readily explainable from the basic physics. Consider first the $B'_g = 0$ curve where the problem is reduced to one of a homogeneous mixture of SiO_2^* and C^* . At the lowest surface temperatures, all of the silicon in the char is removed mechanically, as the surface recedes, in the form of condensed-phase SiO_2^* . Hence, the problem reduces further to that of carbon ablation. At temperatures slightly above the fail temperature of 1,200°K, the B'_c has a constant value of 0.362. This is the well-known diffusion limit for combustion of carbon to form CO



The value of B'_c for pure carbon of 0.176 is increased to the current value because the char is only 48.8 percent by weight carbon. Thus, with the use of a low silica fail temperature, the silica fails at just that rate such that the carbon is exposed and can react with the oxygen which diffuses across the boundary layer. The mechanical removal rate of silica is constant on this plateau.

When the surface temperature exceeds 1,400°K, SiO_2^* becomes the surface species and vaporization of silica



begins to take on importance. Thus, the amount of silica which leaves in the condensed phase begins to decrease, and the oxygen released by Reaction (2) becomes, in effect, available for reaction with carbon. Another way of looking at this is to consider the equivalent reaction



which is obtained by adding Reactions (1) and (2). In any event, the carbon consumed in this process is in addition to the carbon consumed by the oxygen

from the free stream. Thus, the B'_C increases as the surface temperature (and, hence, the vaporization rate of SiO_2^*) is increased.

At approximately 1,680°K, the decomposition rate of SiO_2^* is sufficient to remove the silicon from the char at the same rate that carbon is consumed by Reactions (1) and (3). Thus, the mass removal rate of condensed-phase SiO_2^* is reduced to zero and another plateau region is achieved, the value of B'_C being 0.458. As the surface temperature is elevated still further, the primary SiO_2^* decomposition mechanism becomes



Combining again with Reaction (1) yields



It is apparent that twice as much carbon is consumed through this decomposition reaction as through Reaction (3). Thus, another plateau would be anticipated with a B'_C of 0.62 if the concentration of SiO were to become vanishingly small compared to Si .

At temperatures above 2,500°K, sublimation of carbon, primarily in accordance with



and reaction with nitrogen to form CN



begin to take on importance and a distinct plateau is not seen for the pressure considered. At surface temperatures above 2,800°K, the B'_C begins to rise sharply as sublimation becomes increasingly more important.

The reduction of B'_C with increase in B'_g can be attributed to the way the virgin material is distributed into pyrolysis gas and char (Table II), carbon in the pyrolysis gas being in excess of that required for equilibrium. An examination of the state of the gas at the surface in the carbon-plateau region reveals that the only abundant species containing carbon is CO, whereas the ratio of carbon to oxygen in the original pyrolysis gas is considerably higher,

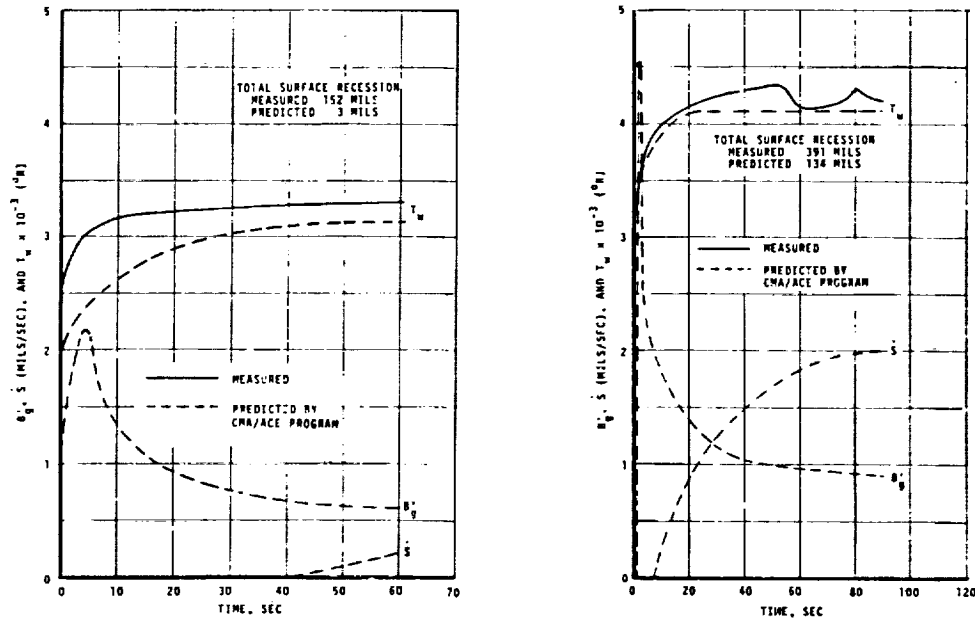
being in the form of various hydrocarbons. Thus, in order to achieve the surface gas composition, reactions of the form



are proceeding to the right. The net effect is that pyrolysis gas being supplied from the decomposition zone consumes oxygen from the boundary layer edge without contributing to surface recession.

The reactive pyrolysis gas surface recession model considering a low silica fail temperature was applied to a number of the ground tests of Schaefer, et. al. (Ref. 4). ACE maps of B'_g for various B'_g and T_w were generated for the test conditions and these were employed as input to the CMA charring ablation program (Ref. 3) to obtain predictions for transient ablation rates and temperatures.

Results are presented in Figure 3 for two typical tests, the first a 60 second test at a pressure of 0.0079 atm pressure and 10,970 Btu/lb enthalpy, and the second a 90 second test at 0.0282 atm and 10,270 Btu/lb. Shown in



(a) Model 91/BH/2.0 ($H_T = 10,970$ Btu/lb, $P_{T_2} = 0.0079$ atm, $\theta = 60$ sec) (b) Model 27/BH/2.0 ($H_T = 10,270$ Btu/lb, $P_{T_2} = 0.0282$ atm, $\theta = 90$ sec)

Figure 3. Correlation of Reactive Pyrolysis Gas Surface Thermochemistry Model with Ground Test Data

these figures are the predicted and experimental values of T_w and predicted \dot{S} and B'_g . Measured and predicted total surface recession is also indicated. The most striking result of these calculations is that the total surface recession is substantially underpredicted - 3 mils compared to 152 mils in the first case and 134 mils compared to 391 in the second. The second result of consequence is that the predicted ablation rate is strongly dependent on time. In contrast, as discussed in Appendix C, at test conditions even less severe than those reported here, series of tests at nearly identical conditions for various test durations (e.g., 60, 120, and 240 seconds) showed that the average ablation rate was fairly insensitive to time and, if anything, actually decreased slightly with increased test duration. The reason for the predicted behavior, that of low, time-dependent ablation rates can be attributed directly to the B'_g which were quite high early in the test and reduced asymptotically thereafter.

A transient ablation prediction was also made for a recent Apollo super-orbital flight using this model. Consistent with the ground-test correlations, the prediction was considerably low, 22 mils compared to a measured value of about 200 mils (Ref. 5). Clearly, this surface thermochemistry model is inadequate. In particular, the problem appears to lie in the dominant effect of B'_g on the surface recession.

2.2 SURFACE THERMOCHEMISTRY MODELS WITHOUT DOMINANT B'_g EFFECTS

There are several thermochemical ablation models which one could postulate which would tend to eliminate the strong B'_g effect. First, recalling that it is the carbon in the pyrolysis gas in excess of that required to convert the oxygen in the pyrolysis gas to CO that produces the strong B'_g effect, one might consider a different elemental composition of char and pyrolysis gas, transferring carbon from the pyrolysis gas to the char. Secondly, reactions between the pyrolysis gas, char, and boundary layer gases may not proceed to equilibrium. Thirdly, the pyrolysis gas may not mix thoroughly with the other gaseous species.

There is experimental evidence that would qualitatively support the first and third of these possibilities. First, examination of flight data for the Apollo heat shield material (Refs. 5 and 6) has shown that there is a substantial increase in carbon density near the surface, obviously due to in-depth coking reactions. Secondly, an examination of both ground data (Ref. 4) and flight test data (Ref. 5) for the Apollo heat shield material has shown numerous fissures in the char. One could speculate that a bulk

of the pyrolysis gas might pass out through these fissures and jet, for the most part, out through the boundary layer without mixing with the boundary-layer gases. These three models will be considered in the order listed. ACE maps will be generated and compared to the ground test data of Schaefer et. al. (Ref. 4).

2.2.1 Reactive Pyrolysis Gases Considering Coking

The effect of coking was treated approximately by removing all of the carbon from the pyrolysis gas in excess of that needed to convert the oxygen in the pyrolysis gas to CO and assigning this excess carbon to the char elemental composition and density. The resulting elemental compositions are shown in Table III (see Table II for elemental composition of noncoking model). The char density is increased from 16.00 to 21.24 lb/ft³, while the density of the pyrolysis gas is correspondingly decreased. Solutions for a pressure of 0.028 atm and a range of B'_g are presented in Figure 4 and can be compared to the noncoking results of Figure 2. The results for steady-state ratios of B'_g/B'_c are also indicated on these figures.

TABLE III
CHAR AND PYROLYSIS GAS ELEMENTAL MASS
FRACTIONS CONSIDERING COKING

Element	Pyrolysis Gas	Char
H	0.1311	--
C	0.3614	0.614
N	0.0268	--
O	0.4807	0.206
Si	--	0.180

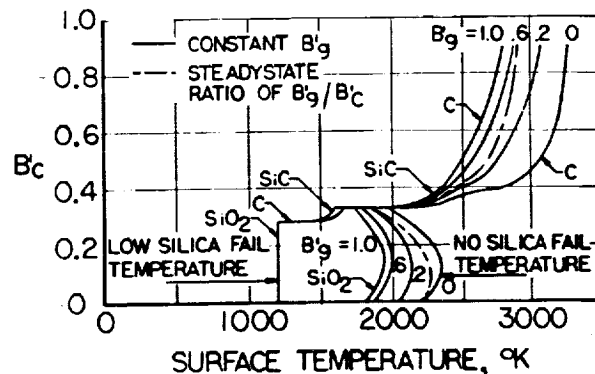


Figure 4. Surface Thermochemistry Model for Reactive Pyrolysis Gases Considering Coking ($P = 0.028$ atm)

In contrast to the noncoking model, the coking model yields plateau behavior with little effect of B'_g for T_w below 2,200°K. This result was not unanticipated as discussed previously. Briefly, in the coking model all of the carbon in the pyrolysis gas is tied up in CO so that the pyrolysis gas is neutral; whereas, in the noncoking model oxygen from the boundary layer reacts with carbon from the interior of the material when B'_g is greater than the steady-state value. In the steady-state limit, the coking and noncoking models yield identical results for surface recession of the virgin material, $B'_t = B'_g + B'_c$. This, of course, must be the case since the composition of the virgin material is the same for both models.

In order to compare this and future theoretical models to the data of Schaefer, the following approach is utilized to simplify the presentation. First, theoretical solutions are shown only for $B'_g = 0.6$. The results of a number of transient theoretical predictions for the test conditions of Schaefer for various theoretical models have indicated that the B'_g consistently rises to a maximum of about 2 to 4 but then drops rather quickly in the test to a value of 0.8 to 0.4 (see Figure 3 for example). Secondly, data are presented for two pressures, 0.008 and 0.028 atm, whereas theory is shown only for the latter pressure. The theoretical effect of a decrease in pressure from 0.028 to 0.008 atm is typically to move sublimation and vaporization curves to T_w which are 100 to 200°K lower, while values of B'_c on the various plateaus are independent of pressure.

The data of Schaefer, reduced to B'_c versus T_w by the methods described in Appendix C, are compared to the coking theoretical model in Figure 5. One can conclude from this figure that either most of the experiments were conducted in the sublimation regime and experimental and analytical uncertainties combine to yield a 500 to 800°K discrepancy, or that the data lie well above the "upper limit" prediction. There is good reason to believe that the former is not the case, in which case one must conclude that this model is unsatisfactory. In the first place, liquid globules were detected in many of these tests, attesting to the validity of the measured surface temperatures, and hardly being indicative of graphite sublimation temperatures. Secondly, the results of transient solutions indicated that there is not sufficient energy available to achieve sublimation conditions.

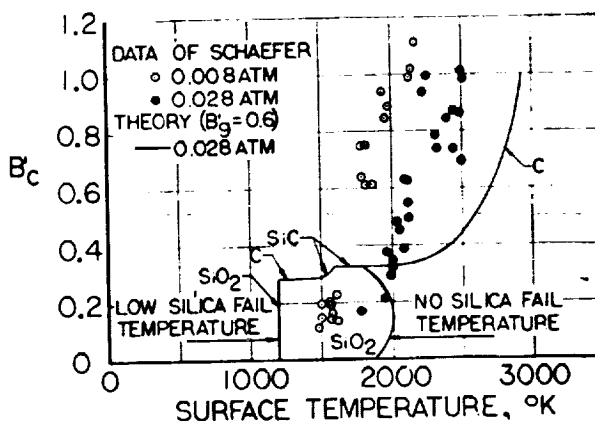


Figure 5. Correlation of Coking Surface Thermochemistry Model with Ground Test Data

2.2.2 Frozen Pyrolysis Gases

At relatively low surface temperatures one might expect that the pyrolysis gases would not equilibrate with the char and boundary-layer gases at or near the surface. The feedback to the surface of the effect of reactions further out into the boundary layer is relatively small. Hence, it is of interest to consider the case of a frozen pyrolysis gas.

Frozen pyrolysis gas ACE maps were generated based upon the following conjectured molar composition: $x(C_2H_4) = 0.30$, $x(CO) = 0.20$, $x(CH_3) = 0.15$, $x(CH_4) = 0.15$, $x(H_2O) = 0.15$, $x(N_2) = 0.04$, and $x(H_2) = 0.01$. This composition is consistent with the elemental composition of the pyrolysis gases (Table II) and is believed to represent reasonable estimates of species which might be expected for the Apollo heat shield material. A fictitious element of atomic weight 22.5 was used to represent the pyrolysis elemental composition, and a molecule consisting of one atom of this element and with the enthalpy-temperature relation of this gaseous mixture was defined.

The results are shown in Figure 6 for a pressure of 0.028 atm and B_g' of zero and 1.0. It can be seen that B_g' has no effect in the various plateau regions and has only minor effect in nonplateau regions. Furthermore, it may be noted that the plateau values of B_c are higher than in the case considered previously where the pyrolysis gas was inert because of in-depth coking. The reason for this is that carbon in the pyrolysis gas is removed from the virgin material in the present model without requiring it to react.

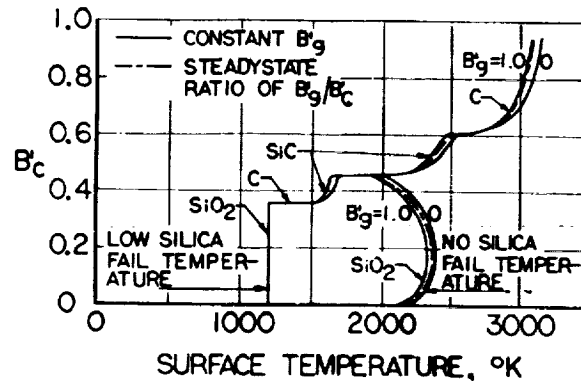


Figure 6. Surface Thermochemistry Model for Frozen Pyrolysis Gases ($P = 0.028$ atm)

The theoretical predictions are compared to the data of Schaefer in Figure 7, together with another prediction to be discussed later. The experimental B'_c data points are lower than in the coking model because, for a given \dot{S} , the \dot{m}_c is lower due to a lower ρ_c . Also, as discussed previously, the theoretical prediction for B'_c is higher. However, a substantial amount of the data are still underpredicted.

As indicated on Figure 7, SiC* is predicted to serve as the surface species for surface temperatures from 1,400 to 2,580°K. On the other hand, post-test chemical analyses of char material have indicated very little SiC* present. It is of interest, therefore, to investigate the significance of the SiC* surface.

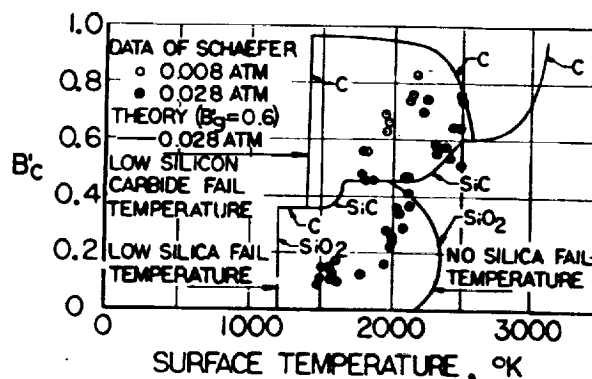
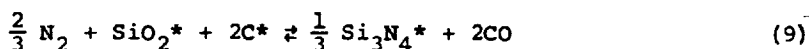


Figure 7. Correlation of Frozen Pyrolysis Gas Surface Thermochemistry Model with Ground Test Data

ACE calculations were thus performed with SiC* removed from consideration. This, in effect, is saying that the formation of SiC* is kinetically-limited. The effect on the solution is minor (as long as Si₃N₄* is also removed from consideration), the B_C' being increased for T_w of 1,800 to 2,580°K but by no more than five percent.

When Si₃N₄* is considered but required to fail, a substantial increase in B_C' is predicted for T_w of 1,480 to 1,750°K for the P and B_g' considered (B_C' rises to a peak of 0.60). This behavior is a result of an equilibrium potential to form Si₃N₄* at wall temperatures above 1,480°K in accordance with the relation



Silica in the char is removed in the form of condensed-phase SiO₂* and/or Si₃N₄* depending upon the equilibrium of this reaction. The increase in B_C' occurs as the reaction moves to the right since there is the net effect that carbon is being oxidized by the oxygen in the silica. The effect decreases for T_w above 1,530°K as a consequence of the fact that the SiO₂* begins to decompose into SiO so that eventually, at T_w above 1,750°K, Si₃N₄* is no longer being formed and only one-half of the oxygen in the silica is available to attack the carbon.

ACE maps were also generated considering a low SiC* fail temperature of 1,200°K. Solutions for B_g' of 0.6 and P = 0.028 atm are also presented in Figure 7. The low SiC* fail temperature is seen to have a dramatic effect on the theoretical predictions; namely, the B_C' is approximately doubled in the region where SiC* wants to be the surface species.

In order to gain further insight into these results, the B_C' and T_w for these solutions are tabulated in Table IV together with the predicted surface species and normalized mechanical removal rates for SiO₂* and SiC*. Starting at the 1,200°K fail temperature for SiO₂*, the surface is SiO₂* and SiO₂* is failing. As B_C' is increased, the normalized SiO₂* removal rate increases to a maximum of 0.0796 at the carbon plateau value for B_C' of 0.362. The surface then changes to carbon and the B_C' remains constant until a T_w of 1,390°K at which point equilibrium dictates that silica-carbon reactions begin to be significant in accordance with the relation



TABLE IV

SURFACE THERMOCHEMISTRY SOLUTIONS WITH AND WITHOUT SiC* FAIL
TEMPERATURE OF 500°K (FROZEN PYROLYSIS GASES, SiO₂* FAIL
TEMPERATURE OF 500°K, B_g' = 0.6, P = 0.028 ATMOSPHERES)

B' C	T _w (°K)	Surface Species	Normalized Mechanical Removal Rate For	
			- SiO ₂ *	SiC*
Low T _w (Independent of SiC* fail temperature)				
0.0100	500	SiO ₂ *	0.0022	0.
0.0500	↓	↓	0.0111	↓
0.1000			0.0224	
0.1500			0.0341	
0.2000			0.0448	
0.2500			0.0562	
0.3000			0.0675	
0.3500	↓	SiO ₂ *	0.0777	
0.3616	1200	C*	0.0796	↓
0.3620	1390	C*	0.0796 (max)	0.
Intermediate T _w				
(a) With low SiC* fail temperature				
0.3620	1390	C*	0.0796	0.
0.4000	1393	↓	0.0746	0.0134
0.5000	1399		0.0617	0.0486
0.6000	1405		0.0488	0.0840
0.7000	1410		0.0357	0.1196
0.8000	1414		0.0226	0.1553
0.9000	1418		0.0094	0.1912
0.9715 (max)	1420		0.	0.2168 (max)
0.9686	1600		↓	0.2157
0.9635	1800			0.2136
0.9555	2000			0.2103
0.9403	2200			0.2029
0.8790	2400	C*	0.	0.1672

TABLE IV (concluded)

B' C	T _w (°K)	Surface Species	Normalized Mechanical Removal Rate for	
			SiO ₂ *	SiC*
(a) With low SiC* fail temperature (concluded)				
0.8480	2440	C*	0.	0.1482
0.8038	2480	↓	↓	0.1210
0.7413	2520	↓	↓	0.0822
0.6532	2560	↓	↓	0.0273
0.609	2575	C*	0.	0.
(b) With no SiC* fail temperature				
0.3620	1390	SiC*	0.0796	0.
0.3961	1600	↓	0.0517	↓
0.4575	1760	↓	0.	↓
0.4583	2000	↓	↓	↓
0.4695	2200	↓	↓	↓
0.5350	2400	↓	↓	↓
0.609	2575	SiC*	0.	0.
High T _w (Independent of SiC* fail temperature)				
0.609	2575	C*	0.	0.
0.6122	2600	↓	↓	↓
0.6321	2800	↓	↓	↓
0.7075	3000	C*	0.	0.

As this reaction begins to move to the right, SiC^* forms and fails and less SiO_2^* is available to fail. At the peak B'_C of 0.972, the surface is still C^* , and mechanical removal is all in the form of SiC^* (meaning that Reaction (10) has gone to completion) and is at a peak value of 0.217. Here the carbon is oxidized by the boundary-layer edge gas and all of the oxygen in the silica, and, in addition, carbon is being removed mechanically via SiC^* . As wall temperature is increased, the SiC^* removal rate (and hence the B'_C) drop until $T_w = 2,575^\circ\text{K}$, $B'_C = 0.609$, and mechanical removal is zero. This decrease in B'_C is the result of SiC^* decomposition into gaseous products, less carbon being carried away in the form of SiC^* . (When SiC^* is not allowed to fail, it becomes the surface species at T_w of $1,390^\circ\text{K}$. As B'_C and T_w increase, the mechanical removal of SiO_2^* decreases until $T_w = 1,760^\circ\text{K}$, $B'_C = 0.4575$ and the mechanical removal rate is zero. SiC^* then remains as the surface species, with no mechanical removal, until $T_w = 2,575^\circ\text{K}$ and $B'_C = 0.609$.) At this point, in either event, the surface is C^* , there is no mechanical removal, and B'_C increases monotonically with T_w .

The theoretical model for frozen pyrolysis gases with low SiC^* fail temperature is seen to encompass all of the Schaefer data points for the two pressures considered in Figure 7. The significance of this result is discussed in Section 2.3.

2.2.3 Fissure Model

The idea for the "fissure" model arises from an observation of 15X photomicrographs of char samples from a recent recovered Apollo flight vehicle (Ref. 5) and from ground tests of Schaefer et. al. (Ref. 4) which revealed sizeable fissures in many, if not all, of the char segments (i.e., the charred filler material between the honeycomb walls). These fissures appear to lead from the decomposition zone to the surface. It is conjectured that the pyrolysis gases instead of passing homogeneously through the char may flow, for the most part, along the fissures and pass inefficiently through the boundary layer. With regard to thermochemical ablation theory, the results presented previously for $B'_g = 0$ are directly applicable. However, there is a major difference when it comes to applying these results to determine \dot{m}_c ; namely, in the fissure model there is assumed to be no reduction of the convective heating rate by the pyrolysis gas. Thus, $\rho_e u_e C_M$ and \dot{m}_c are higher for the same B'_C .

The data of Schaefer are compared to the fissure model in Figure 8. The disallowance of a blowing correction for B'_g substantially increases the

experimental $\rho_e u_e C_M$ and thus decreases the experimental B'_c (for the observed \dot{S}) relative to nonfissure models. As a result, all data are encompassed by the upper and lower-limit theories relative to the status of the silica in the char. Again, the significance of this result will be discussed in Section 2.3.

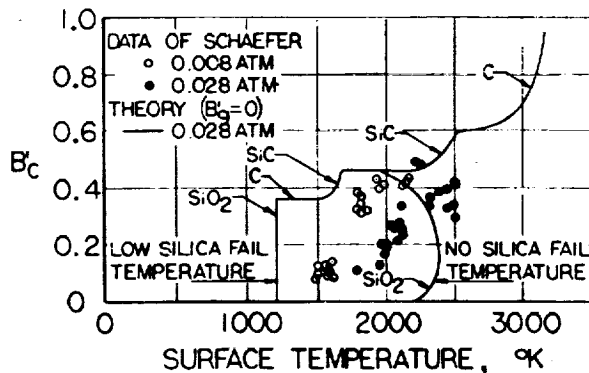


Figure 8. Correlation of Fissure Surface Thermochemistry Model with Ground Test Data

2.3 DISCUSSION OF RESULTS

There are two major conclusions which can be made on the basis of the results presented in Sections 2.1 and 2.2. First, there must be a mechanism for mechanical removal of silica since a number of the tests show substantial ablation at surface temperatures well below those corresponding to silica decomposition. A rate law for the mechanical removal of silica will be presented in Section 3. Secondly, there must be a means by which carbon is removed in excess of that which can be consumed by reaction with oxygen in the boundary layer and in the silica. Two possible mechanisms have been identified - the formation and mechanical removal of SiC^* and the loss of pyrolysis gases (which contain carbon which would otherwise have to react) because of fissures which form in the char.* Alternatively, carbon could erode mechanically and/or nitrogen could contribute to the ablation of the carbon. The question, then, is which of these models is physically the most realistic.

*The use of an empirical coking model as an alternative means for reducing the effects of blowing on the convective heating has been used with good success by Curry and Stephens (Ref. 7) in analyzing the results of the flight tests of the Apollo thermal protection system.

The subject of nitrogen attack of carbon is the most easily dealt with so it will be considered first. There has been a significant amount of data generated (e.g., Refs. 4 and 8) which show that the Apollo heat shield material ablates in nitrogen at approximately one-third the rate at which it ablates in air under otherwise similar conditions. There is also data (Refs. 4 and 8) which show that substantially less ablation takes place in helium. Thus, one must conclude that nitrogen contributes to the ablation process. However, there is an even larger body of data which would show that carbon does not react significantly with nitrogen in the surface temperature range of concern here - 1,500 to 2,500°K.

The effect of nitrogen might be as a catalyst to silica-carbon reaction which exhausts all the silica and a stoichiometric amount of carbon (the char being carbon-rich relative to reaction with silica). The severely weakened and now unreinforced carbon grains might then erode mechanically. This could occur even in the absence of significant external shear because of the stresses induced by the pyrolysis gases as they pass through the char. If this is what happens, the next question to ask is what the effect of nitrogen might be in the presence of oxygen when the environmental gas is air. Again, one can only conjecture, but one might suspect that the effect would diminish or even vanish since now the oxygen provides a means for removing the weakened carbon. In any event, one could conclude that the nitrogen effect is really nothing more than an identifiable type of chemically-induced mechanical removal.

With regard to the possibility of mechanical removal, the above discussion sheds some light. First, there is little or no erosion in helium. The small dimensional change that has been observed is usually attributed to shrinkage. Secondly, the mechanical removal in nitrogen is only about one-third of that in air so one would not expect an increase in ablation rate relative to the thermochemical contribution of more than this amount and, as has been stated previously, it might be expected to be considerably less since there is now a mechanism for removal of the weakened carbonaceous surface material by oxygen. Thus, mechanical removal of carbon is not believed to contribute more than, say, 10 to 20 percent to the surface ablation rate, if that.

This leaves the two possibilities discussed previously - mechanical removal of SiC* and/or a reduction of pyrolysis gas blowing effects as a consequence of fissures in the char. The data examined to this point do not permit a definitive choice between these models. Both envelop the Schaefer data between solutions with and without silica failing. Fissures have been observed in post-test chars but so have traces of SiC*. Intuitively, the fissure

model is somewhat more satisfying and thus is tentatively selected as being more likely. Correlations with flight test data using this model are presented in Section 4. First, however, a rate law for mechanical removal of silica at low surface temperatures is developed in Section 3.

SECTION 3

DEVELOPMENT OF RATE LAW FOR REMOVAL OF SILICA AT LOW SURFACE TEMPERATURES

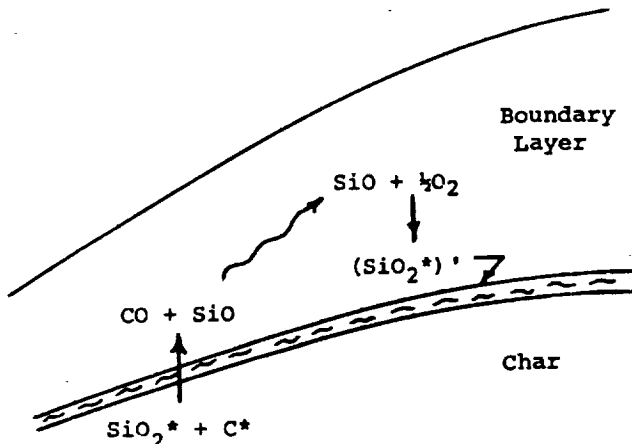
3.1 INTRODUCTORY REMARKS

Having tentatively adopted the fissure noncoking model (Figure 8) it remains to attempt to rationalize the experimental data which lie, for the most part, between the solutions for silica failing and not failing. Recalling that the use of a fail temperature provides a means for mechanical removal of a condensed species which wants to serve as the ablating surface, it is clear that some silica is removed mechanically but not so much as to permit diffusion-controlled ablation of carbon. The mechanical removal of silica from the Apollo heat shield material is believed to be a complex interrelationship between kinetically-controlled silica-carbon reactions, melting with subsequent liquid layer removal, and possibly mechanical erosion.

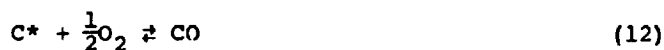
It is well known that there is an equilibrium potential for silica-carbon reactions at relatively low temperatures but that kinetics limit the rate at which this reaction proceeds below temperatures of 2,000°K or so. Thus a reaction such as Equation (3) is taking place in the char layer at and near the surface. However, in the surface temperature range for which a SiO_2^* recession model is desired, the SiO will react with oxygen from the boundary layer to reform condensed-phase silica, designated $(\text{SiO}_2^*)'$ to distinguish it from the original silica in the material



This process is illustrated in the following sketch.

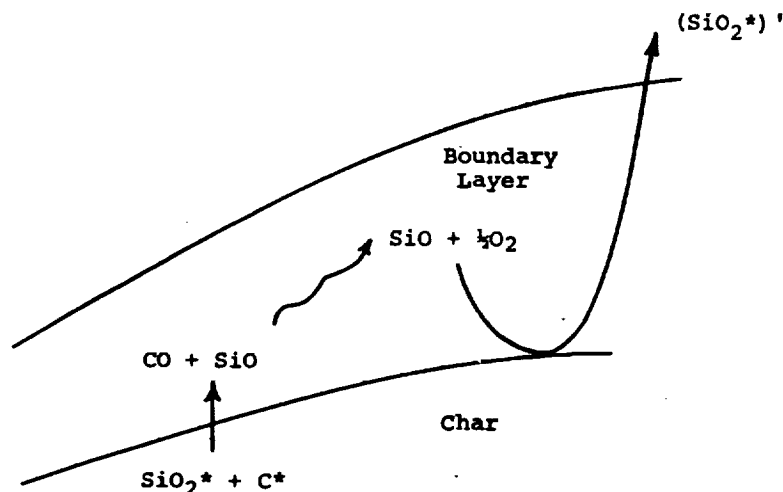


Thus in the actual case one would expect Reaction (3) to proceed at some finite rate and to act together with Reaction (11) to produce a net attack of the carbon by the oxygen in the boundary layer



This would be expected to produce a gradual buildup of a $(SiO_2^*)'$ layer over a receding subsurface consisting of the original SiO_2^* and C^* if the $(SiO_2^*)'$ that forms (or original SiO_2^* for that matter) does not flow or slough off.

One may well ask, then, why zero surface recession is predicted with the ACE program unless silica is removed mechanically. The answer lies in the fact that the ACE program considers only the surface and, at this surface, allows only one condensed phase to exist. In the ACE calculations reported in previous sections, there is no distinction made between SiO_2^* and $(SiO_2^*)'$. Therefore, if SiO_2^* is not allowed to fail, it is predicted to be the surface and zero surface recession is predicted since there is no mechanism for removing it. On the other hand, when a low SiO_2^* fail temperature is applied and the silica-carbon reaction is considered to proceed at an infinite rate, the $(SiO_2^*)'$ is removed as fast as it forms and the surface recession is limited by the rate that oxygen can diffuse to the surface to react with the carbon surface. This is illustrated in the following sketch:



Since the prediction of zero surface recession in the absence of a low silica fail temperature is the result of a limitation in the ACE program, it is well to perform independent calculations to ascertain whether or not surface recession can be explained on the basis of silica-carbon kinetics alone, with the net effect being the recession of an inner surface under a redeposited silica layer. This is done in Appendix E for the surface temperature range where a siliceous scab covers the surface (1,460 to 1,640°K). Applying generally accepted kinetic coefficients for silica-carbon reactions, it is shown therein that reaction rates are insufficient to explain surface recession rates in this surface temperature range on the basis of silica-carbon kinetics alone.

3.2 DEVELOPMENT OF RATE LAW FOR GROUND TEST DATA

In order to simulate the redeposited silica layer with the ACE program it is necessary to distinguish between the silica in the original material, say GLASS, and the redeposited silica, $(\text{SiO}_2^*)'$. The GLASS and $(\text{SiO}_2^*)'$ have identical properties with the exception that the latter has a low fail temperature and the former has a reduced entropy. (This artifice is introduced in order to achieve a one-way reaction.) The surface material GLASS is composed of the element GLASS and is allowed to communicate with the boundary-layer gases only through the one-way reaction



The $(\text{SiO}_2^*)'$ is composed of the conventional elements Si and O and is considered to be in equilibrium with the boundary-layer gases. In effect, then, the GLASS is considered to be converted to $(\text{SiO}_2^*)'$ at just that rate such that the $(\text{SiO}_2^*)'$ will fail so as to yield the experimentally observed B'_c . Since this model is predicated on the assumption that $(\text{SiO}_2^*)'$ is failing, it becomes inapplicable when the vapor pressure of SiO and Si become sufficient to vaporize all of the $(\text{SiO}_2^*)'$. That is, it is inappropriate to kinetically limit the decomposition of silica into gaseous products. Thus, it is employed only when it results in mechanical removal of $(\text{SiO}_2^*)'$.

In order to develop an analytical expression for a rate law for Reaction (13) the data of Figure 8 which lie to the left of the silica vaporization curves are plotted in Figure 9 as $\log (B'_c \sqrt{P})$ versus $1/T_v$. It can be seen that a straight line fits the data quite well. This linear curve can be represented in equation form by

$$B'_c \sqrt{P} = B \exp(-E_a/RT_w) \quad (14)$$

where $B = 4.24$ and $E_a = 19,000$ with T_w in $^{\circ}\text{K}$ and P in atmospheres.

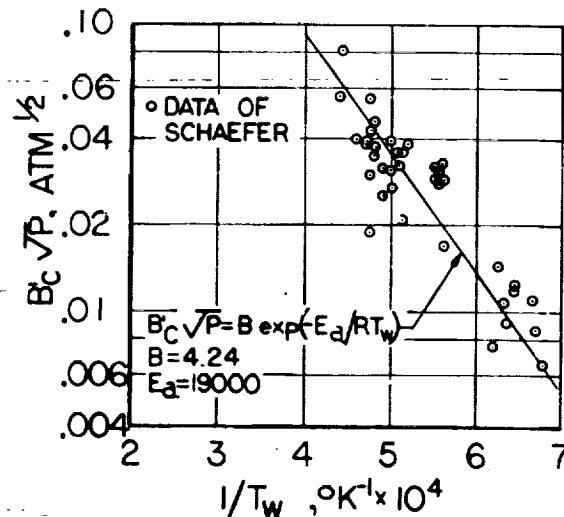


Figure 9. Correlation of Schaefer Ground Test Data in Terms of $B'_c \sqrt{P}$

ACE calculations were made considering this rate-controlled reaction and this rate law and the results are presented in Figure 10. It can be seen that the empirical fit of the low surface temperature data together with thermochemical ablation theory correlates the Schaefer data quite well.

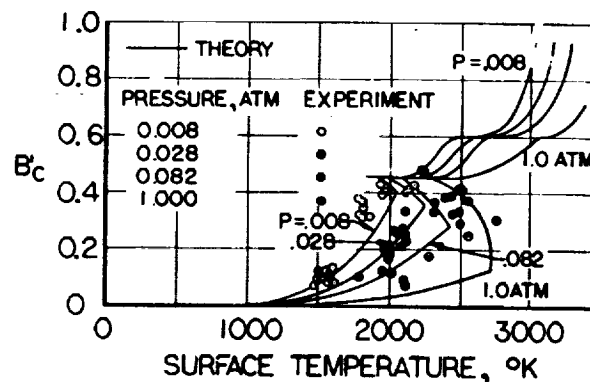
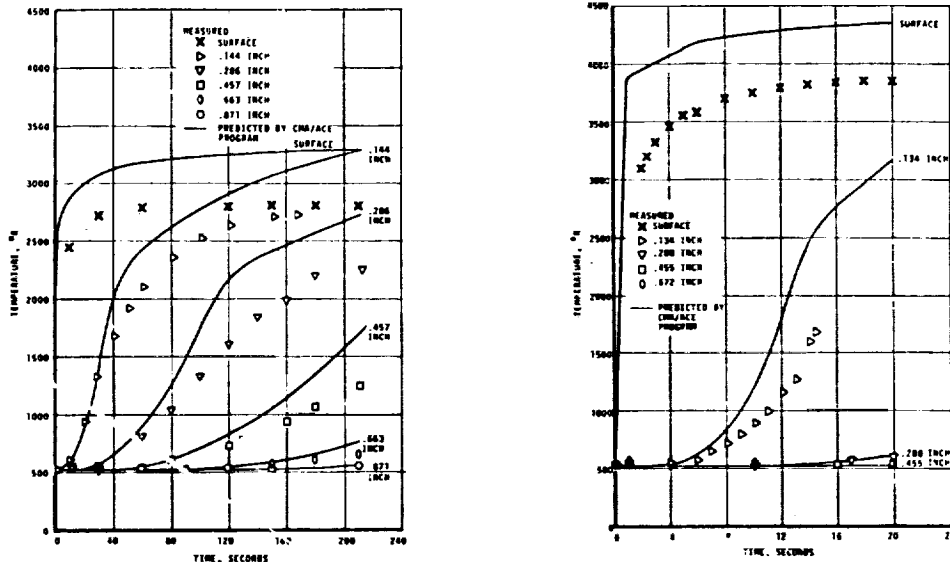


Figure 10. Comparison with Ground Test Data of Fissure Surface Thermochemistry Model Including $B'_c \sqrt{P}$ Correlation for Mechanical Removal of Silica

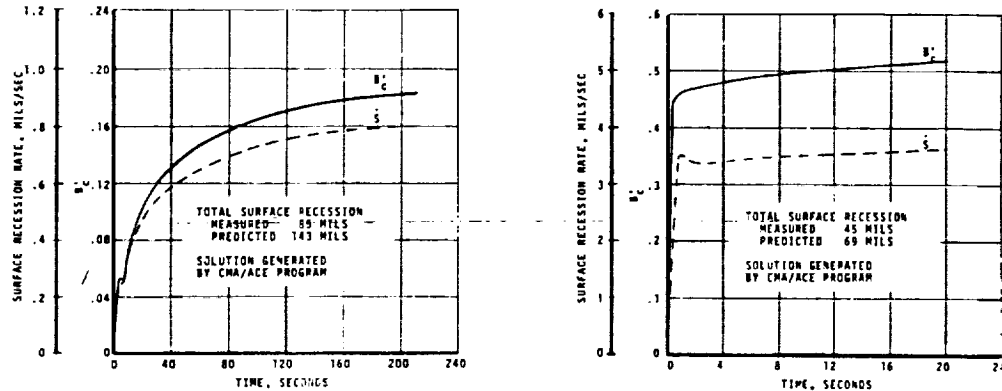
The above correlation is only a partial and approximate check on the validity of the fissure thermochemical ablation model. In the first place, the ACE correlations utilize the experimental surface temperature data which may be in error and which may differ from predicted temperatures because of imperfections in the material thermal properties model. Secondly, the correlation utilizes average ablation rates and surface temperatures whereas transient effects may be important in some cases. Thirdly, the calculation of $\rho_e u_e C_M$ from the \dot{S} needed to calculate the normalized ablation rates, B'_c , are only approximate. Therefore, transient ablation predictions were made using the Charring Material Ablation (CMA) program for two representative Schaefer test conditions and compared to the test data. The fissure model of Figure 10 was employed since it offered the best correlation in the ACE comparisons.

The two tests chosen for the correlation with CMA predictions were Models 114/BH/4.0 and 124/BH/4.0 (see Appendix C). These tests were chosen since they were accurately represented by the theoretical model. Thus any disagreement would reflect deviations from the experimental T_w and/or B'_c used in the ACE correlations. The predicted surface and in-depth temperatures for these two tests are compared to the measured values in Figure 11, while \dot{S} and B'_c predictions are presented in Figure 12.



(a) Model 114/BH/4.0 ($H_T = 4,910$ Btu/lb, $P_{T_2} = 0.0112$ atm, $\theta = 210$ sec) (b) Model 124/BH/4.0 ($H_T = 19,040$ Btu/lb, $P_{T_2} = 0.0279$ atm, $\theta = 20$ sec)

Figure 11. Comparison of Fissure Model Predictions for Surface Temperature with Measured Data for Two Schaefer Ground Tests



(a) Model 114/BH/4.0 ($H_T = 4,910$ Btu/lb, $P_{T_2} = 0.0112$ atm, $\theta = 210$ sec) (b) Model 124/BH/4.0 ($H_T = 19,040$ Btu/lb, $P_{T_2} = 0.0279$ atm, $\theta = 20$ sec)

Figure 12. Fissure Model Predictions for Surface Recession Rate for Two Schaefer Ground Tests

In the two tests considered, the surface temperatures are seen to be overpredicted by about 500°R . As a consequence, surface recession was substantially overpredicted since the solutions both fall in the temperature-sensitive rate-controlled silica-removal regime. Predictions for surface recession would be expected to be much better for more severe conditions where the B'_C is relatively insensitive to temperature.

It might appear to the reader that this overprediction is unacceptably large and that some modification of the thermal properties or surface thermochemical models is in order. This has not been done since the solutions are conservative with regard to thermal penetration and surface recession and some conservatism is demanded when it is recalled that the two tests considered here are represented accurately by the empirical silica-removal rate law, whereas there are a number of experimental data points that fall well above that rate law for a given T_w (see Figure 9). In addition, as mentioned previously, the overprediction in surface recession would be substantially reduced at higher surface temperatures where carbon plateau behavior is encountered. It is thus significant that in severe trajectories where surface recession would be critical, the temperature-sensitive rate-law regime is passed over quickly and most of the ablation takes place in the plateau region. Finally, it is felt that conservatism is especially warranted in a region where the ablation rate is strongly dependent upon temperature since if a considerable portion of the trajectory is spent in this temperature region, a small nonconservative error in heating rate, for example, could produce a large underprediction in ablation.

3.3 APPLICATION OF RATE LAW TO FLIGHT TEST CONDITIONS

Having now a satisfactory correlation of ground test data, one must ask whether this can be extended directly to flight conditions. The primary question to be resolved is whether the rate law for mechanical removal of silica should be applied to flight as B'_c versus T_w or as \dot{S} versus T_w .^{*} There is considerable distinction between these two approaches because of the order-of-magnitude difference in size between ground-test models and the full-scale Apollo vehicle. The correlation which has been presented is for B'_c versus T_w . The alternative of \dot{S} versus T_w was therefore also considered.

The data of Schaefer which lie to the left of the silica vaporization curves in Figure 8 are presented in Figure 13 as $\log \dot{S}$ versus $1/T_w$. It can be seen that the correlation is very similar to the correlation of $B'_c \sqrt{P}$ versus T_w of Figure 9. This is understandable since B'_c and \dot{S} differ only by $\rho_e u_e C_M$ which for stagnation-point flows is given approximately by

$$\rho_e u_e C_M \frac{C_H}{C_M} \frac{C_{H_2O}}{C_H} \approx K \sqrt{P/R'_{eff}} \quad (15)$$

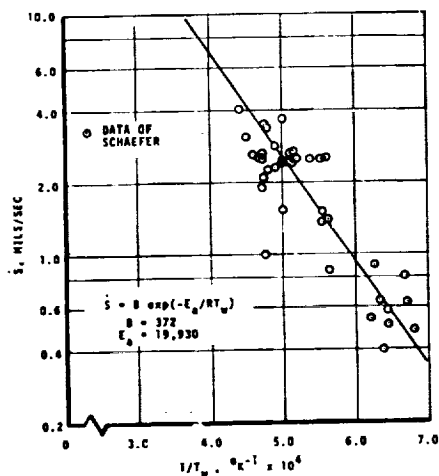


Figure 13. Correlation of Schaefer Ground Test Data in Terms of \dot{S}

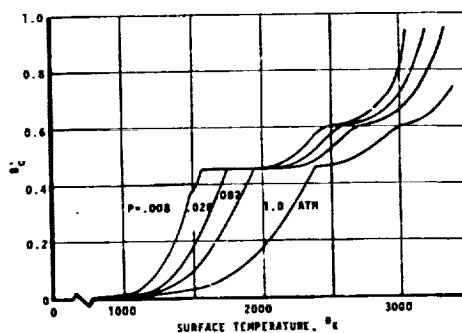


Figure 14. Surface Thermochemistry Map for Apollo Vehicle Based on \dot{S} Correlation of Ground Test Data

^{*} Studies performed by Curry and Stephens (Ref. 7) utilizing a \dot{S} - T_w correlation (also diffusion limited) in conjunction with an empirical rate law for coking and without considering fissures have yielded good agreement with flight data.

where K is nearly constant and R_{eff} is the effective nose radius. Therefore, for a given R_{eff} , \dot{S} is nearly proportional to $B'_C \sqrt{P}$ and the two correlations are equivalent. However, in going from ground to flight test conditions the correlations are vastly different because R_{eff} varies by more than an order of magnitude. To illustrate, application of the \dot{S} correlation of Figure 13 to the Apollo vehicle shape yields the ACE map of Figure 14. It can be seen that the \dot{S} correlation shifts the rate law to substantially lower surface temperatures. On the other hand, if $B'_C \sqrt{P}$ versus T_w were to be applied to flight, the ACE map of Figure 10 would be directly applicable.

If the empirical rate law were strictly a rate law representing the kinetics of the silica-carbon reaction and this reaction did not depend to any great extent upon melting or liquid removal, one might favor the \dot{S} correlation. However, it should be recalled that it is, rather, a rate law for representing the mechanical removal of silica. If melting is the controlling process then the B'_C correlation is probably more meaningful because the viscosity of silica is so strongly temperature-dependent. It is believed that something intermediate is the real situation, but that of the two extremes the B'_C correlation is somewhat more realistic.

In Section 4 the fissure model is applied to recent superorbital flight data using both approaches. The B'_C correlation results in substantial agreement for total recession and surface temperatures for the single body point and flight considered, whereas the \dot{S} correlation results in substantial overprediction of total recession.

SECTION 4

CORRELATION OF SURFACE THERMOCHEMISTRY MODELS WITH FLIGHT DATA

4.1 INTRODUCTORY REMARKS

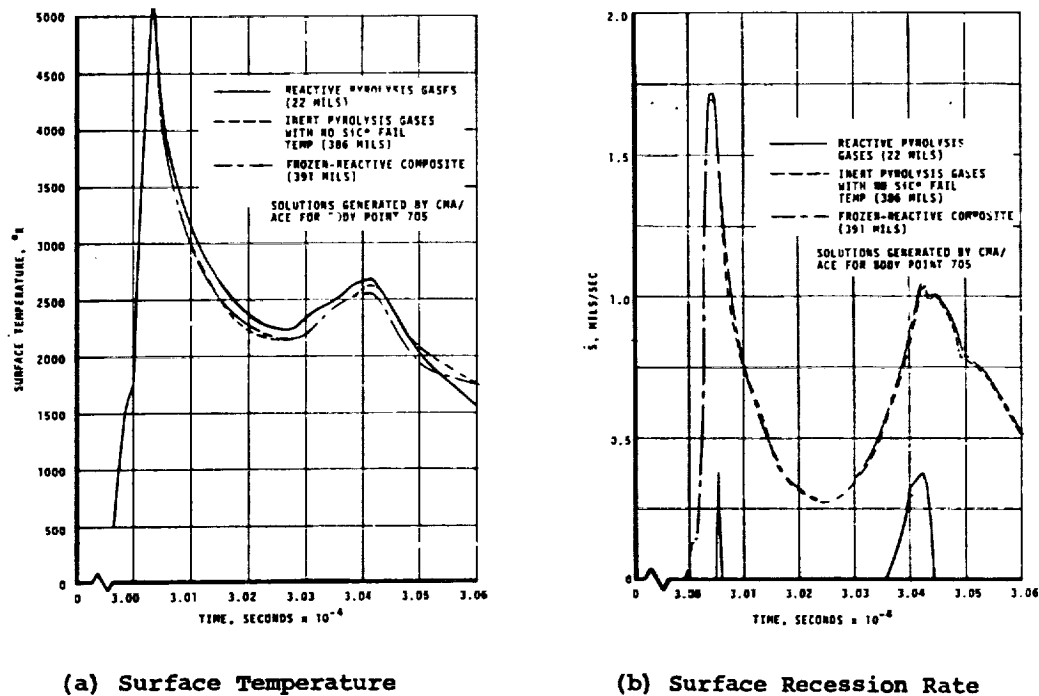
During the course of the present study, the various thermochemistry models described and subjected to ground-test data in Sections 2 and 3 were applied to superorbital flight data for the Apollo heat shield material. Unfortunately, an official (and presumed accurate) trajectory was not available until late in the study; therefore, several of the early calculations were performed with an unofficial trajectory which was markedly different from the official one. Also, these early calculations were performed with a preliminary set of material thermal properties. This was subsequently changed to agree with the best available data (see Appendix A) and this revised set was used for all subsequent calculations. Thus, the results of these early calculations are not quantitatively correct. They are useful, however, for qualitative comparisons of the models and provide indications of some important trends. In Section 4.2, results of some of these preliminary flight calculations are given. Flight predictions based on the correct trajectory and material property data are presented in Section 4.3.

4.2 PRELIMINARY FLIGHT CALCULATIONS

The trajectory information supplied by NASA-MSC for these preliminary studies included altitude, velocity, and stagnation point convective and radiative heat transfer rates as functions of time. Multiplication factors for heating rates and pressure at the point of interest (a position 1.31 feet downstream of the stagnation point along the windward ray) were also given. The recovery enthalpy, radiation flux, convective heat transfer coefficient and pressure, required as inputs to the CMA program, were calculated by standard procedures. Thirty time points were used to describe the trajectory.

In the heat shield material itself, a total of 36 nodes were used to describe the ablator depth of 1.988 inches. For convenience, an insulated backface was assumed. This proved to be adequate since no heatup of the rear-most nodes occurred. A laminar blowing reduction parameter was used. The ratio of mass-to-heat transfer coefficients was taken to be unity, and equal diffusion coefficients were considered in the boundary-layer. A planar geometry was assumed for all calculations.

The surface temperature and surface recession predictions for the reactive-pyrolysis-gas nonfissure model, the frozen-pyrolysis-gas nonfissure model, and a composite frozen/reactive-pyrolysis-gas nonfissure model are shown in Figure 15. A silica fail temperature of 900°K was used in these calculations. It is seen that although the surface thermochemistry models are quite different, the surface temperature is approximately the same for all cases. The major effect of the thermochemistry assumptions shows up in the predicted surface recession rates. The reactive pyrolysis gas model results in almost no surface recession, whereas the frozen and frozen/reactive composite models give about the same recession. Calculations were also performed for the composite-frozen/reactive-pyrolysis-gas model with a fail temperature of $1,400^{\circ}\text{K}$ rather than 900°K . The effect on surface temperature was again small, but the surface recession decreased from 391 to 194 mils. (The 900 and $1,400^{\circ}\text{K}$ fail temperatures were chosen as being indicative of \dot{S} and $B_c\sqrt{P}$ correlations, respectively.) Thus, it can be concluded, at least for this particular trajectory, that the surface recession is very sensitive to the particular thermochemical model and rate law which are employed, whereas the surface temperature is not.



(a) Surface Temperature (b) Surface Recession Rate
Figure 15. Predictions for Typical Superorbital Trajectory for Various Nonfissure Models and Low SiO_2^* Fail Temperature (900°K)

Another useful result of the preliminary studies is an insight into the partitioning of energy as it reaches the surface. Over a very large portion of the flight, approximately 75 percent of the energy reaching the surface is reradiated. Conduction into the material accounts for most of the remaining energy. The contribution to the various chemical ablation terms is negligibly small. Thus, the ability to predict surface temperature accurately depends primarily upon knowledge of the convective and radiative heating rates (including ablation effects on these rates) and the surface emissivity. As discussed in Appendix A, data in the literature indicate a value for surface emissivity of approximately 0.65 at relatively high temperatures. No data are available for lower temperatures where a glassy surface may bring about a lower emissivity or for very high temperatures where the emissivity may approach unity. A value of 0.65 was used for all predictions presented in this report.

4.3 FLIGHT PREDICTIONS USING OFFICIAL TRAJECTORY AND CURRENT MATERIAL PROPERTIES MODEL

For the flight predictions presented in this section, the best available flight trajectory* and material properties (Appendix A) were used. The trajectory parameters needed for the CMA program were calculated in the same manner as described in Section 4.2; the nodal network and other assumptions necessary to use the CMA program were also the same. For the flight and body point in question, a maximum stagnation point convective heat flux of nominally 300 Btu/ft²sec occurs at 30,040 seconds, and a maximum radiative flux of 160 Btu/ft²sec occurs at 30,030 seconds.

Figures 16 and 17 present flight prediction results for surface recession and temperatures, respectively, for two thermochemistry models, a non-fissure composite-frozen/reactive-pyrolysis-gas model and the fissure model. In both cases a conservative fail temperature of 900°K was considered. Also included in Figure 17 are the measured temperatures from on-board instrumentation (thermocouples) for the body point and flight considered. The measured temperatures of Figures 17(a) and 17(b) are subject to question since the 0.1 inch thermocouple was exposed by the receding surface for the latter part of the flight. Total predicted ablation for these cases was 620 mils**

*The details of this trajectory have not yet been released and therefore are not presented in this report.

**It is of interest to compare this to a prediction of 391 mils for the same surface thermochemical model for the old trajectory and material properties. This illustrates the sensitivity of the surface recession prediction to the trajectory.

for the composite nonfissure model and 788 mils with the fissure assumptions. Actual ablation for this flight was approximately 200 mils (Ref. 5). Temperatures in depth were also seriously overpredicted by the fissure model, although some of this overprediction can be attributed to the excessive ablation rates which were calculated. The higher ablation and higher temperatures for the fissure model can be attributed to the much smaller blowing correction on convective heat transfer to the body. In addition, the pyrolysis gas is not allowed to absorb as much energy with the fissure model.

The next logical step in testing the fissure model for the flight case was to employ the ACE map of Figure 14 which applies the Schaefer correlation to flight by means of an \dot{S} - T_w correlation. The results for temperatures and surface recession are shown in Figures 18 and 19, respectively. Total ablation

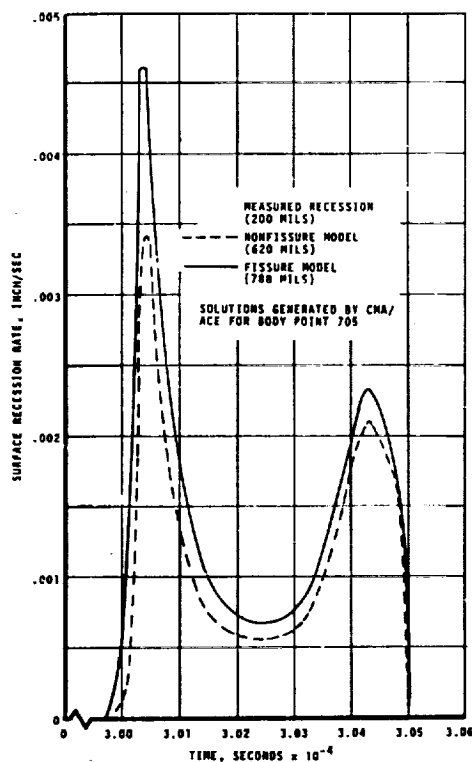
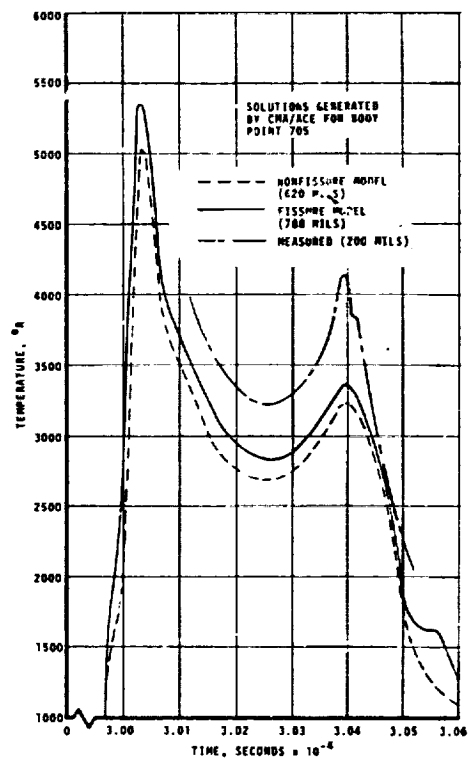
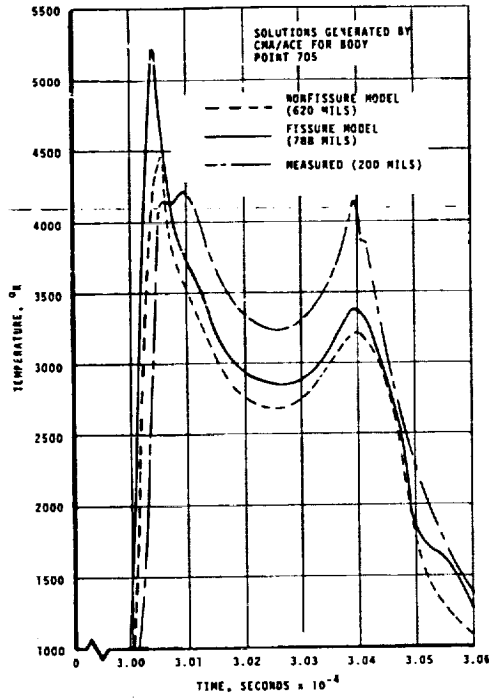


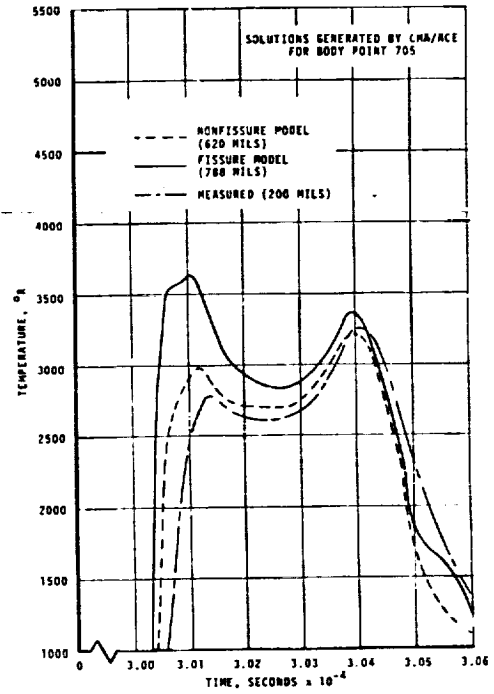
Figure 16. Surface Recession Rate Histories for Typical Superorbital Trajectory with Low SiO_2 * Fail Temperature (900°K) for Fissure and Nonfissure Models



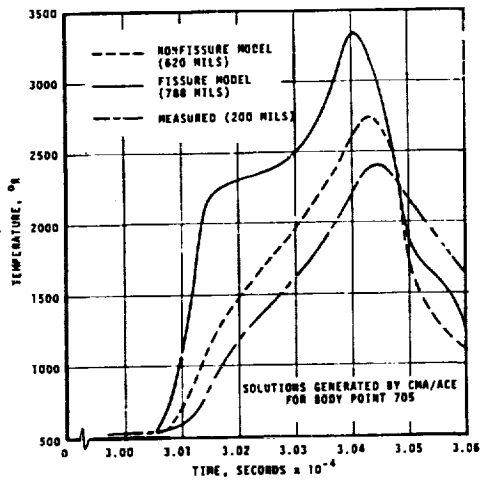
(a) Surface Temperature
Figure 17. Temperature Histories for Typical Superorbital Trajectory with Low Fail Temperature (900°K) for Fissure and Nonfissure Models



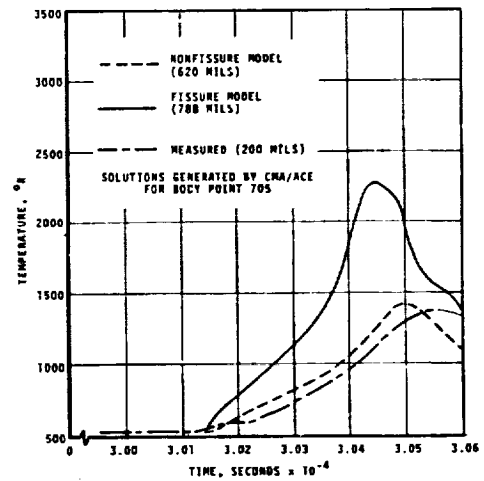
(b) 0.1 Inch from Initial Surface



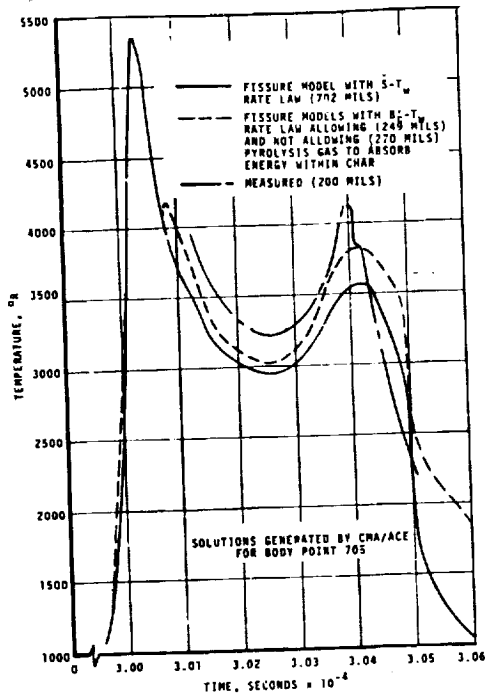
(c) 0.3 Inch from Initial Surface



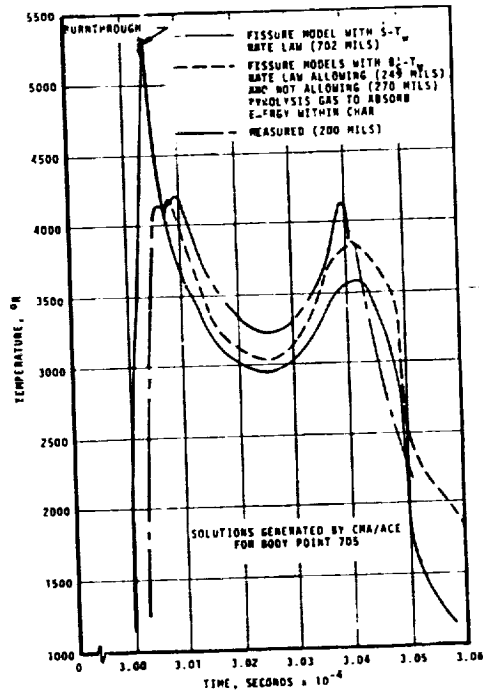
(d) 0.6 Inch from Initial Surface



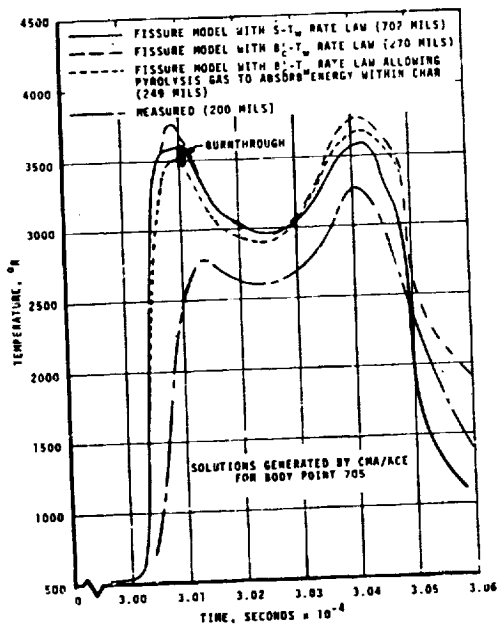
(e) 0.9 Inch from Initial Surface



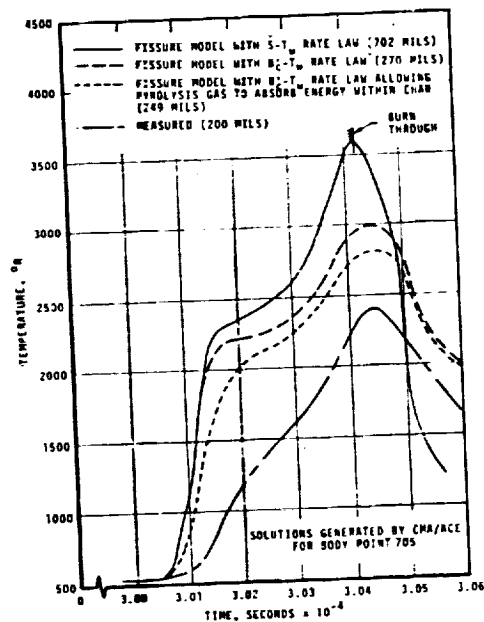
(a) Surface Temperature



(b) 0.1 Inch from Initial Surface

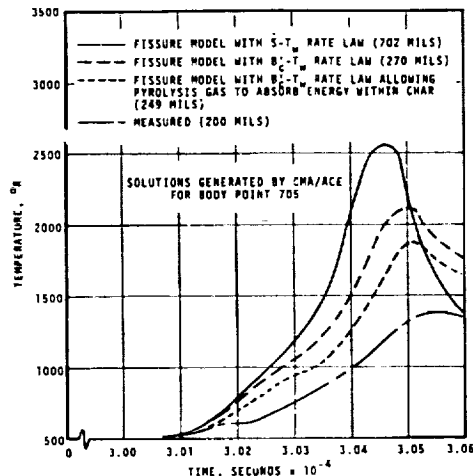


(c) 0.3 Inch from Initial Surface



(d) 0.6 Inch from Initial Surface

Figure 18. Temperature Histories for Typical Superorbital Trajectory with Fissure Model and Silica Mechanical Removal Rate Laws



(e) 0.9 Inch from Initial Surface
Figure 18. (concluded)

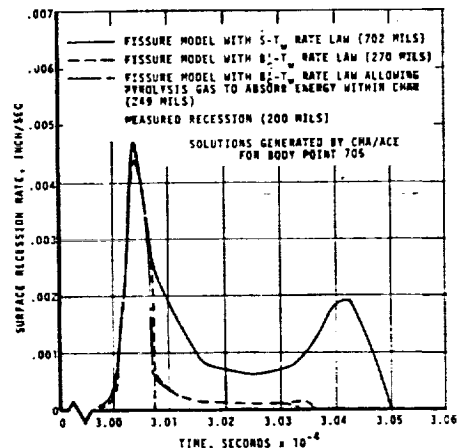


Figure 19. Surface Recession Rate Histories for Typical Super-orbital Trajectory with Fissure Model and Silica Mechanical Removal Rate Laws

for this case was 702 mils. While this is a slight improvement over the prediction considering fail temperatures (with fissures), it is still a gross overprediction. In addition, the in-depth temperatures are much too high, as can be seen in Figures 18(c), (d), and (e) (solid curves). Again a portion of this error can be attributed to the excessive ablation.

The cause for at least part of the excessive ablation can be attributed to the fact that the heat shield spends a large portion of the flight at temperatures ranging from 1,600-2,200°K and at pressures less than 0.1 atmospheres. With the \dot{S} - T_w ACE map of Figure 14, the ablation is forced to occur at the carbon plateau value throughout a substantial portion of the flight.

As discussed in Section 3.3, it is probably more consistent with physical intuition to apply the Schaefer B_c '- T_w correlation of Figure 10 directly to flight. This was done while retaining the fissure concept and the results are also shown in Figures 18 and 19 (long dashes). The most noticeable difference in these results is the much-reduced surface recession rate after the initial heating spike. Total recession for this case was 270 mils, compared with the measured value of 200 mils. This improved agreement is encouraging and lends some credence to the choice of the B_c '- T_w correlation. Surface temperatures also appear to be approximately correct, although little faith can

be placed in thermocouple readings after burnthrough. The one dismaying feature of this prediction is that in-depth temperatures, which are controlled by the total energy conducted into the material, are still several hundred degrees Rankine too high. Although the more realistic ablation depth helped bring temperatures down at depths of 0.6 and 0.9 inches, the effect was not enough. Apparently the energy conducted into the material during the initial heating spike is not as great as that allowed in the present model and must be reduced by some mechanism which was not accounted for.

One assumption which is overly-conservative in the fissure model employed in the above calculations is that the pyrolysis gas is not permitted to absorb any energy as it traverses the charred region. Even if one assumes that all gas passes rapidly through the fissures, some energy will be absorbed by it. To estimate the importance of this effect, the prediction just discussed was repeated with the conventional pyrolysis gas enthalpy table (see Table A-5 of Appendix A); this allowed the gas to absorb energy as if it were percolating through the char. The results are also included in Figures 18 and 19 (short dashes). It can be seen that the effect on in-depth temperatures, although distinguishable, is not a large one. Total ablation for this run was increased slightly (to 249 mils).

Reviewing the results that have been presented up to this point, it can be said that a successful modeling of the surface ablation rates and surface temperatures has been accomplished. The mechanical removal of silica as it is formed is described by a kinetic-type relation which controls the rate of silica removal consistent with the data of Schaefer applied to flight as $B'_c \sqrt{P}$ versus T_w . Vaporization of silica and equilibrium oxidation of the carbon surface as it appears are also included. The incorporation of the fissure assumptions gives a logical basis for assuming that the pyrolysis gas be treated as nonreactive and for disallowing the B'_g blowing correction. This model correlates the laboratory data of Schaefer quite well, and yields a satisfactory prediction of total surface recession and surface temperatures for the single body point that has been analyzed.

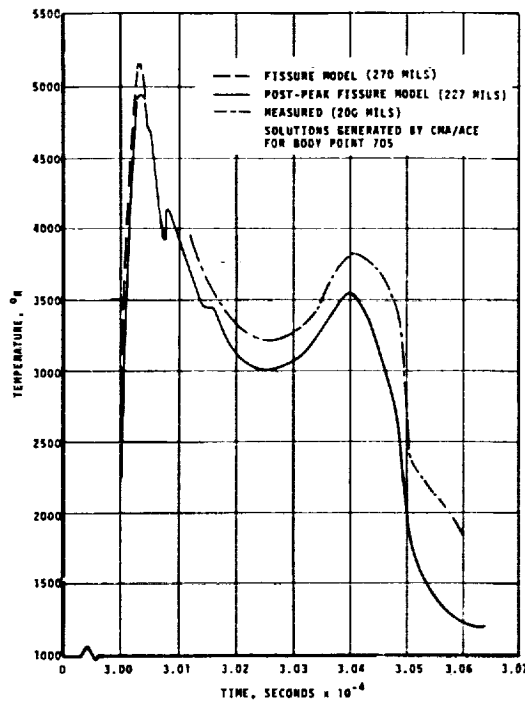
It appears, however, that the model is overly-conservative when it comes to predicting in-depth thermal response. Assuming that the thermal properties of the virgin material are roughly correct, the slopes of the temperature-versus-time curves at the various thermocouple locations indicate that too much energy is being conducted into the material. This can be attributed, in part, to the fact that the fissure model is a limiting case, disallowing a blowing correction caused by escaping pyrolysis gases. It is clear that even if all

pyrolysis gases were escaping through fissures, the resultant jet-boundary layer flow interaction would result in some attenuation of convective heating near each fissure. Thus the assumption of zero attenuation from pyrolysis gas blowing leads to overprediction of the heat transfer coefficient, overprediction of heat conducted into the body, and overprediction of ablation rates (for a given B'_C - T_w map). Furthermore, in the above calculations, the fissure model was applied throughout the entire flight, whereas fissures probably do not form until near peak heating. Pyrolysis gases formed during the period before fissures exist should therefore be allowed to attenuate heating.

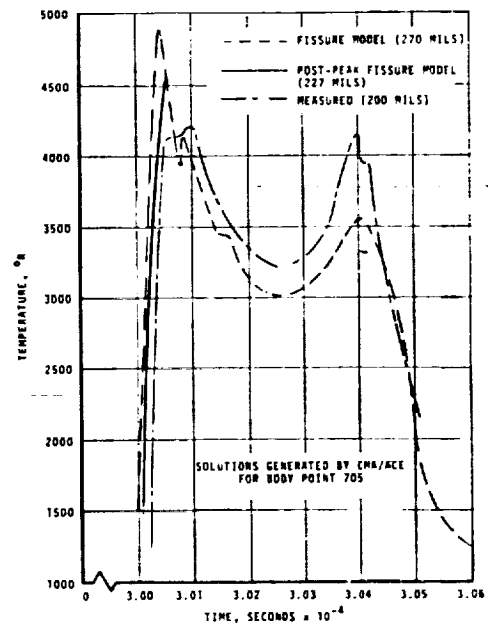
The changes necessary to fully implement such a "post-peak" fissure model are rather extensive; therefore, a relatively crude calculation was carried out. The post-peak fissure approximate predictions were made by calling the fissure option to the CMA program for the entire flight but utilizing altered (reduced) heat transfer coefficients up to peak heating to reflect the anticipated pyrolysis gas flow rate during this period of the trajectory.

The technique employed is not precise for a variety of reasons. First, the blowing rates used to alter the heat transfer coefficients were taken from the regular fissure model prediction, and thus are somewhat different from those which would be obtained for post-peak fissures. Secondly, the wall enthalpy terms, precisely valid only for $B'_g = 0$, were not altered; however, as mentioned earlier, the terms involving these quantities are relatively unimportant for the present problem. Thirdly, a complete B'_g dependent ACE map was not generated for the CMA program, whereas there is a minor effect of B'_g on the ACE map. Nevertheless, the calculations are believed to be sufficiently accurate to demonstrate the proper trends.

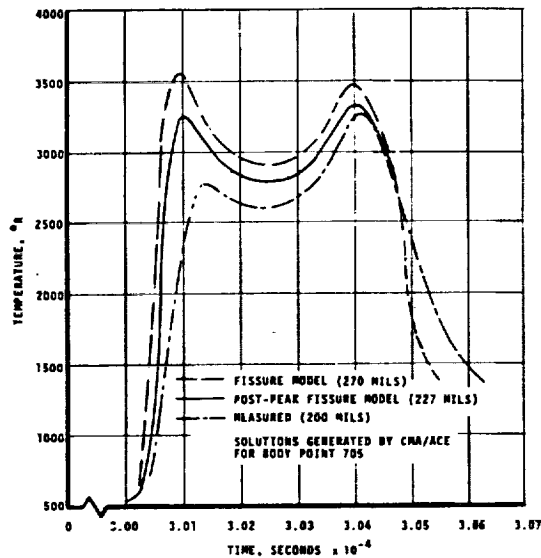
Temperature and surface recession predictions for the approximate post-peak fissure model are presented in Figures 20 and 21, respectively. The results obtained with the regular fissure model and the measured temperatures are also shown for comparison. Predicted total surface recession is decreased only slightly (to 227 mils) by considering fissures only after peak heating, whereas in-depth temperatures are significantly improved. Predictions are excellent at a depth of 0.9 inches and typically 200 to 400°R high at thermocouple locations nearer to the surface. This is consistent with the driver temperature calculations for flight and ground test reported in Appendix A and the ground test correlations presented in Section 3.2. Thus, any further refinements, if any, should probably be directed to the material properties model rather than to the surface thermochemical ablation model.



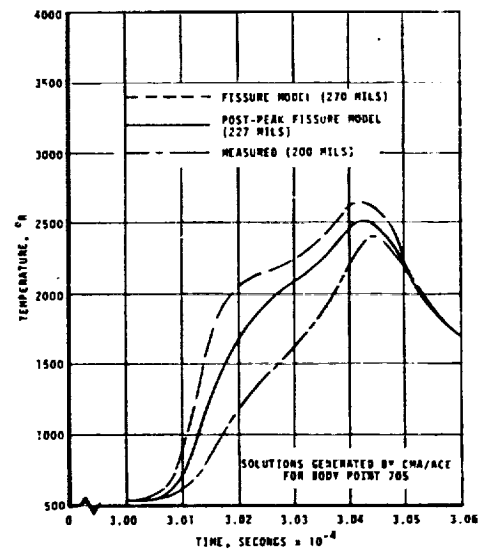
(a) Surface Temperature



(b) 0.1 Inch from Initial Surface

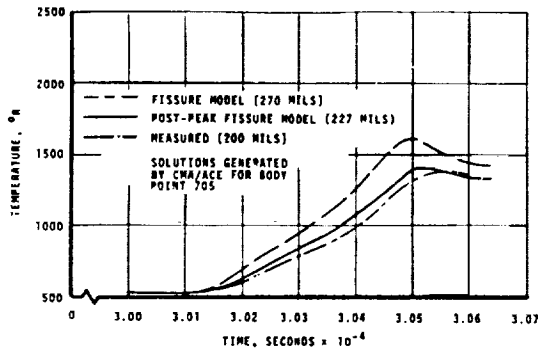


(c) 0.3 Inch from Initial Surface



(d) 0.6 Inch from Initial Surface

Figure 20. Temperature Histories for Typical Superorbital Trajectory with Fissure and Post-Peak Fissure Models



(e) 0.9 Inch from Initial Surface

Figure 20. (concluded)

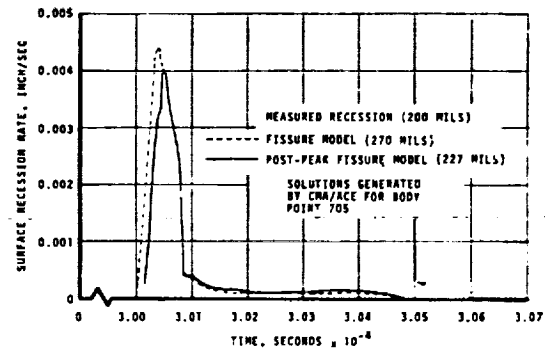


Figure 21. Surface Recession Rate Histories for Typical Super-orbital Trajectory with Fissure and Post-Peak Fissure Models

4.4 INTERIM SUMMARY

A systematic study of ground and flight test data for the Apollo heat shield material has been presented which would suggest two things: (1) at relatively low surface temperatures, mechanical removal of silica occurs which can be correlated by an Arrhenius-type relation, and (2) the pyrolysis gases are not effective in reducing convective heating (presumably as a result of fissures in the char). While this model correlates quite well the ground and flight test data which have been examined, it should not be inferred that this is necessarily the correct ablation model. It is not entirely clear whether the silica rate law should be interpreted as \dot{S} versus T_w or as $B'_C \sqrt{P}$ versus T_w (although the latter has been more effective in correlating flight data), and the behavior at high surface temperatures could be interpreted as mechanical removal of SiC^* and/or C^* rather than the result of nonuniform pyrolysis gas flow due to fissures. Nevertheless, the proposed model is believed to be sufficiently effective and credible to warrant further evaluation. Therefore, until analysis of additional data sheds further light, it is recommended that the fissure model with the $B'_C \sqrt{P}$ silica mechanical removal law be employed. The properties of this surface thermochemical ablation model are summarized in Appendix B.

SECTION 5

BOUNDARY LAYER (BLIMP) SOLUTIONS FOR THE APOLLO HEAT SHIELD MATERIAL

In Section 2 the Aerotherm Chemical Equilibrium (ACE) program was used to develop surface thermochemistry solutions for the Apollo heat shield material. These were correlated with ground test data in Sections 2 and 3 and with flight data in Section 4. The ACE program employs transfer coefficients which must be supplied as input and thus represents only a partial theory. In Section 5.2 boundary-layer solutions generated with the BLIMP program are presented to provide a check on the transfer coefficients employed in the flight predictions of Section 4. First, however, correspondence between the ACE and BLIMP programs is demonstrated in Section 5.1.

5.1 DEMONSTRATION OF CORRESPONDENCE BETWEEN BLIMP AND ACE PROGRAMS

Since the BLIMP and ACE programs employ the same surface thermochemistry relationships, they should provide identical solutions for the same assumed thermochemical ablation model. However, this has never been demonstrated. Therefore, BLIMP solutions were generated for models considered previously; in particular, the fissure model ($B'_g = 0$) and a nonfissure frozen-pyrolysis-gas model with a steady-state ratio of B'_g to B'_c . No silica fail temperature was considered in these calculations and SiC^* was permitted to be the surface species. The BLIMP solutions were generated for a given flight condition (total enthalpy of 25,000 Btu/lb and pressure of 0.028 atm) for the stagnation point of the Apollo vehicle. Surface thermochemistry maps were generated by assigning a series of \dot{m}_c (and corresponding values of \dot{m}_g for the nonfissure solutions) such as to cover the entire range of interest and requiring that surface equilibrium be satisfied.* The solutions thus yielded surface temperatures and the $\rho_e u_e C_M$ needed to compute B'_c - T_w maps. The BLIMP solutions are compared in Figure 22 to the appropriate ACE solutions presented previously. It can be seen that the correspondence is indeed precise.

*The same curves of B'_c versus T_w would be generated by the BLIMP program for a different enthalpy C but the same pressure; however, injection rates would have to be adjusted for the different $\rho_e u_e C_M$ which would result in order to obtain solutions for the same range of B'_c .

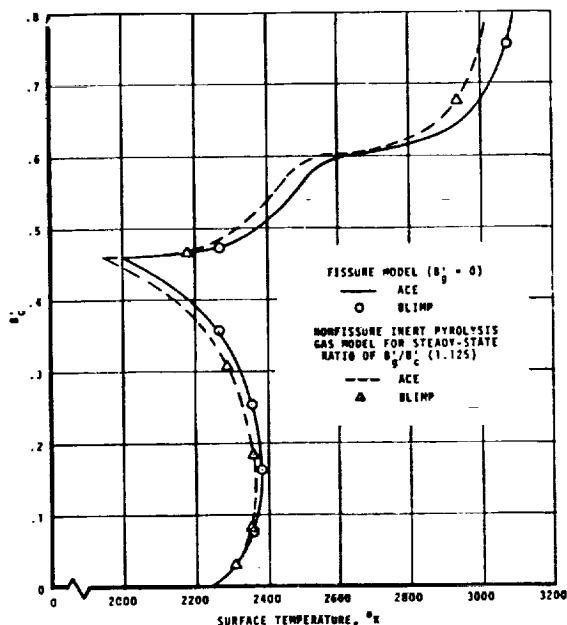


Figure 22. Comparison of Surface Thermochemistry Maps for Fissure and Nonfissure Models without Low Silica Fail Temperature as Generated by BLIMP and ACE Programs

It has thus been demonstrated that the ACE program yields the same surface thermochemistry maps as the boundary layer (BLIMP) program, but that the BLIMP program provides, in addition, a prediction for the $\rho_e u_e C_M$. The BLIMP program also provides boundary layer profiles and other auxiliary information. To illustrate, profiles of velocity ratio, temperature, and elemental mass fractions considering the nonfissure model with steady-state ratio of B'_g to B'_c are presented in Figures 23 through 25, respectively, for char mass ablation rates of 4.0×10^{-5} and 1.0×10^{-3} lb/sec-ft², corresponding to relatively low and high B'_c of 0.031 and 3.30, respectively.

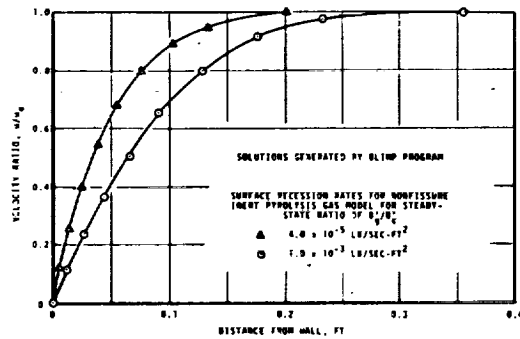


Figure 23. Velocity Profiles in Boundary Layer over Ablating Apollo Heat Shield ($H_T = 25,000$ Btu/lb, $P_{T2} = 0.028$ atm, Nonfissure Model)

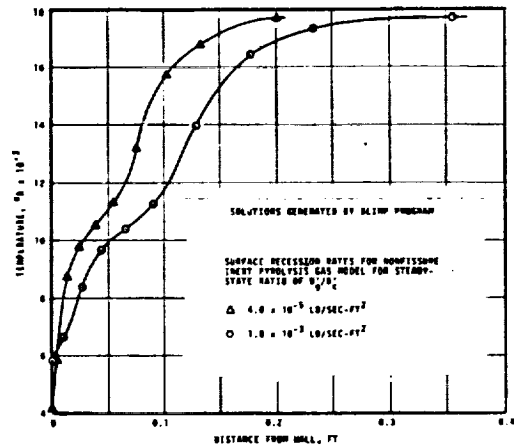


Figure 24. Temperature Profiles in Boundary Layer over Ablating Apollo Heat Shield ($H_T = 25,000$ Btu/lb, $P_{T2} = 0.028$ atm, Nonfissure Model)

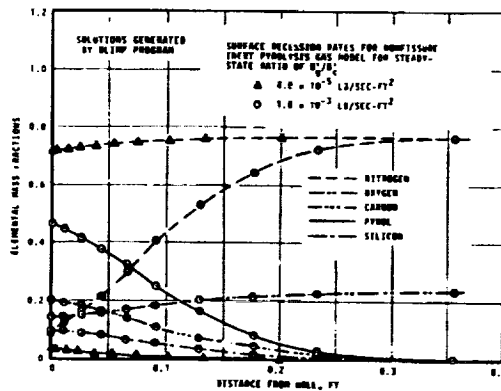


Figure 25. Elemental Mass Fraction Profiles in Boundary Layer over Ablating Apollo Heat Shield ($H_T = 25,000$ Btu/lb, $P_{T2} = 0.028$ atm, Nonfissure Model)

5.2 FLIGHT PREDICTIONS PERFORMED WITH THE BLIMP PROGRAM

In Section 4 the CMA/ACE approach was utilized to provide transient ablation predictions for the Apollo heat shield subjected to typical super-orbital entry conditions. In this approach, nonablating convective and radiative heat transfer rates are employed together with laws relating C_H to C_{H_0} and C_M to C_H . Heating rate data supplied by NASA MSC were used directly in these calculations. In this section, nonsimilar laminar boundary-layer solutions, generated with the BLIMP program, are discussed to assess the validity of the $\rho_e u_e C_{H_0}$, C_H/C_{H_0} and C_M/C_H employed in the CMA/ACE calculations. First, nonablating heat- and mass-transfer coefficients obtained with the BLIMP program are presented for several trajectory times. Then two types of ablation solutions are presented for the peak heating condition (30,030 sec). These approaches both consider surface equilibrium and perform surface mass balances but differ as follows: the first considers a surface energy balance for steady-state conduction into the body and a steady-state ratio of B'_g to B'_c , while the second gives no consideration to an energy balance but uses char and pyrolysis gas injection rates assigned at the levels predicted in the transient CMA/ACE solutions.

The body station considered in Section 4 was located on the windward ray 1.31 feet downstream of the stagnation point. Therefore, it is necessary to perform nonsimilar boundary layer solutions from the stagnation point up to this station.* The pressure distribution which was employed and the resulting pressure-gradient parameter (β), computed and used by the BLIMP program, are presented in Figure 26.

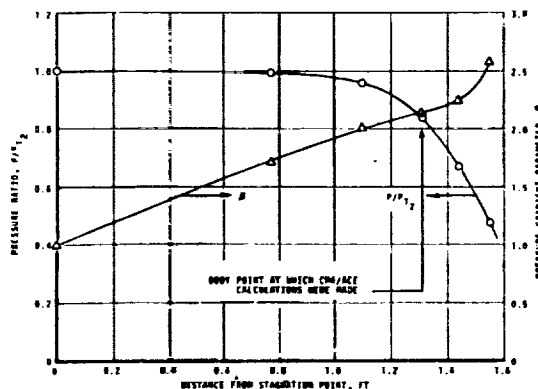


Figure 26. Pressure Ratio and Pressure Gradient Parameter Along Apollo Windward Ray for Typical Super-orbital Trajectory

* In the CMA/ACE approach this is not needed since local convective transfer coefficients are employed.

Distributions of heat- and mass-transfer coefficients around the body up to and slightly past the 1.31 foot station as predicted by the BLIMP program are presented in Figures 27 and 28, respectively, for trajectory times of 30,030, 30,045, 30,070, 30,240, and 30,430 seconds. Heat-transfer coefficients supplied by NASA MSC and used in the CMA/ACE calculations of Section 4 are also shown in Figure 27 for comparison. It can be seen that the BLIMP predictions are about 55 to 65 percent lower in the stagnation region but 35 to 55 percent higher at 1.31 feet, the station at which the CMA/ACE solutions were performed.*

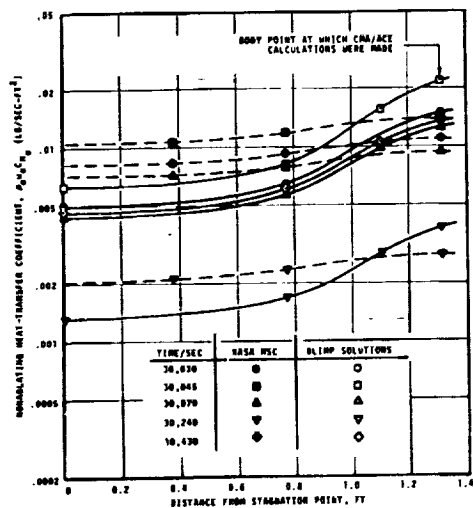


Figure 27. Comparison of Nonablating Heat-Transfer Coefficients along Apollo Windward Ray as Supplied by NASA-MSC and Computed by BLIMP for Typical Superorbital Trajectory

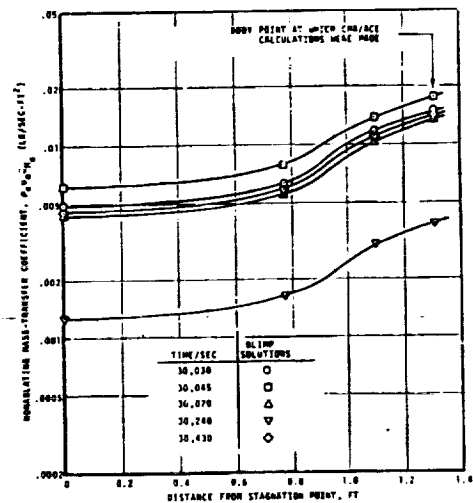
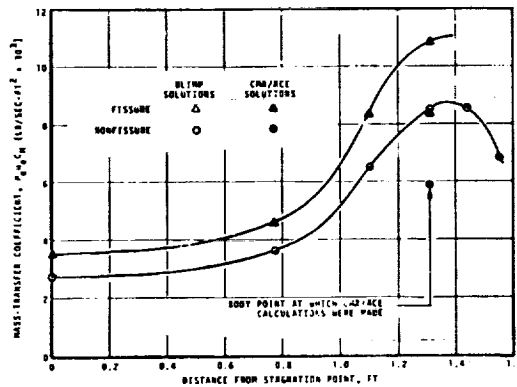


Figure 28. Distributions of Nonablating Mass-Transfer Coefficients along Apollo Windward Ray for Typical Superorbital Trajectory

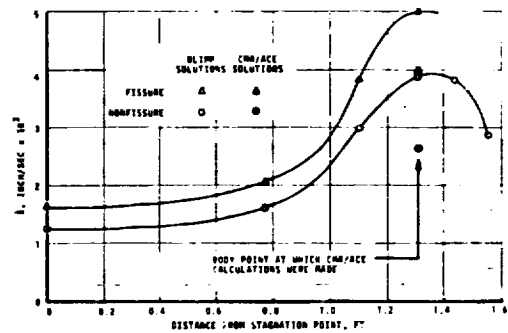
Distributions of $\rho_e u_e C_M$, \dot{S} , and surface temperature predicted by the BLIMP program considering a steady-state energy balance are presented in Figure 29 for fissure and nonfissure (frozen pyrolysis gas) models for a trajectory time of 30,030 seconds. The CMA/ACF predictions for station 1.31 feet are also

*These calculations were performed late in the program; hence, there was no opportunity to resolve these discrepancies.

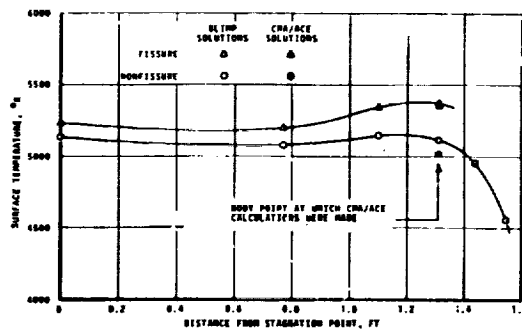
shown for comparison. It can be seen that the approximately 40 percent discrepancy in $\rho_e u_e C_{H_2O}$ of Figure 27 is maintained in the hot-wall, ablating values for $\rho_e u_e C_H$. The discrepancy in \dot{S} at 1.31 feet, shown in Figure 29(b), is nearly the same. The reason for this is that the energy balance which was performed, taking all of the (apparently) compensating factors into account, resulted in only a slightly different B'_c so that the \dot{S} is nearly proportional to $\rho_e u_e C_M$. Likewise, the surface temperature predicted by BLIMP, shown in Figure 29(c), also agrees quite closely with the CMA/ACE prediction.



(a) Mass-Transfer Coefficient



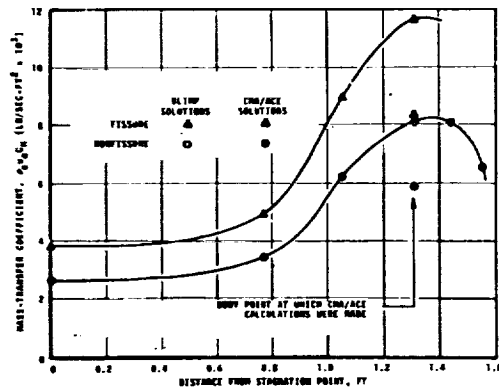
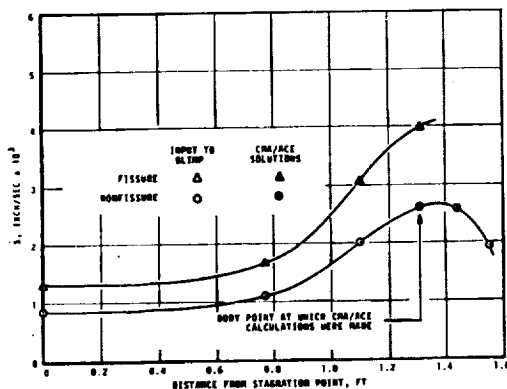
(b) Surface Recession Rate



(c) Surface Temperature

Figure 29. Boundary Layer Solutions along Apollo Windward Ray for Fissure and Nonfissure Models Considering Steady-State Surface Energy Balances for Typical Superorbital Trajectory (Time = 30,030 sec)

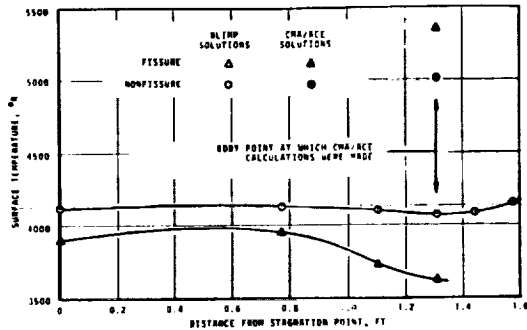
BLIMP solutions for fissure and nonfissure models at peak heating (30,030 sec) based on assigned distributions of \dot{m}_c and \dot{m}_g are presented in Figure 30. The \dot{m}_g and \dot{m}_c were taken to agree with the CMA/ACE solutions at the 1.31 foot station and to vary around the body in the same manner as the steady-state energy balance solutions (see Figure 29(b)). The resulting input distributions of \dot{S} are shown in Figure 30(a). Again, consistent with Figures 27 and 29(a), the $\rho_e u_e C_M$ at the 1.31 foot station predicted by the BLIMP program are substantially higher than those values input to the CMA/ACE program. This is shown in Figure 30(b). As a consequence of these different $\rho_e u_e C_M$, the BLIMP predictions for surface temperature, shown in Figure 30(c), are very low. The reason for this can be seen by examination of Figure 22. The B'_c predicted by the CMA/ACE program were approximately 0.60. The higher $\rho_e u_e C_M$ in the BLIMP solutions result, for the same \dot{S} , in B'_c of about 0.45, and thus the solutions fall on the silica vaporization leg of the B'_c - T_w curve. It is important to note that there are very large energy imbalances in these solutions - if an energy balance would have been performed, the \dot{S} would have adjusted upward in accordance with the higher $\rho_e u_e C_M$.



(a) Surface Recession Rate

(b) Mass-Transfer Coefficient

Figure 30. Boundary Layer Solutions along Apollo Windward Ray for Fissure and Nonfissure Models for Injection Rates Predicted by CMA/ACE for Typical Superorbital Trajectory (Time = 30,030 sec)



(c) Surface Temperature
Figure 30. (concluded)

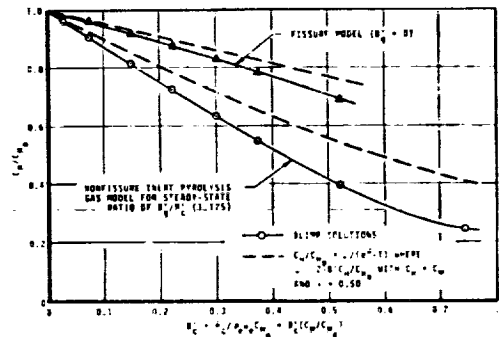


Figure 31. Variation of C_M/C_{M_0} for Fissure and Nonfissure Models ($H_T = 25,000$ Btu/lb, $P_{T2} = 0.028$ atm)

The results of these boundary-layer calculations are summarized in Table V. The major conclusion is that the $\rho_e u_e C_{H_0}$ obtained from NASA MSC and used in the CMA/ACE solutions differ from the $\rho_e u_e C_{H_0}$ computed by BLIMP by about 40 percent. It is also seen that C_M/C_H is very nearly unity as was assumed in the CMA calculations. Finally, the C_M/C_{M_0} calculated by CMA and BLIMP agree very well. However, this is an unfair comparison because of the higher $\rho_e u_e C_{M_0}$ in the BLIMP calculations. Therefore, the values of C_M/C_{M_0} predicted in the series of BLIMP solutions presented in Section 5.1 for fissure and nonfissure models at a given flight condition (25,000 Btu/lb and 0.028 atm) and for a large range of injection rates are compared in Figure 31 to the values which would be predicted by CMA for the value of the blowing reduction parameter, λ , of 0.50 (see figure) which was used in this report. It is seen that mass addition is about 25 to 35 percent more effective in reducing the mass transfer than was considered in the CMA calculations. This situation could be improved simply by increasing the value of the blowing reduction parameter which is an input parameter to the CMA program.

In conclusion, it is deemed appropriate to attempt to resolve the reason for the discrepancy between the $\rho_e u_e C_{H_0}$ supplied by NASA MSC and the values computed by the BLIMP program. It would also be desirable to evaluate the attenuation of the incident radiation flux by ablation products using a radiation coupled boundary layer solution procedure. It is only after such studies as these that repetition of the calculations of Section 4 with revised convective and radiative heat fluxes would be warranted. In the meantime, the results of Section 4 should be considered in the light of the results of the present section.

TABLE V
COMPARISON OF BLIMP AND CMA/ACE SOLUTIONS FOR
A TYPICAL SUPERORBITAL TRAJECTORY AT PEAK HEATING

	FISSURE MODEL			NONFISSURE MODEL		
	CMA/ ACE	BLIMP (ASSIGNED INJECTION RATES)	BLIMP (WALL ENERGY BALANCE PERFORMED)	CMA/ ACE	BLIMP (ASSIGNED INJECTION RATES)	BLIMP (WALL ENERGY BALANCE PERFORMED)
$\rho_e u C_H \times 10^2$ lb/sec-ft ²	1.08*	1.480	1.480	1.08*	1.480	1.480
C_H/C_{H_0}	0.775	0.796	0.724	0.548	0.562	0.579
$\rho_e u C_H \times 10^2$ lb/sec-ft ²	0.836	1.178	1.071	0.591	0.833	0.857
C_W/C_H	1.000*	0.992	1.012	1.000*	0.971	0.996
$\rho_e u C_M \times 10^2$ lb/sec-ft ²	1.08	1.487	1.487	1.08	1.487	1.487
C_W/C_{M_0}	0.775	0.785	0.730	0.548	0.545	0.574
$\rho_e u C_M \times 10^2$ lb/sec-ft ²	0.836	1.168	1.085	0.591	0.809	0.854
$\dot{S} \times 10^3$, in/sec	4.00	4.00*	5.01	2.63	2.63*	3.88
B'_C	0.636	0.457	0.616	0.590	0.433	0.605
B'_L	0.636	0.457	0.616	2.016	1.479	1.288
T_w , °R	5356	3624	5372	5018	4076	5123

*Assigned Values

SECTION 6

CONCLUSIONS AND RECOMMENDATIONS

A number of thermochemical ablation models have been presented for the Apollo heat shield material in the form of normalized surface recession rates, B'_c , versus surface temperature with pressure and normalized pyrolysis gas rate, B'_g , as parameters. The models differ primarily with regard to the treatment of nonequilibrium and mechanical removal effects. These normalized ablation tables were subjected to ground test data over a wide range of environmental conditions. Transient in-depth ablation calculations were then made for some of the test conditions for the theoretical model which appeared to correlate the data best in the normalized ablation plots. It was seen that when the actual energy balance was solved the predictions for thermal penetration and surface recession were conservative to the extent deemed appropriate.

With these correlations judged satisfactory, several of the thermochemical ablation models were subjected to superorbital flight data for the Apollo heat shield material. It was seen that good correlations of surface recession and surface temperatures could be achieved, but it was also seen that the predictions are very sensitive to various parameters of the problem. The thermal penetration was overpredicted somewhat, but this is consistent with calculations which were performed for both flight and ground test data where surface temperatures (or temperatures indicated by thermocouples near the surface) were used as driver temperatures. Since the predicted thermal penetration was again conservative, the thermal property model (which is based entirely on laboratory data obtained from precharred samples) was retained.

The parameters judged to be the most important in flight predictions are surface emissivity, radiative and convective cold-wall heating rates, blowing reduction, and radiation blocking by ablation products. The correlations were accomplished using the value for surface emissivity (0.65) and the heating rates supplied by the NASA MSC contract monitor. No checks of radiative heating rates or radiation blocking were made in the present study, but boundary layer solutions were performed which suggested that convective heating rates might be as much as 40 percent higher than those used in the present study. It was found appropriate that no blowing correction for the pyrolysis gas should be applied, at least after the first peak heating. The grounds for this argument are contained in the physical observation that chars produced in both flight and ground tests possess fissures leading from the

pyrolysis zone to the char surface. Thus, it is reasonable to suspect that the pyrolysis gases may for the most part jet through the boundary layer with little attenuation of the convective heating.

The model which appears to correlate the flight data best also provides the best correlation for the ground test data. In addition to the consideration of fissures, this model has the following major features. At low surface temperatures, it contains an empirical Arrhenius-type law for pressure-dependent B'_C versus surface temperature. This is not a chemical kinetic law, but is, rather, a law for the mechanical removal of silica. At higher surface temperatures, the surface recession is limited by the availability of oxygen (diffusion-controlled carbon ablation regime). The oxygen supplied by the boundary-layer edge gas is supplemented by oxygen in the silica. Finally, at very high temperatures, carbon reactions with nitrogen and carbon sublimation become important.

In order to gain further confidence in this model, it is recommended that further studies of the type reported herein be performed for other available flight data. Also, independent checks of radiative heating rates and further checks of convective heating rates should be performed for flight test conditions using the best available theoretical prediction procedures. Independent theoretical and experimental studies of such important considerations as in-depth coking and the effect of char fissures on the interaction of the pyrolysis gases with the boundary layer should be carried out and the results should be incorporated into the computational procedures. Finally, a series of arc-plasma experiments should be conducted which are especially designed with regard to model shape and size to assess whether \dot{S} or B'_C is the more basic parameter in applying ground test data to flight in the region where mechanical removal of silica controls the ablation process.

REFERENCES

1. Kendall, R. M.: A General Approach to the Thermochemical Solution of Mixed Equilibrium-Nonequilibrium, Homogeneous or Heterogeneous Systems. NASA CR-1064, Aerotherm Corporation, Mountain View, California, June 1968.
2. Kendall, R. M. and Bartlett, E. P.: Nonsimilar Solution of the Multicomponent Laminar Boundary Layer by an Integral Matrix Method. AIAA Journal, Vol. 6, No. 6, pp. 1089-1097, June 1968.
3. Moyer, C. B. and Rindal, R. A.: Finite Difference Solution for the In-Depth Response of Charring Materials Considering Surface Chemical and Energy Balances. NASA CR-1061, Aerotherm Corporation, Mountain View, California, June 1968.
4. Schaefer, J. W., Flood, D. T., Reese, J. J., Jr., and Clark, K. J.: Experimental and Analytical Evaluation of the Apollo Thermal Protection System under Simulated Reentry Conditions. Report No. 67-16, Parts I and II, Aerotherm Corporation, Mountain View, California, July 1967.
5. Alexander, J. G., et al: Evaluation of the Thermophysical Properties of the Apollo Heat Shield AS-501 Flight Core Study. AVSSD-0206-68-RR, AVCO Space Systems Division, Wilmington, Mass., July 1968.
6. Ihnat, M. E.: Evaluation of the Thermophysical Properties of the Apollo Heat Shield. AVSSD-0375-67-RR, AVCO Space Systems Division, Wilmington, Mass., August 1967.
7. Curry, D. M. and Stephens, E. W.: Apollo Ablation Performance at Super-orbital Entry (U). Presented at the AIAA Entry-Vehicle Systems and Technology Conference, Williamsburg, Virginia, Dec. 3-5, 1968.
8. Mauk, C. F. and Altenburg, R. A.: Calculation of Convective and Radiative Ablation Rates. Memorandum Report, Houston Research Inst., Inc., Houston, Texas, September 1965.

APPENDIX A
APOLLO HEAT SHIELD MATERIAL PROPERTIES
USED IN THE PRESENT STUDY

APPENDIX A

APOLLO HEAT SHIELD MATERIAL PROPERTIES USED IN THE PRESENT STUDY

A.1 DESCRIPTION OF MATERIAL

The Apollo heat shield consists of a low density ablation material bonded to a primary structure. The low density ablation material is Avcoat 5026-39/HC-GP, an epoxy novolac resin with phenolic microballoons and silica fiber reinforcement in a fiberglass honeycomb matrix. Although the epoxy-honeycomb combination maintains its cellular appearance after fabrication, the virgin material is treated theoretically as a continuum with uniform thermal and mechanical properties. Overall density of the virgin ablation material is taken to be 34.0 lb/ft³.

Upon being subjected to sufficiently high heating, the Avcoat material decomposes chemically forming a pyrolysis gas and a char residue. Based upon chemical and thermogravimetric analysis data supplied by NASA MSC, the elemental composition of the pyrolysis gas and char is taken to be as indicated in Table A-1.

TABLE A-1
CHAR AND PYROLYSIS GAS ELEMENTAL MASS FRACTIONS
IN AVCOAT 5026-39/HC-GP

<u>Element</u>	<u>Pyrolysis Gas</u>	<u>Char</u>
H	0.0930	--
B	--	0.0079
C	0.5470	0.4880
N	0.0190	--
O	0.3410	0.2605
Al	--	0.0212
Si	--	0.1852
Ca	--	0.0366

These compositions are based on a pyrolysis gas density of 18.0 lb/ft³ and a char density of 16.0 lb/ft³, where the char is composed of the compounds listed in Table A-2. It was found convenient in the present study to

TABLE A-2

CHAR SPECIES MASS FRACTIONS

Species	Mass Fraction
C*	0.4880
SiO ₂ *	0.3971
Al ₂ O ₃ *	0.0384
CaO*	0.0510
B ₂ O ₃ *	0.0255

approximate the char composition by replacing the three trace species by an equivalent amount of SiO₂*. The reason for these changes and their effects is discussed in the main body of the report.

A.2 MATERIAL THERMAL PROPERTIES MODEL

A thorough study of the available properties data on the Apollo heat shield material was carried out and a set of properties was selected which is believed to represent these data best. Char and virgin plastic thermal properties as functions of temperature are shown in Tables A-3 and A-4. The virgin plastic and char thermal conductivities were taken from recently prepared AVCO conductivity charts for pre-charred material (Ref. A-1). The data presented on the AVCO charts includes char thermal conductivity as a function of temperature with pre-char temperature as a parameter. The envelope of that data, in which the pre-char temperature is taken equal to the char temperature, was used for the present study. This choice is appropriate for constant heating arc-jet tests and prior to the first peak heating of a typical Apollo trajectory, but some error in char conductivity might be expected whenever heating rates are reduced sufficiently such that char temperatures drop substantially. Virgin plastic and char specific heat data are identical to the data used as of March, 1968 in the NASA-MSD STAB II code for 5026-39/HC-GP, as described in Reference A-2. Virgin and char emissivities were held constant at 0.65 consistent with the data of References A-3 and A-4.

A-3

TABLE A-3

CHAR THERMAL PROPERTIES

T °R	C _P Btu/lb°R	k Btu/ft sec°R	ε
460	0.35	1.33 x 10 ⁻⁶	0.65 ↑
710	0.35	1.94 x 10 ⁻⁶	
860	0.35	2.00 x 10 ⁻⁶	
1,060	0.35	1.86 x 10 ⁻⁶	
1,210	0.35	1.83 x 10 ⁻⁶	
1,360	0.37	1.94 x 10 ⁻⁶	
1,460	0.40	2.03 x 10 ⁻⁶	
1,710	0.45	2.89 x 10 ⁻⁶	
1,860	0.50	4.03 x 10 ⁻⁶	
2,060	0.50	6.81 x 10 ⁻⁶	
2,260	↑	1.00 x 10 ⁻⁴	
2,460		1.16 x 10 ⁻⁴	
2,660		1.38 x 10 ⁻⁴	
2,860		1.46 x 10 ⁻⁴	
3,060		1.61 x 10 ⁻⁴	
3,260		1.77 x 10 ⁻⁴	
3,460		1.93 x 10 ⁻⁴	
3,660		2.09 x 10 ⁻⁴	
3,860		2.18 x 10 ⁻⁴	
4,060		2.22 x 10 ⁻⁴	
4,260		2.20 x 10 ⁻⁴	
4,460		2.08 x 10 ⁻⁴	
4,660		1.95 x 10 ⁻⁴	
4,860		1.82 x 10 ⁻⁴	
5,060		8.48 x 10 ⁻⁵	
5,260		7.42 x 10 ⁻⁵	0.65 ↓
5,460		5.56 x 10 ⁻⁵	
5,660		4.03 x 10 ⁻⁵	
5,860		2.11 x 10 ⁻⁵	
6,060		1.53 x 10 ⁻⁵	
6,260		1.11 x 10 ⁻⁵	
6,460	0.50	6.95 x 10 ⁻⁶	0.65

The model for plastic decomposition which is used by the CMA program takes the form

$$\frac{\partial \rho}{\partial \theta} = B e^{-E_a/RT} \rho_o \left(\frac{\rho - \rho_r}{\rho_r} \right)^{\psi} \quad (A-1)$$

where ρ = instantaneous density
 ρ_r = residual or char density
 ρ_o = original or virgin density
 θ = time
 T = temperature

TABLE A-4
 VIRGIN PLASTIC THERMAL PROPERTIES

T °R	C _p Btu/lb°R	k Btu/ft sec°R	ε
460	0.350	1.33 x 10 ⁻⁵	0.65
560	0.350	1.61 x 10 ⁻⁵	0.65
660	0.356	1.93 x 10 ⁻⁵	0.65
760	0.360	1.97 x 10 ⁻⁵	0.65
860	0.370	2.00 x 10 ⁻⁵	0.65
960	0.420	1.94 x 10 ⁻⁵	0.65
1,060	0.440	1.86 x 10 ⁻⁵	0.65
1,160	0.440	1.83 x 10 ⁻⁵	0.65
1,260	0.440	1.83 x 10 ⁻⁵	0.65
1,360	0.440	1.89 x 10 ⁻⁵	0.65
1,460	0.440	2.03 x 10 ⁻⁵	0.65
5,000	0.440	2.03 x 10 ⁻⁵	0.65

For the material under consideration here, the following numerical values were used:

$$\begin{aligned}\rho_o &= 34.0 \text{ lb/ft}^3 \\ \rho_r &= 16.0 \text{ lb/ft}^3 \\ B &= 1.06 \times 10^6 \text{ sec}^{-1} \\ \psi &= 2.5 \\ E_a/R &= 24,530^\circ\text{R}\end{aligned}$$

Heats of formation of the virgin plastic, char, and pyrolysis gas for a datum of 536°R are

$$\begin{aligned}\Delta H_{f_{vp}} &= -2,390 \text{ Btu/lb} \\ \Delta H_{f_c} &= -3,310 \text{ Btu/lb} \\ \Delta H_{f_{pg}} &= 0\end{aligned}$$

The pyrolysis gas enthalpy is described in Table A-5. All enthalpies are computed by the relation

$$h = \Delta H_{f_{536^\circ\text{R}}} + \int_{536^\circ\text{R}}^T C_p dT \quad (\text{A-2})$$

A.3 COMPARISONS WITH TEST DATA

A.3.1 Theoretical Analysis Technique

Theoretical studies of in-depth thermal response of the Apollo material were carried out utilizing the "driver temperature" option of the Charring Material Ablation (CMA) program. The CMA code is an implicit finite-difference computational procedure for computing the one-dimensional transient transport of thermal energy in a three-dimensional isotropic material which can ablate from the front surface and can decompose in depth. A summary description of this program is contained in Part I of this series of reports.

TABLE A-5
PYROLYSIS GAS ENTHALPY

Temperature °R	Enthalpy Btu/lb
900.	-919.
1,500.	-410.
2,000.	0
2,500.	470.
3,000.	890.
3,600.	1,404.
4,500.	2,161.
5,400.	7,600.
6,300.	13,290.

A.3.2 Ground Test Data

Comparisons of in-depth temperature response utilizing the thermal properties model described above were made for twelve of the arc-jet test models of Schaefer (Ref. A-5). Assuming a constant recession rate throughout the test, the measured surface temperature (obtained with an infrared optical pyrometer) was used as the driver temperature. The results may be seen in Figures A-1 through A-12. In general, the predicted in-depth response is in reasonably good agreement with the measured values. Typically, agreement is better for cases where the surface temperature does not exceed 3,000°R, indicating that the thermal properties model in the high-temperature region may include some error. However, the measured surface temperature in the high-temperature tests is also less well defined.

A.3.3 Flight Test Data

Driver temperature calculations were also performed for data from a recent superorbital Apollo flight. The results of these calculations may be seen in Figures A-13 through A-15. In Figure A-13, the measured temperature history at 0.6 inch depth from the original surface was used to predict the temperature response at 0.9 inches. The resulting prediction is seen to be quite close to the actual temperature history, the maximum error being approximately 150°R. Figure A-14 shows the temperature comparisons using measurements at 0.3 inches as the driver, with predictions compared to thermocouple values at 0.6 and 0.9 inches. Agreement between measured and

predicted temperatures is excellent, with maximum error of 100°R and 150°R at 0.6 inches and 0.9 inches, respectively.

Predictions using the 0.1 inch thermocouple as a driver are not as straightforward or precise. The surface recedes past this thermocouple somewhere during the flight and the meaning of the thermocouple reading after burn-through is open to question. Nevertheless, an estimate of the surface recession history after burn-through was made and the measured response of the 0.1 inch thermocouple after burn-through was taken as the surface temperature. Predictions of in-depth temperature response are shown in Figure A-15. Agreement is not as good as for the other two cases, the in-depth temperature being overpredicted. This may be due in part to inaccurate properties in the higher temperature region (3,000 to 4,000°R); however, it is just as likely that the surface temperature after burn-through of the 0.1 inch thermocouple may not be as high as is recorded on that thermocouple.

A.3.4 Summary of Thermal Properties Model

The thermal properties model described in Section A.2 has been taken directly from data obtained for post-test chars. It is very satisfying, therefore, that the model appears to be very accurate for temperatures below about 3,000°R for both ground and flight test data. The comparison for test conditions where the surface (or reference thermocouple) exceeds 3,000°R is not as good, in-depth temperatures being consistently overpredicted. However, the agreement is judged satisfactory since the error may be due in no small part to uncertainties in the measured temperatures. Therefore, no attempt was made to modify the laboratory data to better match the present data at higher temperatures.

REFERENCES FOR APPENDIX A

- A-1. Ihnat, M. E.: Evaluation of the Thermophysical Properties of the Apollo Heat Shield. Report AVSSD-0375-67-RR, AVCO Space Systems Division, Wilmington, Massachusetts, August 8, 1967.
- A-2. Personal communication with Donald M. Curry, Contract Monitor.
- A-3. Pope, R. B.: Measurements of the Total Surface Emittance of Charring Ablators. AIAA J., 5, 2285, 1967.
- A-4. Wilson, R. G., and Spitzer, C. R.: Visible and Near-Infrared Emittance of Ablation Chars and Carbon. AIAA J., 6, 665, 1968.
- A-5. Schaefer, J. W., Flood, D. T., Reese, J. J. and Clark K. J.: Experimental and Analytical Evaluation of the Apollo Thermal Protection System Under Simulated Reentry Conditions. Report No. 67-16, Parts I and II, Aerotherm Corporation, Mountain View, California, July 1967.

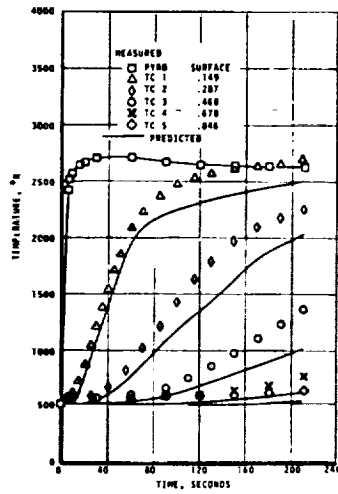


Figure A-1. Temperature Response for Model 93/BH/2.0

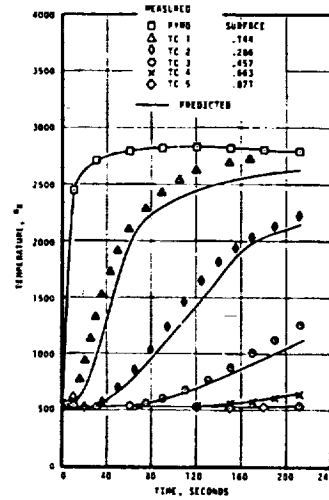


Figure A-2. Temperature Response for Model 114/BH/4.0

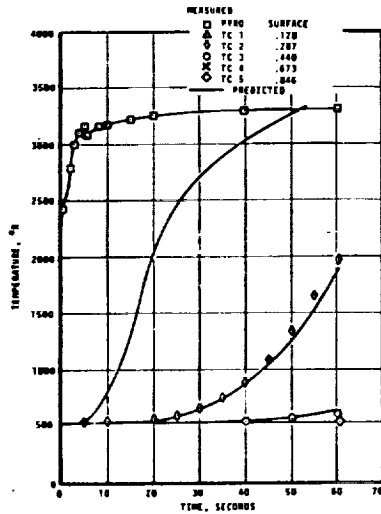


Figure A-3. Temperature Response for Model 91/BH/2.0

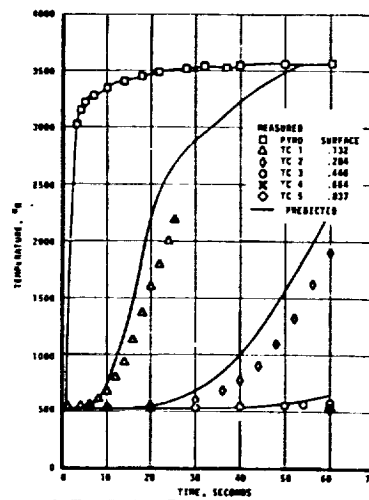


Figure A-4. Temperature Response for Model 103/BH/2.0

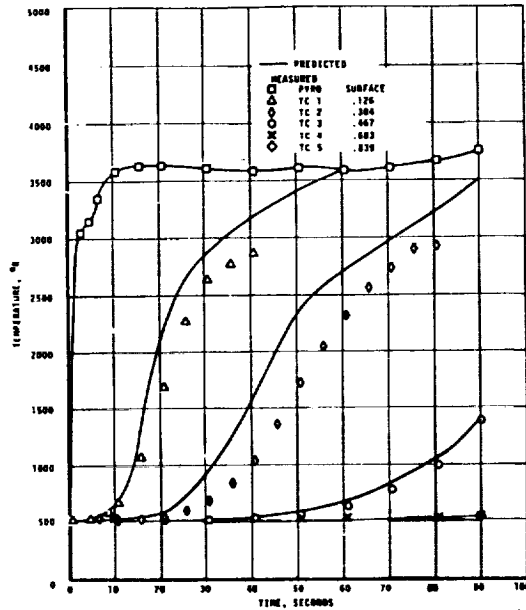


Figure A-5. Temperature Response for Model 30/BH/2.0

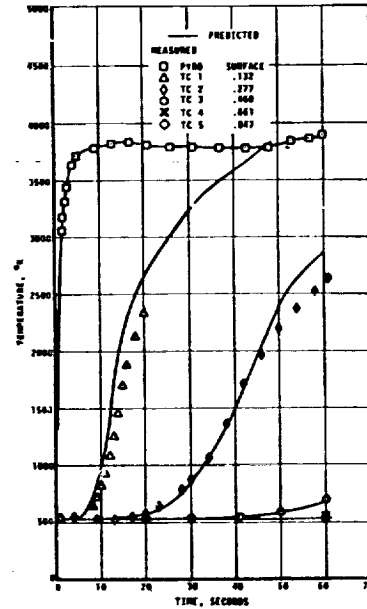


Figure A-6. Temperature Response for Model 122/BH/4.0

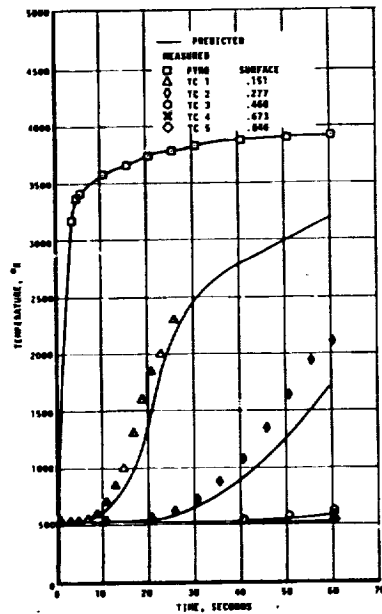


Figure A-7. Temperature Response for Model 84/BH/2.0

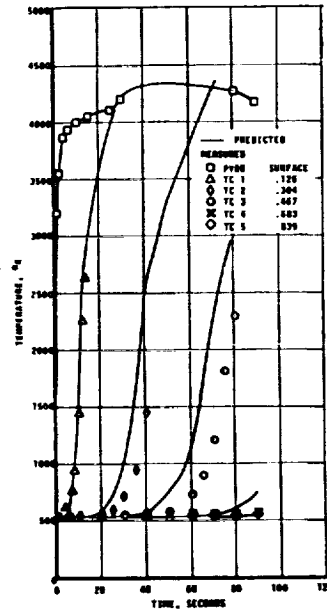


Figure A-8. Temperature Response for Model 27/BH/2.0

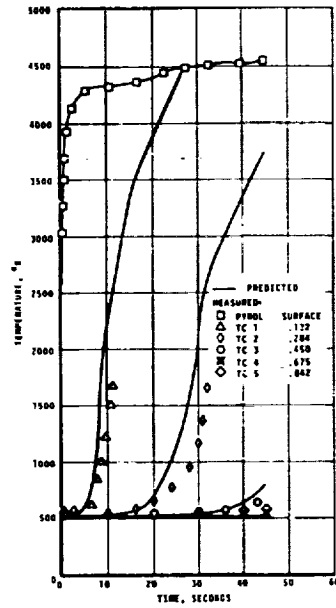


Figure A-9. Temperature Response for Model 102/BH/2.0

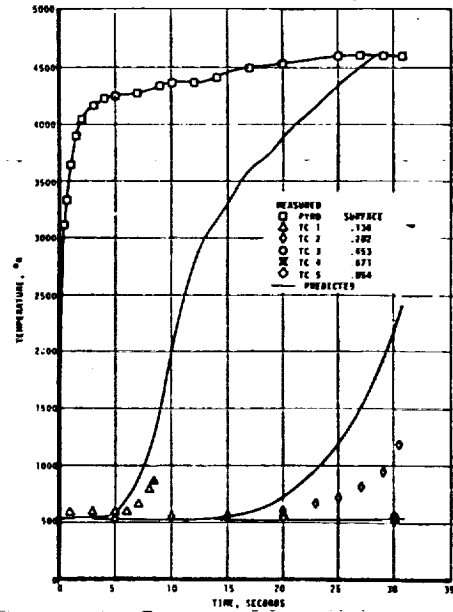


Figure A-10. Temperature Response for Model 96/BH/2.0

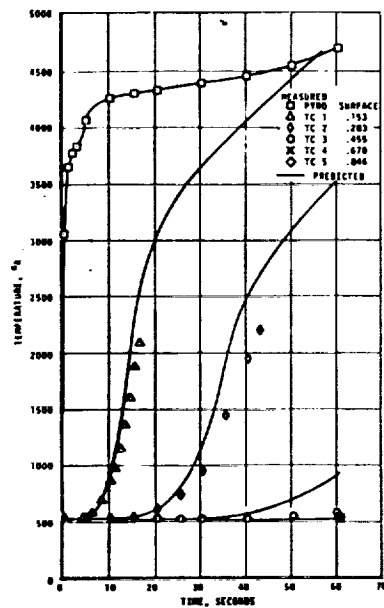


Figure A-11. Temperature Response for Model 80/BH/2.0

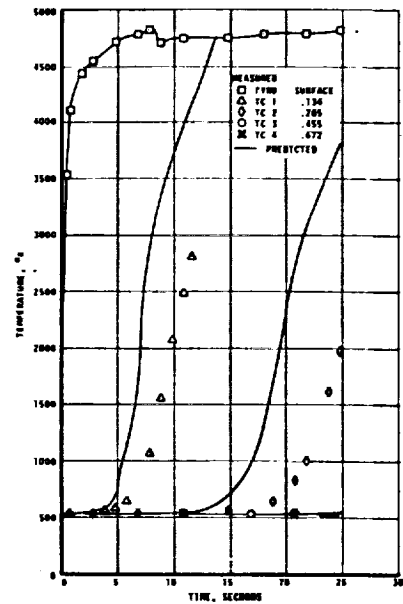


Figure A-12. Temperature Response for Model 111/BH/1.0

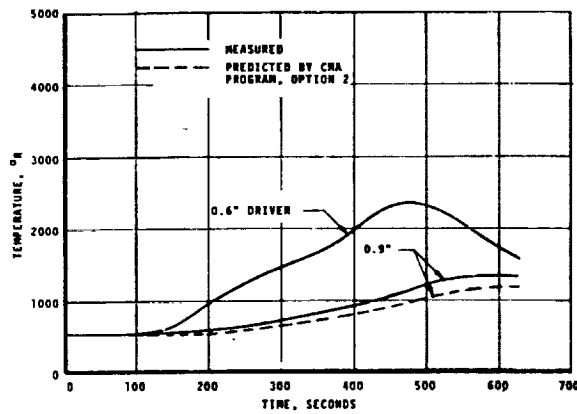


Figure A-13. Correlation of In-Depth Temperature Response of Apollo Flight Data Using 0.6 Inch Thermocouple as a Driver

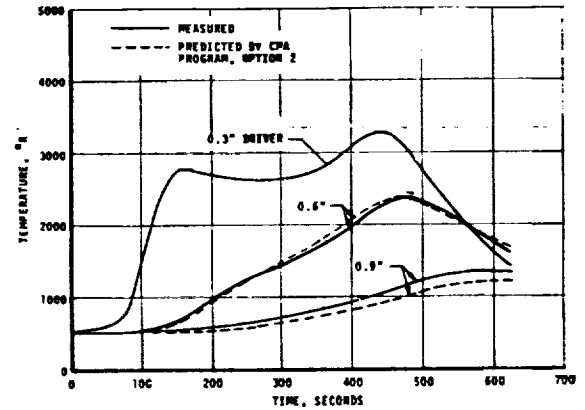


Figure A-14. Correlation of In-Depth Temperature Response of Apollo Flight Data Using 0.3 Inch Thermocouple as a Driver

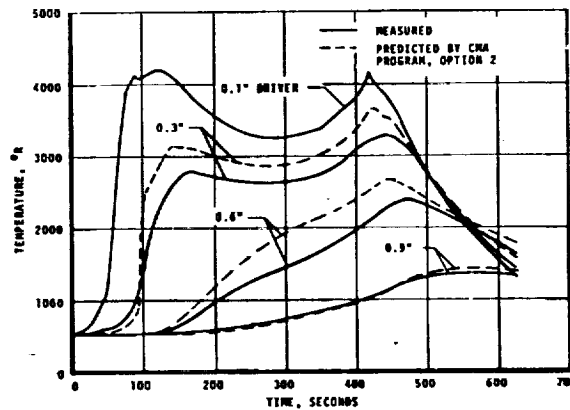


Figure A-15. Correlation of In-Depth Temperature Response of Apollo Flight Data Using 0.1 Inch Thermocouple as a Driver

APPENDIX B

**SUMMARY OF RECOMMENDED SURFACE
THERMOCHEMICAL ABLATION MODEL**

APPENDIX B

SUMMARY OF RECOMMENDED SURFACE THERMOCHEMICAL ABLATION MODEL

The prediction of transient ablation rates and transient temperature distributions requires a knowledge of material thermal properties and a surface thermochemical ablation model. Recommended material properties are presented in Appendix A. In this appendix the recommended surface thermochemical ablation model is summarized and the specific data needed to implement this model in the ACE and CMA programs are presented.

On the basis of the results presented in this report, it is recommended that the fissure model be employed for the prediction of Apollo heat shield ablation response. In this approach, the pyrolysis gas which forms is considered to pass through the boundary layer without attenuating the convective heating and without altering the composition of the boundary-layer gases at the wall. In addition, it is recommended that the rate law for mechanical removal of silica which was developed on the basis of ground test data be applied to the flight environment directly as $B'_c \sqrt{P}$.

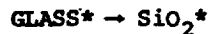
The appropriate elemental composition for the Apollo heat shield material is presented in Table B-1. This is for practical purposes the same as

TABLE B-1
CHAR AND PYROLYSIS GAS ELEMENTAL MASS FRACTIONS CONSIDERED IN FISSURE MODEL

Element	Pyrolysis Gas	Char	Atomic Weight
C	---	0.488	12.011
Si	---	0.0001	28.09
Glass	---	0.512	60.09
Pyrol	1.000	---	22.5

that given in Table II of the main body of the report but the following definitions are employed:

(1) The silica in the char, instead of being appropriated between SILICON and OXYGEN, is designated as a fictitious element GLASS. The purpose of this artifice is to permit the silica in the char to be converted to SiO_2^* through the reaction



(B-1)

(2) A trace of the conventional element SILICON is included in order that it will be catalogued into the solution as a potential element. The "element" SILICON is created through Reaction (B-1) and the SiO_2^* is furthermore required to be in equilibrium with other candidate species such as SiO , SiO_2 and Si_2 .

(3) The pyrolysis gas is designated to consist of a fictitious element PYROL of atomic weight 22.5. The purpose of this is to permit consideration of a frozen pyrolysis gas in the event the reader is interested in generating solutions for nonfissure, frozen pyrolysis gas models (B'_g is taken as zero in the fissure model so the pyrolysis gas elemental composition does not have to be defined in that case). The actual elemental composition of the pyrolysis gas in terms of HYDROGEN, OXYGEN, CARBON, and NITROGEN, which one would have to consider if pyrolysis gases were to be considered reactive, is shown in Table II of the main body of the report.

The species which are considered in the generation of the fissure thermochemical ablation model are presented in Part (a) of Table B-2, the frozen species PYROL is presented in Part (b), and the species which should be considered in a boundary layer with reactive pyrolysis gases are presented in Part (c). Curve fit constants used to generate specific heat, enthalpy and entropy for these species are also presented in Table B-2 together with instructions for interpreting these constants. The species GLASS* has identical properties to conventional SiO_2^* except that it is assigned a reduced entropy. (through the number P6 - see Table B-2) so that Reaction B-1 will be a one-way reaction. Also, SiO_2^* is assigned a low fail temperature of, say, 500°K . Finally, PYROL is composed of one atom of the element PYROL and is assigned a specific heat of $19.316 \text{ cal/mol } ^\circ\text{K}$, and a heat of formation of -15.4 Kcal/mol . The PYROL remains frozen in that there are no other chemical compounds considered involving PYROL.

The last pieces of information required are the kinetic constants for Reaction B-1. The rate law is expressed as

$$B'_c \sqrt{P} = B \exp(-E_a/RT_w) \quad (\text{B-2})$$

where $B = 4.24 \text{ atm}$ and $E_a/R = 19,000^\circ\text{K}$.

The fissure model ACE maps are generated considering $B'_g = 0$ for a range of pressure and B'_c . (If ACE maps are desired for nonfissure models, a range

of B'_g has to be considered, using PYROL if the pyrolysis gases are to be considered frozen or using the various hydrogen-containing species if the pyrolysis gases are to be considered reactive.)

Having generated fissure ACE maps, transient ablation predictions can be generated by using the thermal properties presented in Appendix A and the newly developed fissure option of CMA. In essence, in this option the surface energy balance equation is modified to reflect a pyrolysis gas rate, B'_g , of zero.

Two data changes are appropriate in order to make fissure model calculations. First, it is mandatory when generating ACE cards for CMA that $B'_g = 0$ data be included for any two values of B'_g (say, 0.01 and 0.02) so that the CMA program will be able to perform its linear interpolation (and extrapolation) in the ACE tables. The second change is optional and accomplishes the purpose of allowing the pyrolysis gas to pass directly out through the fissures in the material without absorbing energy from the char. In order to accomplish this, the pyrolysis gas enthalpy table (see Table A-5 of Appendix A) can be altered such that the gas specific heat is zero above, say, 2,700°R. This temperature is recommended as being representative of a 99-percent-char isotherm. The pyrolysis gas is thus allowed to absorb energy until the virgin material is nearly completely decomposed, whereupon the gas is injected instantly into the boundary layer without further energy absorption. The CMA program is not presently equipped to perform "post-peak" fissure calculations; however, this model can be treated approximately using the approach described in Part 4.3 of the main body of the report.

TABLE B-2

THERMODYNAMIC PROPERTIES OF GASEOUS AND CONDENSED SPECIES

DATA FORMAT

THE THERMODYNAMIC DATA ARE OBTAINED AS CURVE FITS OF BEST AVAILABLE DATA (TYPICALLY JANAF). THE CURVE FITS ARE GENERATED BY THE AEROTHERM TCDATA PROGRAM. THE DATA FORMAT IS THE SAME AS THAT USED IN NAVWEPS REPORT 7043 AND CONSISTS OF THREE CARDS FOR EACH SPECIES AS SHOWN BELOW.

CARDS 1, 4, 7, ONE FOR EACH MOLECULE $\text{FORMAT}(7(F3.0,13),30X,2A4)$

FIELDS 1, 3, 5, ONE FOR EACH ELEMENT IN MOLECULE (COLUMNS 1-3, 7-9, 13-15, ...)

NUMBER OF ATOMS (OF ATOMIC NUMBER GIVEN IN SUBSEQUENT FIELD) IN A MOLECULE OF THIS SPECIES.

FIELDS 2, 4, 6, ONE FOR EACH ELEMENT IN MOLECULE (COLUMNS 4-6, 10-12, 16-18, ...)

ATOMIC NUMBERS OF ELEMENTS IN MOLECULES.

LAST FIELD (COLUMNS 73-80)

MOLECULAR DESIGNATION (E.G., SiO_2) FOR OUTPUT AND AS IDENTIFIER FOR DIFFUSION FACTOR DATA.

CARDS 2, 5, 8, ONE FOR EACH MOLECULE $\text{FORMAT}(6E9.6,6X,F6.0,11)$

FIELD 1 (COLUMNS 1-9)

HEAT OF FORMATION OF MOLECULE AT 298 DEG K FROM JANAF BASE STATE (ELEMENTS IN MOST NATURAL FORM AT 298 DEG K), CAL/MOLE.

FIELDS 2-6 (COLUMNS 10-18, 19-27, 28-36, 37-45, AND 46-54)

CONSTANTS APPROPRIATE TO LOWER TEMPERATURE RANGE OF THERMODYNAMIC DATA. TAKING F_2 , F_3 , AS FIELDS 2, 3, ETC., THE CURVE FITS ARE AS FOLLOWS WITH T IN DEG K, H IN CAL/MOLE, AND S IN CAL/MOLE DEG K.

HEAT CAPACITY, $CP = F_3 F_4 + T F_5 / T^{**2}$

ENTHALPY, $H - H_{298} = F_2 F_3 * (T - 3000) + 60.5 * F_4 * (T^{**2} - 3000^{**2}) - F_5 * (1/T - 1/3000)$

ENTROPY, $S = F_6 F_3 * \text{LN}(T/3000) + F_4 * (T - 3000) - 0.5 * F_5 * (1/T^{**2} - 1/3000^{**2})$

FIELD 7 (COLUMNS 61-66)

UPPER LIMIT OF LOWER TEMPERATURE RANGE IN DEG K. FOR CONDENSED-PHASE MATERIALS WHICH MELT, THIS IS USUALLY TAKEN TO BE THE MELT TEMPERATURE).

FIELD 8 (COLUMN 67)

TABLE B-2 (CONTINUED)

1 SIGNIFIES GASEOUS SPECIES

2 SIGNIFIES SOLID SPECIES

3 SIGNIFIES LIQUID SPECIES

CARDS 3, 6, 9, ..., ONE FOR EACH MOLECULE FORMAT(6E9.6,6X,F6.0,11)

FIELDS 1-8 (COLUMNS 1-67)

SAME AS CARDS 2, 5, 8, ... EXCEPT USE CONSTANTS FOR UPPER TEMPERATURE RANGE AND FIELD 7 IS IGNORED.

LISTING OF SPECIES DATA

PART (A). CHAR AND BOUNDARY LAYER EDGE GASES ONLY (APPROPRIATE FOR USE WITH
FISSURE MODEL -- B PRIME G = 0)

1	6	0	0	0	0	0	0	0	0	OJANAF 03/61			C
17088666	13550065	44443361	228125-3	40983066	49287062	500.	3000.1			0.C			
17088666	13550065	41221261	261908-3	26288667	49287062	3000.	5000.1			0.C			
1	6	1	7	0	0	0	0	0	0	OJANAF 12/62			CN
10900066	23249065	65590661	115326-2	47951766	66976062	500.	3000.1			0.CN			
10900066	23249065	98801361	313855-3	64945367	66976062	3000.	5000.1			0.CN			
1	6	1	8	0	0	0	0	0	0	OJANAF 03/61			CO
-26417065	22357065	86504061	117021-3	89821166	65370062	500.	3000.1			0.CO			
-26417065	22357065	11549662	-424139-3	13156368	65370062	3000.	5000.1			0.CO			
1	6	2	8	0	0	0	0	0	0	OJANAF 03/61			CO2
-94054065	36535065	14455962	210386-3	18239267	79848062	500.	3000.1			0.CO2			
-94054065	36535065	15645162	-381561-4	60276867	79848062	3000.	5000.1			0.CO2			
2	6	0	0	0	0	0	0	0	0	OJANAF 9/61			C2
19899966	24699065	77661261	696081-3	18564966	68551962	500.	3000.1			0.C2			
19899966	24699065	10416262	566841-4	64020567	68551962	3000.	5000.1			0.C2			
2	6	2	7	0	0	0	0	0	0	OJANAF 3/61			C2N2
73869965	51107065	18874062	559856-3	89687366	98547962	500.	3000.1			0.C2N2			
73869965	51107065	20820462	630229-5	34686567	98547962	3000.	5000.1			0.C2N2			
3	6	0	0	0	0	0	0	0	0	OJANAF 12/60			C3
18967066	36622065	14644162	622536-4	16822767	79841062	500.	3000.1			0.C3			
18967066	36622065	14478262	792232-4	64687766	79841062	3000.	5000.1			0.C3			
3	6	2	8	0	0	0	0	0	0	OJANAF 12/60			C302
-83000064	65212065	26377562	103904-3	35036867	11272363	500.	3000.1			0.C302			
-83000064	65212065	26354362	882201-4	28709167	11272363	3000.	5000.1			0.C302			
4	6	0	0	0	0	0	0	0	0	OJANAF 12/60			C4
24232166	51123065	20590362	623436-4	25770367	98676062	500.	3000.1			0.C4			
24232166	51123065	21071462	-434895-4	40493967	98676062	3000.	5000.1			0.C4			
4	6	2	7	0	0	0	0	0	0	OJANAF 3/61			C4N2
12750066	80123965	29749062	856052-3	15225567	13306363	500.	3000.1			0.C4N2			
12750066	80123965	32721262	952999-5	54165467	13306363	3000.	5000.1			0.C4N2			
5	6	0	0	0	0	0	0	0	0	OJANAF 12/60			C5
24237466	65623065	26470662	806528-4	33712567	11164163	500.	3000.1			0.C5			
24237466	65623065	27115662	-580271-4	54318367	11164163	3000.	5000.1			0.C5			

TABLE B-2 (CONTINUED)

6 6 0 0 0 0 0 0 0 0 0 0 0 0 0 0	ODUFF BAUER 6/61		C6
29134266 77270065 30396562 607305-3-47566067 12895863	500. 3000.1	0.C6	
29134266 77270065 30848862 643430-4 58335067 12895863	3000. 5000.1	0.C6	
7 6 0 0 0 0 0 0 0 0 0 0 0 0 0 0	ODUFF BAUER 6/61		C7
29211666 90977065 35979562 669838-3-57963867 14055563	500. 3000.1	0.C7	
29211666 90977065 35578562 210202-3 10222268 14055563	3000. 5000.1	0.C7	
8 6 0 0 0 0 0 0 0 0 0 0 0 0 0 0	ODUFF BAUER 6/61		C8
34489166 10468466 41559462 733634-3-68346267 15927563	500. 3000.1	0.C8	
34489166 10468466 40289462 359448-3 14698468 15927563	3000. 5000.1	0.C8	
9 6 0 0 0 0 0 0 0 0 0 0 0 0 0 0	ODUFF BAUER 6/61		C9
34066566 11839166 47141062 796582-3-78732867 17087263	500. 3000.1	0.C9	
34066566 11839166 45020762 505033-3 19081368 17087263	3000. 5000.1	0.C9	
10 6 0 0 0 0 0 0 0 0 0 0 0 0 0 0	ODUFF BAUER 6/61		C10
40043966 13209866 52720262 860613-3-89107667 18959263	500. 3000.1	0.C10	
40043966 13209866 49743962 651908-3 23510968 18959263	3000. 5000.1	0.C10	
1 7 0 0 0 0 0 0 0 0 0 0 0 0 0 0	OJANAF 03/61		N
11296566 13437065 48694461 383516-4 95846065 48090062	500. 3000.1	0.N	
11296566 13437065 42895761 240844-3-41727366 48090062	3000. 5000.1	0.N	
1 7 1 8 0 0 0 0 0 0 0 0 0 0 0 0	OJANAF 06/63		NO
21580065 22700065 87762361 899031-4-78965666 68849062	500. 3000.1	0.NO	
21580065 22700065 91626061 657885-5-21251967 68849062	3000. 5000.1	0.NO	
1 7 2 8 0 0 0 0 0 0 0 0 0 0 0 0	OJANAF 06/63		NO2
80110064 34580065 13781962 315611-4-13376567 84889062	500. 3000.1	0.NO2	
80110064 34580065 13015462 172586-3 17534067 84889062	3000. 5000.1	0.NO2	
1 7 3 8 0 0 0 0 0 0 0 0 0 0 0 0	OJANAF 12/64		NO3
17000065 49821965 19230162 191161-3-11212967 99897062	500. 3000.1	0.NO3	
17000065 49821965 19870962 577142-7-17291367 99897062	3000. 5000.1	0.NO3	
1 7 1 14 0 0 0 0 0 0 0 0 0 0 0 0	OJANAF 12/60		NS1
12100066 23511065 89335761 603803-4-41146666 71156062	500. 3000.1	0.NS1	
12100066 23511065 88377961 815057-4-11976966 71156062	3000. 5000.1	0.NS1	
2 7 0 0 0 0 0 0 0 0 0 0 0 0 0 0	OJANAF 03/61		N2
000000-0 22165065 86269961 116090-3-10371567 63765062	500. 3000.1	0.N2	
000000-0 22165065 98417561-116232-3-61272867 63765062	3000. 5000.1	0.N2	
2 7 1 8 0 0 0 0 0 0 0 0 0 0 0 0	OJANAF 12/60		N20
19500065 36545065 14468662 120489-3-15347867 81590062	500. 3000.1	0.N20	
19500065 36545065 12303662 459018-3 94238267 81590062	3000. 5000.1	0.N20	
2 7 3 8 0 0 0 0 0 0 0 0 0 0 0 0	OJANAF 12/64		N203
19799965 61779965 23212162 477580-3-12410367 12321763	500. 3000.1	0.N203	
19799965 61779965 24830462 102872-5-29389267 12321763	3000. 5000.1	0.N203	
2 7 4 8 0 0 0 0 0 0 0 0 0 0 0 0	OJANAF 9/64		N204
21699964 78596965 29773462 594431-3-17883367 13490863	500. 3000.1	0.N204	
21699964 78596965 31781562 175630-5-38596967 13490863	3000. 5000.1	0.N204	
2 7 5 8 0 0 0 0 0 0 0 0 0 0 0 0	OJANAF 12/64		N205
21699964 91575965 35305162 147295-3-16385067 15671963	500. 3000.1	0.N205	
21699964 91575965 35736562 624545-5-17126767 15671963	3000. 5000.1	0.N205	
1 8 0 0 0 0 0 0 0 0 0 0 0 0 0 0	OJANAF 06/62		O
59559065 13522065 49722861 380768-5 15474965 50096062	500. 3000.1	0.O	
59559065 13522065 65748961-224268-3-89178267 50096062	3000. 5000.1	0.O	
1 8 1 14 0 0 0 0 0 0 0 0 0 0 0 0	OJANAF 09/63		OS1
-24200065 23359065 89144461 545951-4-45209166 69747062	500. 3000.1	0.OS1	
-24200065 23359065 35077361 132710-3 10991867 69747062	3000. 5000.1	0.OS1	
2 8 0 0 0 0 0 0 0 0 0 0 0 0 0 0	OJANAF 03/61		O2
000000-0 23446065 80437061 510872-3-15271866 67973062	500. 3000.1	0.O2	
000000-0 23446065 10307162 290991-4-78307967 67973062	3000. 5000.1	0.O2	
2 8 1 14 0 0 0 0 0 0 0 0 0 0 0 0	OJANAF 12/62		O2S1
-76200065 38295065 14827262 207464-4-77720066 85895062	500. 3000.1	0.O2S1	
-76200065 38295065 13332062 289052-3 57113967 85895062	3000. 5000.1	0.O2S1	

TABLE B-2 (CONTINUED)

[illegible]

TABLE B-2 (CONTINUED)

[illegible]

1
2

1
2
3
4
5
6
7
8
9
10
11
12

1

APPENDIX C
SUMMARY OF GROUND TEST DATA
UTILIZED IN THIS STUDY

APPENDIX C
SUMMARY OF GROUND TEST DATA
UTILIZED IN THIS STUDY

The ground test data considered in the present study were generated in the Aerotherm Arc tunnel facility under a previous effort (Ref. C-1). Approximately 150 tests of the Apollo heat shield material were conducted under carefully controlled conditions simulating a broad spectrum of lunar return conditions. In order to assure valid results, the flow stream was thoroughly calibrated for all test conditions. Pressure and heat flux variations across the models were measured to check the uniformity of the environment. Measurements were also made to verify proper gas mixing and acceptable contamination levels. In view of the relatively high permeability of the Apollo heat shield material, special precautions were taken to seal the model cores to prevent gas leakage. The effect of porous flow on the results was investigated analytically and is reported in Appendix D to be negligible, at least for the tests conducted at 1 atmosphere and below.

Observation of the models during the tests combined with post-test chemical analysis of the models indicated that there are basically four regimes of surface behavior in terms of surface temperature and pressure:

1. At the lowest surface temperatures (to 1,600°K) a surface scab of agglomerated silica fibers appears on the surface.
2. At intermediate surface temperatures (1,600 to 2,100°K) silica globules partially cover the char surface, the coverage decreasing as wall temperature increases.
3. At higher temperatures (above 2,100°K) there is no evidence of a silica melt. Although no direct measurements of char density were made, post-test chemical analysis showed a substantial decrease in the silica-to-carbon ratio near the surface indicating either carbon deposit or silica depletion near the surface. Also, SiC* crystals often showed up in the chemical analysis, but never as more than two percent of the surface material.
4. At test conditions above one atmosphere pressure, gross mechanical removal was observed.

Other significant findings in the experimental program were that surface recession rate is independent of run time and that substantial erosion occurs

in nitrogen (approximately one-third that which occurs in air) but that only slight erosion occurs in helium under similar test conditions.

Pertinent data and test conditions for the tests considered in the main text of this report are shown in Table C-1. All of the convective heating tests of the Apollo heat shield material in air were considered with the exception of turbulent duct tests and tests at pressures greater than 1.0 atmosphere. The reported surface recession rate is an average for the total test time, while the T_w represents an average value near the end of the test where steady-state ablation was being approached. The use of an average \dot{S} seems reasonable in view of the fact that the theoretical ablation models under consideration all predict a rapid rise of \dot{S} to the asymptotic value and the test results appear to be insensitive to test duration.

For the purpose of comparing to the normalized ablation maps, the \dot{m}_c were computed considering the char density appropriate to the particular theoretical model in question. The $\rho_e u_e C_M$ were calculated for each test by correcting the reported value for hot-wall nonablating heat transfer coefficient, $\rho_e u_e C_{H_0}$, for mass addition. The blowing corrections associated with B'_c were obtained iteratively, while the blowing corrections for B'_g were calculated from average values of B'_g obtained by interpolating between limiting theoretical predictions for the tests. Considering experimental uncertainties, the averaging procedures employed, and the importance of the approximate blowing corrections employed, the experimental B'_c are believed to be within about ± 20 percent and the T_w (which are taken directly from the experiments) to be within 200°K or so.

REFERENCE FOR APPENDIX C

- C-1. Schaefer, J. W., Flood, D. T., Reese, J. J., Jr., and Clark, K. J.: Experimental and Analytical Evaluation of the Apollo Thermal Protection System Under Simulated Reentry Conditions. Report No. 67-16, Parts I and II, Aerotherm Corporation, Mountain View, California, July 15, 1967.

TABLE C-1
SUMMARY OF DATA USED IN PRESENT STUDY

Model No.**	Enthalpy Btu/lb	Pressure Atm	$\rho_e u_e C_{H_0}$ Lb/sec ft ²	\dot{S}_{avg} Mils/sec	$T_{w avg}$ °R	Surface Condition*
90/BH/2.0	10969	.0079	.0098	2.54	3200	M
91/BH/2.0	10969	.0079	.0098	2.51	3250	M
92/BH/2.0	10193	.0079	.0112	2.49	3350	M
99/BH/2.0	16301	.0080	.0088	2.57	3475	M
108/BH/2.0	16301	.0080	.0088	2.44	3550	M
126/BH/4.0	14480	.0081	.0062	1.40	3200	M
127/BH/4.0	14480	.0081	.0062	1.37	3250	M
128/BH/4.0	13500	.0081	.0063	1.52	3250	M
93/BH/2.0	3442	.0082	.0090	0.48	2650	S
94/BH/2.0	3539	.0082	.0090	0.81	2700	S
95/BH/2.0	3539	.0082	.0090	0.63	2675	S
106/BH/2.0	16880	.0082	.0089	2.40	3500	M
109/BH/2.0	25600	.0085	.0090	2.50	3825	NM
162/BH/2.0	25800	.0085	.0090	2.53	3850	NM
166/BH/2.0	29400	.0085	.0090	2.63	3900	NM
89/BH/2.0	4944	.0090	.0091	0.54	2900	S
116/BH/4.0	4944	.0090	.0064	0.58	2800	S
88/BH/2.0	5044	.0110	.0085	0.64	2850	S
115/BH/4.0	5044	.0110	.0059	0.51	2800	S
87/BH/2.0	4910	.0112	.0090	0.90	2875	S
114/BH/4.0	4910	.0112	.0063	0.40	2825	S
74/BH/2.0	6322	.0261	.019	2.64	3525	M
22/FF/2.0	7236	.0265	.012	2.28	3650	M
26/BH/2.0	5549	.0289	.016	2.84	3700	M
19/BH/2.0	5582	.0270	.011	1.54	3600	M
25/BH/2.0	5447	.0270	.021	2.46	3575	M
33/BH/2.0	5640	.0275	.026	3.81	3750	M
30/BH/2.0	5937	.0275	.018	2.42	3600	M
122/BH/4.0	10434	.0275	.0119	2.77	3800	NM
119/BH/4.0	10976	.0279	.0099	3.12	4000	NM
117/BH/4.0	4612	.0279	.0114	0.86	3200	S, M

TABLE C-1 (concluded)

Model No.**	Enthalpy Btu/lb	Pressure Atm	$\rho_e u_e C_{H_2O}$ Lb/sec ft ²	\dot{S}_{avg} Mils/sec	$T_{w,avg}$ °R	Surface Condition*
124/BH/4.0	19040	.0279	.0116	2.25	3775	NM
125/BH/4.0	15891	.0279	.0116	1.88	3825	NM
159/BH/2.0	17204	.0279	.022	5.13	4475	NM
35/BH/2.0	10463	.0281	.021	5.54	4300	NM
123/BH/4.0	15186	.0283	.0117	2.12	3800	NM
75/BH/2.0	11578	.0283	.016	4.97	4050	NM
29/BH/2.0	9554	.0283	.015	3.78	4175	NM
165/BH/2.0	17300	.0283	.017	3.90	4150	NM
100/BH/2.0	15800	.0295	.017	4.84	4500	NM
164/BH/2.0	15800	.0285	.017	3.48	4500	NM
101/BH/2.0	17400	.0287	.017	4.76	4525	NM
20/BH/2.0	14844	.0287	.012	2.73	4400	NM
21/BH/2.0	14267	.0287	.012	3.22	4400	NM
34/H/2.0	3692	.0289	.031	2.68	3500	M
37/FF/1.25	5020	.071	.019	1.00	3800	M
49/FF/1.25	6290	.099	.032	4.07	4100	NM
46/FF/1.25	3090	.112	.051	3.48	3775	M
51/FF/1.25	3290	.112	.043	3.71	3625	M
134/BH/1.0	3310	1.01	.238	61.0	4600	NM
156/BH/1.0	3456	1.02	.219	≈33.2	4800	NM
113/BH/1.0	5047	1.05	.222	47.0	4960	NM
154/BH/1.0	5031	1.06	.217	38.5	4600	NM

* S = Surface Scab, M = Melt Globules, NM = No Melt

** BH = Blunt Hemisphere, FF = Flat Faced, H = Hemisphere
Last number in Model No. is body diameter in inches.

APPENDIX D

AN EVALUATION OF THE EFFECTS OF POROUS FLOW
THROUGH THE SCHAEFER TEST MODELS

by

Jack D. Melnick

APPENDIX D

AN EVALUATION OF THE EFFECTS OF POROUS FLOW THROUGH THE SCHAEFER TEST MODELS

D.1 INTRODUCTION

The purpose of this study is to determine the effects of porous flow through a model of the Apollo heat shield material tested in Reference D-1. The approach utilized follows closely the approach used in Reference D-2 in a study of porous flow through graphite nose tips. In essence, it is desired to compare the mass flow rate due to thermochemical ablation with the mass flow rate of air within the model due to the porosity of the material. If the latter is negligible with respect to the former, the effect of porosity may be neglected.

The effects of substantial porous flow may be summarized as follows:

1. Suction into the porous surface would tend to decrease the boundary layer thickness and hence increase the convective heat transfer coefficient.
2. Energy transfer between the internal gas flow and the model as a consequence of a temperature differential could alter the model's temperature field.
3. In-depth chemical reactions could occur.

D.2 THEORETICAL APPROACH

There are two models which are commonly used for non-rarefied porous flow calculations; namely, Darcy's Law and Reynold's Law, which reduces to Darcy's Law when viscous forces dominate inertial forces (low Reynold's number). Unfortunately, since the flow velocity is an unknown, it is not a priori obvious when to neglect inertial effects. But, if it is initially assumed that inertial effects are negligible, then this assumption may be subsequently tested using the computed results. This approach has been utilized here.

For Darcy's Law

$$\dot{m} = \rho \vec{v} = -\rho \frac{K}{\mu} \text{ grad } P \quad (D-1)$$

where

\dot{m} = mass flow rate based on projected area (lbm/ft² sec)

K = permeability coefficient (ft²)

μ = viscosity of the gas (lbf sec/ft²)

\vec{v} = gas velocity of projected fluid (ft/sec)

P = gas pressure (lbf/ft²)

ρ = gas density (lbm/ft³)

Reynold's Law can be stated as

$$|\text{grad } P| = \alpha \mu v + \beta \rho v^2 \quad (\text{D-2})$$

where

α = viscous resistance coefficient (ft⁻²)

β = inertial resistance coefficient (ft⁻¹)

The Aerotherm Axisymmetric Transient Temperature (AATT) code can be used to solve for the mass flow through a porous medium if one assumes that Darcy's Law holds since Fourier's Law and Darcy's Law are of the same form.

Fourier's Law is given by

$$\dot{q} = -k \text{ grad } T \quad (\text{D-3})$$

where \dot{q} is the conductive heat flux in Btu/ft²sec and k is the conductivity in Btu/ft-sec °R. Thus, one can make the following transformation

$$T(^{\circ}\text{R}) \rightarrow P \quad (\text{lbf/ft}^2)$$

$$k(\text{Btu/ft-sec}^{\circ}\text{R}) \rightarrow \frac{K\rho}{\mu} \quad \frac{\text{lbm} - \text{ft}}{\text{lbf} - \text{sec}}$$

$$\dot{q}(\text{Btu/ft-sec}^{\circ}\text{R}) \rightarrow \dot{m} \quad (\text{lbm/ft}^2\text{sec})$$

The dimensions of length and time remain unchanged in this analogy.

The equation for conservation of mass for unsteady compressible flow through a solid of porosity, ϵ (volume of empty space divided by total solid volume) is

$$\text{div}(\rho \vec{v}) = -\epsilon \frac{\partial \rho}{\partial \theta} \quad (\text{D-4})$$

For unsteady heat conduction, conservation of energy is analogously

$$\text{div} \vec{q} = -\rho_s c_p \frac{\partial T}{\partial \theta} \quad (\text{D-5})$$

where ρ_s is the density of the solid (lbm/ft³) and c_p is the specific heat of the solid (Btu/lbm^oR). Combining the rate equations with the conservation equations gives

$$\text{div} \left[\frac{\rho K}{\mu} \text{grad } p \right] = \epsilon \frac{\partial \rho}{\partial \theta} \quad (\text{D-6})$$

$$\text{div}(k \text{ grad } T) = \rho_s c_p \frac{\partial \rho}{\partial \theta} \quad (\text{D-7})$$

If the flow follows the perfect gas law

$$\rho = \frac{p}{RT} \quad (\text{D-8})$$

and

$$\text{div} \left[\frac{Kp}{\mu RT} \text{grad } p \right] = \frac{\epsilon}{RT} \frac{\partial p}{\partial \theta} - \frac{\epsilon p}{RT^2} \frac{\partial T}{\partial \theta} \quad (\text{D-9})$$

Pressure and temperature are both unknown. If a unique relationship is assumed between them, then the partial differential equation governing porous flow may be written as a function of one unknown dependent variable, p . The simplest approach is to consider the flow isothermal. However, comparison of the p and T boundary conditions indicated that some improvement in accuracy might be realized by the use of a polytropic relation

$$T = C\sqrt{p} \quad (\text{D-10})$$

where C is a constant for a given situation chosen to best match the temperature and pressure boundary conditions.

With the substitution of Equation (D-10) into Equation (D-9), there results

$$\text{div} \left[\frac{K\sqrt{p}}{CR_u} \text{grad } p \right] = \frac{\epsilon}{2CR\sqrt{p}} \frac{\partial p}{\partial \theta} \quad (\text{D-11})$$

One can then use the AATT code with $\rho_s c_p$ replaced by $\epsilon/(2CR\sqrt{p})$ together with the other transformations outlined above.

The quantity $\epsilon/(2CR\sqrt{p})$ can be seen as simply a measure of the time to reach steady state for the system. The final distribution of \dot{m} and p will not be affected by the value of this quantity. Therefore a nominal value of $\epsilon = 0.1$ was selected for the problem.

The variation of viscosity with temperature was taken to be

$$\mu = \mu_1 \left[\frac{T}{T_1} \right]^{0.764} \quad (\text{D-12})$$

which can be expressed as a function of p through the polytropic temperature-pressure relation.

The boundary conditions for this code are surface pressure (temperature in the case of heat conduction) or mass flux (heat flux) as functions of time. These were taken to be time-independent over the test duration. A Newtonian pressure distribution was assumed on the front face of the model, ambient pressure was considered on the side walls, and the back wall was considered to be impervious* to flow (insulated). The initial pressure was taken to be the ambient value.

D.3 TEST MODEL CONSIDERED AND PERMEABILITY DATA EMPLOYED

The model and conditions of test 30/BH/2.0 was selected for this calculation (Ref. D-1). Test 30/BH/2.0 employed a two-inch diameter cylinder of axial length one inch. The front face was a section of a sphere two inches in radius. The local stagnation pressure in this test was 0.0275 atm (or 58.10 lbf/ft²).

*This key boundary condition is believed justified because of the type of seal employed.

The model was assumed to be composed only of virgin material (i.e., no char) for this preliminary calculation. The effect of the char layer with its higher permeability is discussed later. The permeability in the direction parallel to the honeycomb walls was taken directly from data published in Ref. D-3. In this reference, an initial curve-fit gave a negative value of β which is physically impossible. A second curve-fit was then made in Ref. D-3 using $\beta = 0$. Thus, the value of α reported therein is the reciprocal of permeability and $K_{||}$ is

$$K_{||} = 1.40 \times 10^{-11} \text{ ft}^2$$

Original test data on pressure drop through plugs of the Apollo material reported in Ref. D-4 were evaluated using Darcy's Law to determine K_{\perp} . For a plug of thickness L , through which the pressure drops slightly from p_2 to p_1 , Darcy's Law can be approximated by

$$\frac{p_1 - p_2}{L} = \frac{\mu V}{K_{\perp}} \quad (D-13)$$

The resulting mean of three calculations of K_{\perp} was

$$K_{\perp} = 2.095 \times 10^{-13} \text{ ft}^2$$

where the three values of K_{\perp} are within 3 percent of the mean. (This shows that Darcy's Law is valid for these test conditions.)

It is felt that the use of average values for $K_{||}$ and K_{\perp} is adequate since gross effects are being studied, and it is not necessary to attempt to approximate the actual complicated honeycomb structure for this calculation.

The boundary conditions are

$$p = p_{\infty} + (p_0 - p_{\infty}) \cos^2 \phi \quad (D-14)$$

on the hemispherical cap where ϕ is the angle from the horizontal to the normal at the point. On the cylinder wall,

$$p = p_{\infty} \quad (D-15)$$

D-6

On the back wall,

$$\frac{\partial p}{\partial n} = 0 \quad (D-16)$$

For the test under consideration

$$p_o = 58.10 \text{ lbf/ft}^2$$

$$p_\infty = 2.78 \text{ lbf/ft}^2$$

D.4 RESULTS AND CONCLUSIONS

The results of the calculations are shown on the grid network which was utilized (Figure D-1). The \dot{m} 's that are shown are the mass rates of flow due to porosity at the surface nodes. The numbers shown within the grids are the local values of pressure. This result, of course, is completely decoupled in this calculation from thermochemical ablation.

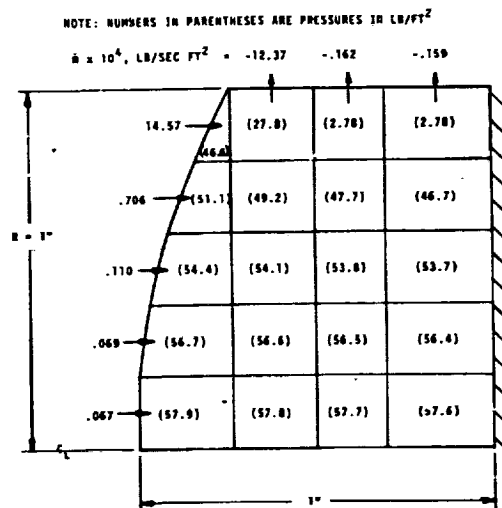


Figure D-1. Internal Pressure Distribution and Flow Rates In and Out of a 5026-39/HC-GP Test Sample (Test 30/BH/2.0, $p_\infty = 2.78 \text{ lb/ft}^2$, $p_o = 58.1 \text{ lb/ft}^2$)

The results show that \dot{m} varies from $6.723 \times 10^{-6} \text{ lbm/ft-sec}$ at the stagnation point up to a maximum of 1.457×10^{-3} at the corner. This can be compared to an average \dot{m} of 7×10^{-3} measured during the test (Ref. D-1). The

high values of \dot{m} occur only at the corner where the path length is small. Porous flow through the virgin material in the vicinity of the stagnation point would therefore not seem to be important. The models tested in Ref. D-1 did not have pressure equalization holes nor was the effect of such holes considered in the calculations. However, this should not have an effect on this conclusion because of the small size and small number of the holes.

The use of Darcy's Law was checked with the set of α and β first calculated in fitting the Ref. D-3 test data. Despite the negative β value, the data was thought to give a good measure of the relative size of α and β . Substituting an average value of $\dot{m} = 7 \times 10^{-8}$ and $\mu = 1.77 \times 10^{-6}$ lbm/ft-sec

$$\left| \frac{\beta Re}{\alpha} \right| = \frac{(7.47 \times 10^3)(7 \times 10^{-8})}{(6.63 \times 10^{10})(1.77 \times 10^{-6})} = 4.5 \times 10^{-8}$$

Thus for this condition the neglect of inertial effects was indeed justified.

In order to develop further confidence in the overall mass-flow-rate results obtained in the two-dimensional calculations, solutions were also generated using a one-dimensional, isothermal approximation for the pressure drop

$$\dot{m} = \frac{p_o^2 - p_w^2}{2\mu \alpha R T L} \quad (D-17)$$

If one assumes that $L = 1$ inch and $T = 600^\circ R$

$$\dot{m} = 2.37 \times 10^{-6} \text{ lbm/ft}^2\text{-sec}$$

which agrees quite favorably with the computed values of \dot{m} for the test conditions.

Consideration of $\alpha = 5.78 \times 10^9$ for the char (given in Ref. D-3) gives for isothermal conditions (say, $T = 2,000^\circ R$) the surprisingly low mass flux

$$\dot{m} = 3.54 \times 10^{-6} \text{ lbm/ft}^2\text{-sec}$$

One can thus conclude that porous flow in the char layer may also be neglected in the tests of Ref. D-1 at this pressure level. The situation is different at higher pressures. If $p_o = 1$ atmosphere

$$\dot{m} = 4.5 \times 10^{-2} \text{ lbm/ft}^2\text{-sec}$$

and \dot{m} due to ablation is the order of 10×10^{-2} . This shows that porous flow could well be a factor in eroding chars in tests conducted at high stagnation pressures.

It should be noted that after the calculations were made, use of a polytropic relation between T and p was found to be probably not as good as a simple isothermal assumption. In particular, the pressure drop within the porous solid occurs near the side boundary, whereas the primary temperature drop occurs near the front face and secondly, the temperature is fairly uniform throughout the majority of the body. However, this effect is believed not to affect the major conclusions of the study. Finally, the quasi-steady assumption is good, since the time found to reach steady pressure and \dot{m} values is a few seconds, while the test duration was 89 seconds.

REFERENCES FOR APPENDIX D

- D-1. Schaefer, J. W., Flood, D. T., Reese, J. J., Jr., and Clark, K. J.: Experimental and Analytical Evaluation of the Apollo Thermal Protection System Under Simulated Reentry Conditions. Report No. 67-16, Parts I and II. Aerotherm Corporation, Mountain View, California, July 15, 1967.
- D-2. Powars, C. A., Rindal, R. A., and Rodriguez, D. A.: A Detailed Thermal and Structural Analysis of Graphite Nosetip Models Tested in Arc-Heated Air. Final Report, Aerotherm Corporation, Mountain View, California, Sandia Laboratories Contractor Report (to be published).
- D-3. Munson, T. R., et al.: An Advanced Analytical Program for Charring Ablators. AVCO Report AV SSD-0172-67-RR, Vol. I, AVCO Space Systems Division, Wilmington, Massachusetts, (no date).
- D-4. Anonymous: Evaluation of the Thermal Properties of Materials. AVCO Report AV SSD-0197-66-RR, AVCO Space Systems Division, Wilmington, Massachusetts, June 1966.

APPENDIX E

AN ATTEMPT TO PREDICT SURFACE RECESSION FOR THE
APOLLO HEAT SHIELD MATERIAL ON THE BASIS
OF SILICA-CARBON REACTION KINETICS ALONE

by

Carl B. Moyer

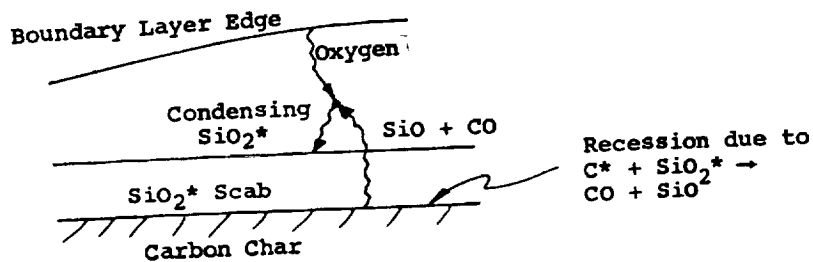
APPENDIX E

AN ATTEMPT TO PREDICT SURFACE RECESSON FOR THE APOLLO HEAT SHIELD MATERIAL ON THE BASIS OF SILICA-CARBON REACTION KINETICS ALONE

E.1 MODEL

A number of the post-test specimens described in Reference E-1 had a crusty siliceous "scab" resting on top of the carbonaceous char. Both the top surface of the scab and the scab-char interface receded during the tests at approximately the same velocity after the initial transient, although there is some evidence that the scab was slowly thickening during all of the tests.

Since it is well known that condensed phase carbon and silica react to form gaseous products, one might speculate whether the velocity of the scab-char interface could be interpreted as being due to erosion of the carbon substrate by the hot silica scab resting on top of it, the scab being replenished by recondensation at the surface of oxidized silica-carbon reaction gases. The proposed model is shown in the following sketch.



Sketch of Proposed Model

E.2 OUTLINE OF NECESSARY CALCULATIONS

The calculation of the recession rate for the proposed model involves the simple relation

$$\dot{s} = \frac{\dot{m}_C''}{\rho_C} \quad (E-1)$$

where ρ_C is the density of char carbon and \dot{m}_C'' is the kinetically controlled consumption rate of carbon on a unit area basis (lb/ft²sec).

Unfortunately the available kinetic data for carbon consumption by silica is based on a unit-of-initial-mass basis, since the actual contact area between the silica and the carbon phases cannot be determined. Thus the experimental data has the form

$$\left(\frac{\dot{m}_C}{m_C}\right)_0 = A e^{-E/RT} \quad (E-2)$$

In order to obtain the \dot{m}_C'' required in Equation (E-1), it is necessary to estimate the initial contact area per initial unit mass of carbon during the experiments which provided the data of Equation (E-2) since, calling this area A_0 , we can write

$$\dot{m}_C'' \triangleq \frac{\dot{m}_C}{A_0} = \left(\frac{\dot{m}_C}{m_C}\right)_0 \left(\frac{m_C}{A_0}\right) = \left(\frac{\dot{m}_C}{A_0}\right)_0 \left(\frac{m_C}{m_C}\right) \quad (E-3)$$

Thus with A_0/m_C in hand we can compute \dot{m}_C'' from Equation (E-2) and the experimental values for \dot{m}_C/m_C , and then compute \dot{S} from Equation (E-1). The \dot{S} values so calculated may then be compared to those given on page 9-12 of Reference E-1 for the scabby models. The following sections summarize the necessary calculations.

E.3 CALCULATION OF INITIAL AREA PER INITIAL UNIT MASS IN EXPERIMENTS REPORTED

Reference E-2 describes the only experiments with sufficient data reported to obtain all of the quantities required here. For computing surface area, the only possible procedure is to compute the initial area of silica available per initial pound of carbon and the initial area of carbon available per initial pound of carbon. The smaller of these two numbers represents the maximum contact area possible. The actual contact area is probably somewhat less, but there is no way of knowing the amount of reduction, so no correction will be applied here.

To compute the quantities A_0/m_C and A_0/m_{SiO_2} for the five samples reported in Reference E-2, we note from Reference E-2 that for samples 1, 2, 3, and 4 both the silica and carbon particles were nearly spherical, so that

$$\left(\frac{A_0}{m_0}\right) = \frac{\pi \delta^2}{(\pi/6) \delta^3 \rho} = \frac{6}{\rho \delta} \quad (E-4)$$

E-3

The particle diameters δ are given in each case and we will assume that $\rho_C = \rho_{SiO_2} = 2.3 \text{ gr/cm}^3$, which will not be grossly in error. In case five, a more realistic char, the silica was in the form of cylindrical fibers and the carbon was dispersed. The only area which can be computed is $(A_{SiO_2})_O$, and

$$\frac{(A_{SiO_2})_O}{(m_{SiO_2})_O} = \frac{\pi \delta L}{\rho \frac{\pi \delta^2}{4} L} = \frac{4}{\rho \delta} \quad (E-5)$$

Table E-1 summarizes the calculation of A_O for the five experiments reported in Reference E-2.

E.4 SELECTION OF KINETIC DATA AND CALCULATION OF \dot{m}_{CO}/m_{CO}

Reference E-2 reports data in the form \dot{m}_{CO}/m_{CO} (actually it reports rate of CO production but this can be directly converted to \dot{m}_{CO}) as a function of temperature. The reference suggests an E for Equation (E-2) of $70,000 \pm 10,000 \text{ cal/mol}$ but does not present values for A. Reference E-3, however, presents values of A and E/R computed from the data of Reference E-2. These values are

$$\begin{array}{ll} A & = 3.18 \times 10^6 \text{ sec}^{-1} \\ E/R & = 63,000^\circ R \text{ (corr. to } E = 70,000 \text{ cal/mol)} \end{array} \quad \left\{ \begin{array}{l} \text{For Samples} \\ 2 \text{ and } 3 \end{array} \right. \quad (E-6)$$

$$\begin{array}{ll} A & \approx 3.16 \times 10^5 \text{ sec}^{-1} \\ E/R & = 63,000^\circ R \end{array} \quad \left\{ \begin{array}{l} \text{for Samples} \\ 1 \text{ and } 5^* \end{array} \right. \quad (E-7)$$

An alternative set of constants matching the reported rate data at $1,500^\circ R$ but with the greater activation energy $80,000 \text{ cal/mol}$ is (also from Ref. E-3)

$$\begin{array}{ll} A & = 9 \times 10^7 \text{ sec}^{-1} \\ E/R & = 72,100^\circ R \end{array} \quad \left\{ \begin{array}{l} \text{for Samples} \\ 2 \text{ and } 3 \end{array} \right. \quad (E-8)$$

$$\begin{array}{ll} A & \approx 9 \times 10^6 \text{ sec}^{-1} \\ E/R & = 72,100^\circ R \end{array} \quad \left\{ \begin{array}{l} \text{for Samples} \\ 1 \text{ and } 5 \end{array} \right. \quad (E-9)$$

* Sample 4 did not yield useful rate data.

E-4

This second set of kinetic data was used to compute values of \dot{m}_{C_0}/m_{C_0} for cases 1, 2, 3, and 5. These are presented in Table E-2 together with corresponding values of \dot{m}_C obtained from Equation (E-3) and the values of A_0/m_{C_0} given in Table E-1.

E.5 COMPUTATION OF RECESSION RATES

With the area basis mass consumption rates \dot{m}_C summarized in Table E-2, it is possible to compute a surface recession rate \dot{S} with Equation (E-1). Noting that the ρ_C in Equation (E-1) is the local density of the carbon in contact with silicon, which we may presume to be roughly 2.3 gr/cm³, and not the superficial density of carbon in the char (about 7.8 lb carbon/ft³ char). With this density, we compute from Table E-2 and Equation (E-1) the recession rates shown in Table E-3.

E.6 DISCUSSION OF RESULTS

Referring to the measured recession data reported in Reference E-1 for test models with scabs, the data lie between 0.5 and 1.0 mils/second at temperatures between about 1,460°K and 1,640°K. The discrepancy between these recession data from Reference E-1 for test models with scabs and the predictions of Table E-3 for the proposed physical model considered in this section is about six orders of magnitude, the predictions being low. Although the actual calculations of predicted recession rate for the proposed model involve a number of doubtful assumptions (in particular, the calculation of contact surface area may be in error by several orders of magnitude), it would be difficult to rationalize six orders of magnitude. It is doubtful, furthermore, that the kinetic data are much in error: the data are consistent and were obtained for temperatures at most only 200°K from the scab data studied.* It must be concluded, therefore, that silica-carbon reactions by themselves probably cannot be an important mechanism in the surface recession of the scabbed test models.

* Furthermore, similar data reported by Beecher and Rosensweig in References E-4 and E-5 and amended in Reference E-2 agree with the data of Reference E-2 within an order of magnitude.

TABLE E-1

CALCULATION OF SURFACE AREA IN DEVELOPMENT OF
SILICA-CARBON REACTION KINETIC RELATIONS

Sample	Reported Data			Computed Results			
	①	②	③	④	⑤	⑥	⑦
	$\frac{m_{SiO_2}}{m_C}$	δ_C	δ_{SiO_2}	$\frac{A_C}{m_C}$	$\frac{A_{SiO_2}}{m_{SiO_2}}$	$\frac{A_{SiO_2}}{m_C} = ⑤ \times ①$	$\min(④, ⑥) = \frac{A_O}{m_{C_P}}$
		(μ)	(μ)	(m^2/gr)	(m^2/gr)	(m^2/gr)	(m^2/gr)
1	5	17	2,800	153	.93	4.65	4.65
2	15	17	2,800	153	.93	14.95	14.95
3	5	17	15	153	162	810	153
4	5	17	2,800	153	.93	4.65	4.65
5	4.3	?	1,000*	?	1.74	7.5	7.5?

*Cylinder fiber diameter

TABLE E-2

COMPUTED MASS LOSS RATES PER UNIT MASS AND PER
UNIT AREA FOR CASES 1, 2, 3, and 5

①	②	③	④	⑤	⑥	⑦
T	$\frac{\dot{m}_C}{m_C}$ with (17)	$\frac{\dot{m}_C}{m_C}$ with (18)	$\dot{m}_1'' = \frac{③}{(A_O/m_C)_1}$	$\dot{m}_2'' = \frac{②}{(A_O/m_C)_2}$	$\dot{m}_3'' = \frac{②}{(A_O/m_C)_3}$	$\dot{m}_5'' = \frac{③}{(A_O/m_C)_5}$
(°K)	(Cases 2,3) sec ⁻¹	(Cases 1,5) sec ⁻¹				
1,500	2.27×10^{-4}	2.27×10^{-5}	1.00×10^{-8}	3.11×10^{-8}	3.04×10^{-9}	6.2×10^{-9}
2,000	1.67×10^{-1}	1.67×10^{-2}	7.38×10^{-7}	2.30×10^{-6}	2.24×10^{-7}	4.57×10^{-7}
2,500	9.54	9.54×10^{-1}	4.2×10^{-6}	1.31×10^{-5}	1.26×10^{-6}	2.61×10^{-6}
3,000	1.37×10^2	1.37×10	6.01×10^{-4}	2.61×10^{-3}	1.83×10^{-4}	3.72×10^{-4}
3,500	9.5×10^2	9.5×10	4.18×10^{-3}	1.30×10^{-2}	1.27×10^{-3}	2.59×10^{-3}

TABLE E-3

SUMMARY OF PREDICTED RECESSION RATES FOR
CASES 1, 2, 3 and 5

T	Recession Rates in mils/sec			
$^{\circ}\text{K}$	\dot{s}_1	\dot{s}_2	\dot{s}_3	\dot{s}_5
1,500	8.31×10^{-7}	2.59×10^{-6}	2.53×10^{-7}	5.18×10^{-7}
2,000	6.12×10^{-6}	1.92×10^{-4}	1.86×10^{-5}	3.81×10^{-5}
2,500	3.5×10^{-4}	1.09×10^{-3}	1.06×10^{-4}	2.17×10^{-4}
3,000	5.01×10^{-2}	2.17×10^{-1}	1.52×10^{-2}	3.10×10^{-2}
3,500	3.49×10^{-1}	1.08	1.06×10^{-1}	2.16×10^{-1}

REFERENCES FOR APPENDIX E

- E-1. Schaefer, J. W., Flood, D. T., Reese, J. J., Jr., and Clark, K. J.: Experimental and Analytical Evaluation of the Apollo Thermal Protection System Under Simulated Reentry Conditions. Report 67-16, Part II, Aerotherm Corporation, Mountain View, California, July 15, 1967.
- E-2. Blumenthal, J. L., Sandy, M. J., and Burns, E. A.: Kinetic Studies of High-Temperature Carbon-Silica Reactions in Charred Silica-Reinforced Phenolic Resins. AIAA J., 4, 1053, 1966.
- E-3. Rindal, R. A., Clark, K. J., Moyer, C. B., and Flood, D. T.: Experimental and Theoretical Analysis of Ablative Material Response in a Liquid-Propellant Rocket Engine. Aerotherm Corporation, Mountain View, California, NASA CR-72301, September 1, 1967.
- E-4. Beecher, N. and Rosensweig, R. E.: Ablation Mechanisms in Plastics with Inorganic Reinforcement. ARS J., 31, 532, 1961.
- E-5. Rosensweig, R. E. and Beecher, N.: Theory for the Ablation of Fiberglass-Reinforced Phenolic Resins. AIAA J., 1, 1802, 1963.